The phase space of last glacial inception: characterization and feedbacks via ensemble coupled ice/climate modelling

by

© *Taimaz Bahadory*

A thesis submitted to the School of Graduate Studies in partial fulfilment of the requirements for the degree of

Doctor of Philosophy

Department of *Physics and Physical Oceanography*

Memorial University of Newfoundland

Dec 2019

St. John's Newfoundland

Abstract

The feedbacks between ice sheets and the rest of the climate system are a major source of uncertainty in constraining future sea level change and perhaps aspects of future climate change. In the past, there is strong evidence that large and at times relatively abrupt changes in sea level and climate occurred. The past therefore offers a testable window that may help build confidence in projecting future changes.

Climate models are used to study the evolution of ice and climate during glacial intervals. However, these models are either computationally expensive to run for glacial-scale periods, or are too simplified and miss key feedbacks between ice and the climate. To confidently model changes in the past, ensembles of transient model run on order 10 ky or longer are required. Therefore, a fast coupled ice-climate model with relevant feedbacks is required.

Beyond last glacial maximum and especially beyond the range of accurate ^{14}C dating (about 40-50 ka), constraints on past ice sheet evolution become sparse. The last glacial inception (herein including post inception peak retreat, thus covering the range of about 120 ka to 105 ka) is a poorly understood interval that includes both rapid ice sheet growth and subsequent decay. It thereby offers a challenging test for fully coupled ice and climate models.

This thesis documents 3 specific contributions. 1) The fast fully coupled ice-climate model LCice 1.0 is documented. 2) Results from an ensemble of coupled transient simulations of the last glacial inception are presented. The ensemble provides a potential phase-space of ice and climate evolution during the last glacial inception. 3) Finally, multiple sensitivity experiments isolate the impacts of the two

largest northern hemisphere ice sheets on climate and each other.

Acknowledgements

This thesis would have never be done without the kind help and support of all our group members, specially Dr. Heather Andres, who helped me with no hesitation. Also I should thank Marilena Geng, with all her supports, encouragements, and energy-balls! And at last, Dr. Lev Tarasov, who was always there for me, corrected my mistakes, made sure the research and writing follows high standards, and in general, helped me to improve my critical thinking, analyzing, and writing skills, which I will benefit for the rest of my life. I should also thank my parents, who without their supports I could not be here today.

— MUN School of Graduate Studies

Contents

List of Tables

List of Figures

List of Acronyms

AMOC Atlantic Meridional Overturning Circulation

BK Barents-Kara seas

CESM Community Earth System Model

CLIMBER CLIMate-BiosphERe model

EA Eurasia

EMIC Earth system Model of Intermediate Complexity

ESM Earth System Model

GCM General Circulation Model

GHG Greenhouse Gas

GIA Glacial Isostatic Adjustment

GSM Glacial Systems Model

ka kilo annum before present

kyr kiloyear

LCice LoveClim Ice

LGI Last Glacial Inception

LGM Last Glacial Maximum

LOVECLIM LOch–Vecode-Ecbilt-CLio-agIsm Model

MIS Marine Isotope Stage

NA North America

PD Present day

PlaSim Planet Simulator

PMIP Paleoclimate Modelling Intercomparison Project

SICOPOLIS SImulation COde for POLythermal Ice Sheets

SLE Sea level equivalent

T2m 2 m near surface air temperatures

VECODE Vegetation Continuous Description model

Chapter 1

Introduction

Climate change and associated sea level rise are fundamental issues for global society, and climate models have emerged as a key tool in understanding and constraining potential climate change. With the accelerating warming we are facing, confidence in projections of future climate and sea level requires understanding the feedbacks between ice sheet and the climate. However, as detailed below, the tools for developing such understanding are to date limited.

Earth System Model (ESM) are the primary tools for understanding and projecting possible future climate change. Full complexity ESMs have high computational costs which tend to limit ESM model usage to sub-millennial scale transient runs. This computational cost is a major limitation for coupled ice and climate contexts given that the response time of ice sheets to changes in climate is multi-timescale. The ice sheet build-up timescale is $O(1\ \text{kyr})$ to $O(10\ \text{kyr})$ while fast ice streams can have active time scales as low as $O(1\ \text{yr})$). Feedbacks between ice and climate implies that models and observations covering this whole range of time scales is required to build

coupled ice/climate system understanding and confidence in model predictions for future climate and sea level change. Confidence in ESM accuracy for modelling future climate change and especially changes in variability and possible "tipping points" is further limited given that these models are generally tuned to present-day climate.

The paleo record offers a test of ESMs under different mean states from interglacials warmer than present to the Last Glacial Maximum (LGM), ∼20 ka, when sea level on average was between 120 and 130 m lower than present due to the conversion of water to terrestrial ice. Paleoclimate also provides data to study large and at times relatively abrupt changes in the climate, such as multiple rapid warmings recorded in Greenland ice-cores, in the order of tens of years (Dansgaard-Oeschger event). Such different climate states contribute to our understanding of the climate system and its behaviour by providing analogues for current change and testable scenarios for evaluating General Circulation Model (GCM).

During the last 2.5 Myr, inferred ice volume variations from deep sea oxygen isotope records (Chappell et al., 1996; Shackleton, 1987) indicate that the climate periodically switched between glacial and interglacial conditions. These oscillations transitioned from an approximate dominant 41 kyr periodicity (approximately in phase with obliquity-driven variations in insolation) to more saw-tooth shaped glacial cycles in the last 1 Myr. The latter are characterized by long (∼ 80-90 kyr) and non-monotonic periods of ice accumulation that end abruptly with relatively rapid (∼ 10-20 kyr) deglaciation (figure 1.1). During each glacial interval, new ice sheets built up over the Northern Hemisphere continents, the Antarctic and Greenland ice sheets grew, global mean sea level decreased, as did global mean temperature and precipitation, and sea-ice cover expanded (figure 1.2). There are, however, large

uncertainties in the inferred response of the climate system to such changes, in part due to a number of feedbacks between ice and climate system components.

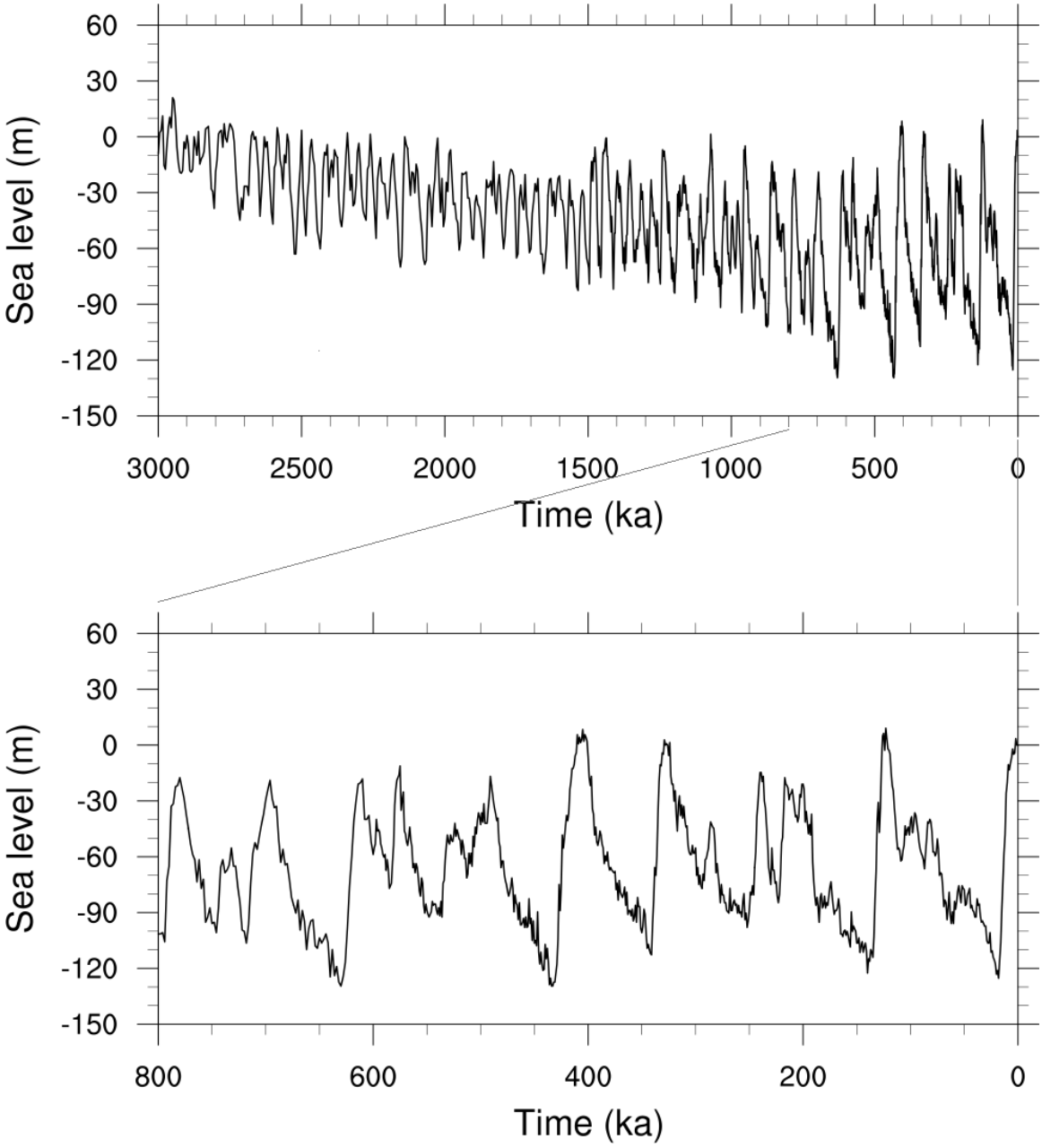

Figure 1.1: Sea level variations in the last 3 Myr (Lisiecki and Raymo, 2005).

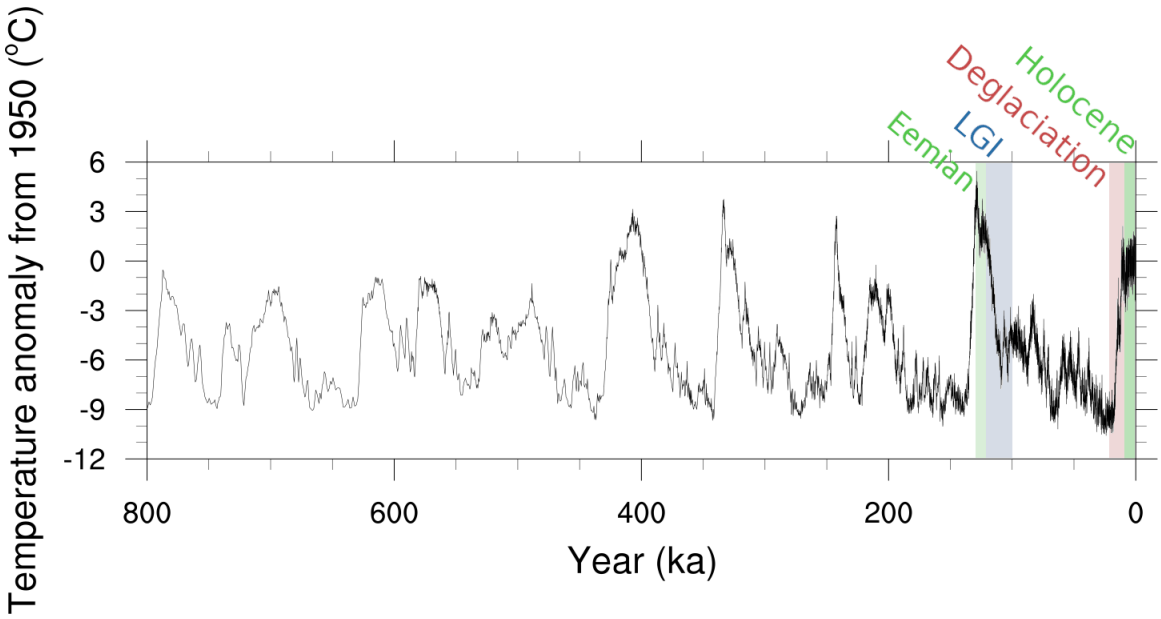

Figure 1.2: Temperature estimates of the last 800 kyr from EPICA Dome C ice core (Jouzel et al., 2007).

For instance, as ice sheets grow thicker, they can relocate or split the jet-stream (Bromwich et al., 2004; Benson et al., 1995; Bromwich et al., 2005; Andres and Tarasov, 2019), change the wave number of stationary Rossby waves, and therefore alter storm tracks, temperature, and precipitation. Changes in temperature and precipitation in return highly influence ice sheet evolution. The scale of such changes strongly depend on the elevation and location of the ice domes, which are poorly constrained in proxy records (especially prior to the LGM). Ice sheet growth/decay affects the oceans as well. Changing terrestrial ice combined with Glacial Isostatic Adjustment (GIA) can alter terrestrial runoff routing and freshwater flux into the oceans. The conversion of water to terrestrial ice lowers sea level, which can partially or completely close some of the key gateways in the ocean, such as the Bering Strait and large sectors of the Barents and Kara Seas (Groeneveld et al., 2014; Takahashi,

1998). Both of these effects can result in altering the oceans' salinity distribution and circulation. Changes in ocean circulation consequently impact the heat and moisture transport to higher latitudes, and therefore ice sheets' growth or retreat. Section 1.4 reviews feedbacks between ice and climate in more detail.

The LGM and the following termination (∼17-7 ka) have been the focus of many studies (Braconnot et al., 2007a; Otto-Bliesner et al., 2006; Liu et al., 2018; Cleator et al., 2019) as they include a rapid warming in the climate and consequent ice sheet melt, with a sea level rise of ∼120 m in 10 kyr (Peltier and Fairbanks, 2006; Lambeck et al., 2014; Clark and Mix, 2002). The temporal proximity of LGM enables a large set of well-dated and well-preserved proxy records for constraining the ice and climate state. However, the full glacial state of LGM is very far from present-day and future, and thus provides a climate state of questionable value for global warming contexts. Initializing ESMs for LGM climate modelling is also non-trivial given limited constraints on the LGM ocean state along with uncertainties in ice sheet configuration.

The last interglacial offers potentially the best paleo analogue for ongoing climate change. However, model initialization is even more of a challenge given the rapid and otherwise poorly constrained penultimate deglaciation that led to the interglacial. On the other hand, the Last Glacial Inception (LGI), ∼120-110 ka, avoids much of the uncertainties associated with model initialization, as there was no ice sheet over North America and Eurasia near the end of the last interglacial (Eemian), and Greenland and Antarctic ice sheets sizes were relatively similar to their present-day values (Helsen et al., 2013). Similarities in ice configuration and sea level between the end of the Eemian and present-day offers the latter's ice and ocean state as a

proximal initialization option for simulating LGI. Furthermore, despite the common perception that ice sheet growth is much slower than ice sheet retreat, the rate of past ice growth is at times comparable to rates of ice sheet retreat (*e.g.* Marine Isotope Stage (MIS) 7b at ∼230 ka and LGI) (Chappell et al., 1996; Waelbroeck et al., 2002; Siddall et al., 2003). During LGI, multiple marine terraces from around the world identified a fast sea level lowering of $\sim$ 60 m from 120 ka to 110 ka (Waelbroeck et al., 2002), which is almost 50% of the full-glacial sea level lowering at the LGM. This rapid change in sea level was then followed by an increase in sea level due to ice sheet retreat for the next 10 kyr. Therefore, LGI is a period of rapid ice and climate change, with a relatively more constrained initial condition. Combined, this offers an exquisite test for ESM sensitivity to orbital and greenhouse gas forcing and the capture of relevant ice and climate feedbacks that goes well beyond what is available with the current mean climate state.

However, due to the subsequent disturbance of the surface by the expanding ice sheets and being outside of the ^{14}C dating interval, proxy records of LGI ice sheet extent are scarce and poorly dated (Andrews and Barry, 1978; Stokes et al., 2012). As such, relatively little is known about the evolution of individual ice sheets during the LGI. This uncertainty percolates into the associated changes in the climate system both due to similar limitations in proxy records and the uncertainty in the required ice sheet boundary conditions for running climate models over this interval.

1.1 Modelling of the LGI

Prior to this work, modelling of the LGI was largely limited to: simulating perennial snow cover in high latitudes of the Northern Hemisphere in climate models without dynamic ice (*e.g.* Dong and Valdes, 1995; Vettoretti and Peltier, 2003, 2004), forcing climate models with uncertain prescribed ice sheet configurations (Pollard, 2010), or using highly simplified climate models coupled to ice sheet models that lacked key ice and climate feedbacks (*e.g.* Tarasov and Peltier, 1997b; Wang and Mysak, 2002; Kageyama et al., 2004; Abe-Ouchi et al., 2013).

These models have generally failed to simultaneously simulate both the inferred amount and rate of LGI sea level decrease and subsequent increase. This may be due to the complete lack of coupled dynamic ice sheets and/or the absence of key feedbacks between ice sheets and the rest of the climate system. Although climate models may be tuned to simulate the rapid sea level lowering, that tuning is then often inconsistent with the rapid retreat after 110 ka. Depending on the model resolution, the simplicity of the representation of the processes, and the feedbacks included in these models, different types of regional deficiencies can arise as well. For instance, the coupled ice - climate model of Calov et al. (2005) simulated an erroneous ice sheet over eastern Siberia and Alaska, and failed to capture ice retreat after the first glacial peak. Using a simpler 2D ice sheet model coupled to 1D energy balance climate model, Wang and Mysak (2002) also simulated extensive ice over Alaska during the early phases of the inception, which is not supported by proxy data (Hidy et al., 2013). Furthermore, they did not extend their simulation to test post-inception retreat and therefore the ability to grow ice might have been purely due to a model cold bias.

The only successful simulation of LGI prior to this study in terms of capturing both the fast ice sheet build-up and the following retreat (Ganopolski et al., 2010) also suffers from extensive glaciation of Alaska. Their coupled ice sheet (SICOPOLIS) - coarse resolution climate model (CLIMBER) was limited to an energy balance atmospheric component that relied heavily on a dust forcing chronology and ad hoc parameterization of dust impact on planetary and snow albedo. They also applied a temperature correction field over North America to aid in resolving the zonal temperature gradient, which was crucial for their modelled initiation of last glacial inception. Their model lacks some possibly key ice and climate feedbacks (such as the rerouting of ice sheet meltwater runoff into the ocean and the dependence of sub-ice shelf melt on modelled ocean temperature) and it is not clear whether their results would continue to fit global sea level variations as effectively if these feedbacks were included.

The difficulties that models have in simulating the growth and retreat of ice during the LGI suggests problems with net model sensitivity to orbital and/or greenhouse gas forcings. Therefore, the LGI interval offers a potentially strong test for climate model sensitivity to orbital and Greenhouse Gas (GHG) variations that might help constrain the wide spread of current GCM predictions for 2100 and beyond.

The extent that missing or too poorly represented ice-climate couplings and feedbacks versus other problems (such as limited model resolution and inappropriate model tuning) are responsible for erroneous sensitivity of models and the failure in capturing LGI is to date unclear. To parse this, it is first useful to review the most important missing or simplified ice-climate couplings/feedbacks in current models.

Atmosphere

The most challenging aspect of coupling ice sheet models to atmospheric models is that the spatial and time scales are very different. Within this coupled climate context, atmospheric models tend to operate at spatial resolutions of approximately 2^o to 10^o, whereas ice sheet models currently operate at grid resolutions of approximately 10 to 25km (approximately 0.1^o to 0.25^o). The climate model-computed surface temperature and orographically forced precipitation will therefore tend to be inconsistent with the O(10) to O(100) finer grid resolution of the ice sheet model. This discrepancy will be strongest in regions of high topographic variance and steep surface gradients, precisely the regions most sensitive to errors in precipitation and surface temperature (such as high elevation ice nucleation sites and ice sheet margins).

One commonly-used strategy to deal with this discrepancy for surface temperatures is to adjust the values passed from the atmosphere model at the atmospheric surface heights to the ice sheet model surface heights via a given vertical temperature gradient ("lapse rate"). The lapse rate most commonly used is a constant, often the mean free tropospheric moist adiabatic lapse rate (Gregory et al., 2012; Gardner et al., 2009), which is problematic for at least two reasons: the actual temperature gradient with height along a mountain's surface is not the same as a vertical temperature gradient measured in the free air, and vertical temperature gradients vary spatially and temporally (Marshall et al., 2007; Gardner et al., 2009).

Orographically-forced precipitation is even more of a challenge to down-scale from low-resolution model output. Paleo ice sheet models have tended to rely

on bilinear interpolation with imposed vertical precipitation gradients that run counter to that expected and observed on windward slopes.

The choice of how to spatially aggregate the topographic features of ice sheet heights from the ice sheet model's high-resolution grid to the atmospheric model's low-resolution grid is also non-trivial. Choices must be made about what attributes of the ice sheet surface are most important to retain: for example, should height be preserved at the expense of total topographic volume (say above sea level), or visa versa?

Timescales of processes in the atmosphere operate on the order of hours to years, whereas timescales for ice sheets operate primarily on the orders of decades to millennia and beyond (with sensitivities to shorter timescales for processes such as surface melt, ice stream surges, and ice calving). It is prohibitively computationally expensive for modelling groups to run ice sheet models coupled to current state-of-the-art climate models (at conventional resolutions of approximately 1^o) for multiple millennia. Therefore, due to the separation in timescales of atmospheric and glacial processes, modellers have historically chosen one of two options. If their focus is on the climate, they prescribe ice sheet conditions to be constant and non-interactive (aka a white rock) and perform climate model simulations at conventional resolutions (Pollard, 2010; Ivanovic et al., 2016). Alternatively, groups most interested in modelling ice sheet changes employ highly simplified atmospheric forcing for their ice sheet models. This simplified atmospheric forcing has tended to vary between using ice core records to interpolate temperature and precipitation between present-day climatologies

and a full glacial state as represented by snapshot GCM modelling (*e.g.* Tarasov and Peltier, 2004) and the use of energy balance climate models that thereby lack atmospheric dynamics (Tarasov and Peltier, 1997b; Huybers and Tziperman, 2008). These approaches neglect feedbacks between the ice sheets and atmosphere at their worst and simplify the responses of one component to a degree that it is no longer realistic at their best.

Ocean

Oceans and ice sheets have fewer means of interacting than the atmosphere and ice sheets do. They only come in direct contact at the margins of ice sheets and along the bottom surface of ice shelves. However, runoff and calving from ice sheets alters the distribution of salinity in the ocean (and thus its density and all associated processes), and the surface conditions of the oceans affect the temperature and humidity of air interacting with ice sheets. All of the issues of spatial and temporal scales mentioned in the previous section apply here as well. Nevertheless, there are additional simplifications to note here that are particular to ocean-ice sheet interactions.

It has until recently been common for ice shelves to not be modelled at all for paleo contexts. Once ice flowing towards its grounding line meets a thickness criteria, it is often parameterized to calve immediately (*e.g.* Roche et al. (2014)). For ice sheet models that explicitly incorporate ice shelves, the relation of sub-shelf temperature and circulation (controls on sub-shelf melt) to that of the proximal ocean model (coarser resolution) grid cell is poorly constrained (sub ice shelf marine circulation has to date not been resolved in ocean models used

for paleo contexts).

Due to relatively small-scale but dynamically-important features in the oceans such as boundary currents, the distribution of meltwater runoff from ice sheets (and thus its effect on large-scale circulation patterns) depends on where and at what depth it is injected to the ocean. While ice sheet melt is commonly determined on the high-resolution ice sheet model grid, its runoff may not be, especially if the ice sheet does not terminate at the ocean. Thus, the location that the freshwater is being injected into the ocean may not be realistically represented.

Vegetation

Records of large vegetation changes in northern Canada and Europe at the end of Eemian suggest that including missing feedbacks related to vegetation in GCMs might improve model ability to capture glacial inceptions (Cane et al., 2006). Initial investigations into the role that albedo changes due to changing vegetation cover play in the LGI indicate that including dynamic vegetation in models can help maintain snow cover through a full seasonal cycle (Pollard and Thompson, 1997; Gallimore and Kutzbach, 1996; De Noblet et al., 1996) and thereby facilitate terrestrial ice growth. In a similar study, Meissner et al. (2003) showed that land-related feedbacks can double the atmospheric cooling during glacial inception as well as the reduction of the meridional overturning in the North Atlantic. Therefore omitting the vegetation component in modelling the transient climate of the LGI may have significant impacts on the results.

Spatial Downscaling

As noted above, GCMs generally employ coarse resolutions relative to that of ice sheet models. Earth system Model of Intermediate Complexity (EMIC) tend to use even lower resolutions (*e.g.* for the LOVECLIM atmospheric component: $\sim$5.6°at equator; and for its ocean component: 3°$\times$ 3°(Goosse et al., 2010a)). This difference in spatial resolution requires careful consideration when coupling ice sheet and climate models with regards to the passing of fluxes between the models.

The model that I will be presenting herein, LCice, downscales temperature from the coarse LOVECLIM grid to that of the high resolution Glacial Systems Model (GSM) using the spatially and temporally variable vertical temperature lapse-rate and ice sheet elevation, rather than typical use of time independent scalar value (usually 6.5°C/km) (Alex S. Gardner et al., 2009; Colleoni et al., 2014). For precipitation, I use a novel scheme ("advective precipitation") to downscale precipitation that corrects for the high resolution orographic forcing of precipitation on the GSM grid compared to the order 10 times poorer topographic resolution of LOVECLIM. Both the downscaling methods are described in more detail in Chapter 2.

Temporal Downscaling

Depending on the processes and nature of the system considered, each component of a climate model integrates forward in time with a different time step. Coupling these components may require time averaging of a field from one component before passing it to another component. As shown in Chapter 2 of this thesis and Gregory et al. (2012), using different coupling time-steps can yield

different results.

From a modelling viewpoint, some of the most common approximations that may significantly limit model ability to accurately capture glacial inception/deglaciation rates and patterns are:

- the exclusion of ice-sheet dynamics (no coupled model) (Beghin et al., 2013; Liakka, 2011)
- ignoring land surface dynamics (vegetation, soil moisture) (Meissner et al., 2003)
- the choice of vertical lapse-rate (Charbit et al., 2007)
- initial conditions (model spinup length, initial ice sheet extent and thickness) (van Lent, 2013)
- the exclusion of dust feedbacks (Harrison et al., 2001)
- simplistic (or non-existent) treatment of ice calving and sub ice shelf melt that, for instance, often ignores dependence on temperature and ocean circulation.
- the exclusion or simplification of sea ice representations (Stephens and Keeling, 2000; Shine and Henderson-Sellers, 1985; Gildor and Tziperman, 2003)
- simplistic ocean models (Hewitt et al., 2003)

Despite studies showing the importance of including individual ice/climate feedbacks/couplings in climate models, there has been to date no study to include all of these in one model. This is in part due to the computational cost of the inclusion of all processes and feedbacks between different components of the climate system. For

instance, running the state-of-the-art Community Earth System Model (CESM) with all components enabled for 10 kyr year of simulation takes more than a year using O(500 cores). Using such a model to simulate tens of thousands of years is not yet practical.

The need to simulate multi-millennial timescales within a reasonable time resulted in the development of EMICs. The faster runtime (more than 1 kyr/day in the case of LOVECLIM) of EMICs is achieved by running in lower temporal and spatial resolution, and using simpler representations of dynamical processes. Fast EMICs enable the inclusion of slowly varying components of the Earth system, such as ice sheet and carbon cycle feedbacks.

Prior to this work, there was no coupled ice sheet - climate model that captured the key dynamics in both the ice and climate and associated feedbacks, and ran fast enough for transient glacial scale simulations. Therefore I developed a coupled model (LCice) by coupling the climate model LOVECLIM, to the Glacial Systems Model (GSM). This coupling includes almost all of the main feedbacks between ice sheets and climate, and is also fast enough to simulate the LGI ($\sim$ 120-100 ka) in a reasonable time ($\sim$3 weeks) using only a single CPU core.

1.2 LCice; a fully coupled ice-climate model

While developing LCice, I aimed to include almost all of the key feedbacks between ice sheets and the atmosphere and oceans, including those that have previously been absent in coupled models: dynamic meltwater runoff flux and routing, sub-shelf melt dependence on modelled ocean temperature, dynamic adjustment of Bering Strait

throughflow, ice sheet grid scale orographic forcing of precipitation, and dynamic vertical temperature lapse-rate. Figure 2.1 in Chapter 2 illustrates the coupling scheme and associated text provides details about LCice components and coupling.

LCice 1.0 is the only fully coupled ice sheet (GSM) - climate (LOVECLIM 1.3) model to date to capture the sea level changes of the LGI with only greenhouse gas and orbital forcing and with no temperature and precipitation bias correction (Bahadory and Tarasov, 2018). For the initial selection of a climate model component, I original tried to set up and run several EMICs, including MITgcm, UVic, etc. I assigned one week to the attempted porting of each model. Most of these models failed to be successfully ported, due to compilation errors, instability and multiple crashes, inconsistency in functioning with different versions of libraries, etc. Planet Simulator (PlaSim) and LOVECLIM are the only models with atmospheric, ocean, sea-ice, and vegetation components that I could port within only one week of effort. LOVECLIM has the advantage of dynamic sea ice (PlaSim only has thermodynamic sea ice) and faster speeds with much reduced computation resource requirements (LOVECLIM only runs on a single core). It was therefore selected for coupling to the GSM. However, it is worth noting that the LCice coupler is very flexible and will at some point also be used for coupling the GSM to an upgraded version of PlaSim.

Below, the main characteristics of the two models (LOVECLIM and GSM) used in LCice are reviewed.

1.2.1 LOVECLIM

LOch–Vecode-Ecbilt-CLio-agIsm Model (LOVECLIM) is a three-dimensional EMIC (Claussen et al., 2002), which includes atmospheric, oceanic, and vegetation components. The atmosphere and ocean models in LOVECLIM have different grid resolutions (details in sections 1.2.1.1 and 1.2.1.2), with a spatial resolution coarser than that of state-of-the-art GCMs. The details for each component of LOVECLIM are provided below.

1.2.1.1 The atmospheric model (ECBilt)

The atmospheric component of LOVECLIM (ECBilt) is a quasi-geostrophic model with T21 horizontal resolution ($\sim 5.6^o$ to $\sim 8^o$ in latitude and longitude) and three vertical levels for the dynamics at 800 hPa, 500 hPa and 200 hPa (Goosse et al., 2010a). Temperature is calculated at surface, 650 hPa, and 350 hPa levels. Due to the quasi-geostrophic approximation, ECBilt's simulation of the Tropics is poor. The coarse resolution of the atmospheric model flattens the topographical elevations, especially in regions with steep slopes, therefore affecting the temperature, precipitation, and precipitation type. With our temperature and precipitation downscaling schemes in LCice, I tried to partially compensate for this discrepancy. The humidity in the atmosphere is represented in ECBilt as the total precipitable water content between the surface and 500 hPa. Precipitation occurs when the total precipitable water in the layer is above the relevant threshold, or water is transported by atmospheric flow above the 500 hPa level. As shown in Chapter 2, this is one of the key parameters in controlling the evolution of ice sheets, as ice sheets highly sensitive to precipitation

amounts.

The cloud cover in ECBilt for radiative contexts is prescribed. To account for possible changes in the distribution of cloud during glacial periods, I incorporated a simple cloud parameterization in LCice 1.0 as a function of humidity. The impact of including this parameterization is shown in figure 2.9 of Chapter 2. LOVECLIM's soil model is also part of the atmospheric model. It is a single-layer land-surface model on the same grid as the atmospheric model.

1.2.1.2 The ocean model (CLIO)

CLIO is a primitive equations ocean model with a free surface, 20 vertical levels and a horizontal resolution of 3°. It includes approximations such as the Boussinesq approximation, the thin shell approximation, and the hydrostatic approximation (Goosse et al., 2000), and includes parameterization of vertical mixing and downsloping currents along the continental slope, and the Gent-McWilliams scheme for eddy-induced advection (Goosse et al., 2010a; Gent and Mcwilliams, 1990). The sea ice component is a dynamic-thermodynamic model with fractional sea ice coverage in a grid cell (Hibler, 1979), though limited to only one ice thickness category per each cell.

1.2.1.3 The vegetation model (VECODE)

The model for the terrestrial biosphere Vegetation Continuous Description model (VECODE) (Brovkin et al., 2002; Cramer et al., 2001) is a coarse-resolution vegetation model suitable for long-term simulations. VECODE consists of three sub-models: 1) a model of vegetation structure that calculates plant functional type fractions in equilibrium with climate 2) a biogeochemical model that estimates net primary pro-

ductivity and its allocation, and carbon pool dynamics 3) a vegetation dynamics model. For any given climate, there is a stable composition of plant functional types corresponding to the climate. If climate changes, the vegetation model simulates the transition from the equilibrium for the previous climate to a new equilibrium. The vegetation model does not directly interact with the ice sheet model; however, the vegetation cover affects modelled atmospheric temperature (through its albedo) and precipitation. These are both primary controls on the ice sheets' surface mass balance.

1.2.1.4 Internal LOVECLIM coupling of components

The dynamical equations of the atmospheric and ocean models are discretized on different grids. Therefore an interpolation of climatic fields is required during the exchange between the two models. CLIO provides ECBilt with the sea surface temperature, the sea ice temperature, the fraction of sea ice in each ocean grid cell and the sea ice and snow thickness. ECBilt passes CLIO the wind stresses over the ocean and sea ice, the shortwave and net heat fluxes over both sea ice- and ocean-covered fractions of each grid cell, and the solid and liquid precipitation (including runoff, evaporation and sublimation).

No flux correction on wind stress or heat fluxes is applied between ECBilt and CLIO. However, as precipitation rates in the Atlantic and the Arctic are significantly overestimated in ECBilt, they are reduced by 8.5% and 25%, respectively, before being transmitted to CLIO in order to avoid excessive ocean drift (Goosse et al., 2010a). In order to conserve mass, the excess water is dumped into the North Pacific where ECBilt underestimates precipitation.

1.2.1.5 Model performance

As LOVECLIM is a model of intermediate complexity, it cannot be expected to reproduce all observations to the same degree as a GCM. Some of the biases in the model are directly linked to the model formulation, and reducing their amplitudes can only be achieved by modifying fundamental model assumptions, which would be at the expense of some of the main advantages of LOVECLIM.

Comparing the simulated mean climate over the last decades to observations, LOVECLIM reproduces the main characteristics of the observed surface temperature distribution reasonably well (see table 2.3 in Chapter 2 for instance). As shown by Goosse et al. (2010a), the simulated mean annual zero degree isotherm by LOVECLIM averaged over the 1980-2000 period is close to that observed in present-day in both hemispheres, with a more northern position on continents than over the oceans in the Northern Hemisphere. Though not as appropriate as the JJA (June July August mean) isotherm for this context, this offers some confidence that temperatures controlling the ice margin location are at least approximately captured for present day by the model. LOVECLIM also captures the temperature gradient between the cold western and warm eastern Atlantic at mid and high latitudes, as seen in present-day observations. Goosse et al. (2010a) found that the model overestimates tropical temperatures, especially over the continents and the Eastern Pacific, resulting in an underestimation of the temperature gradient between the Eastern and Western Pacific. The zonal mean precipitation has the right magnitude in nearly all the latitude bands for present-day, although it is too symmetrical between the northern and southern hemispheres likely due to its quasi-geostrophic atmospheric approximation.

The simulation of sea ice extent is reasonably accurate in the Pacific Ocean, both during summer and winter. In the North Atlantic Ocean however, the simulated sea ice margin is too far north in Baffin Bay and the Labrador region in winter. In summer the sea ice extent is too large. In the Southern Ocean the sea ice extent is also slightly overestimated year-round.

1.2.2 GSM

The GSM (Glacial Systems Model) is a three-dimensional thermomechanically coupled ice sheet model, that includes basal dynamics, visco-elastic bedrock response (Tarasov and Peltier, 1997a), a permafrost-resolving bed thermal model (Tarasov and Peltier, 2007), positive degree day surface mass balance (Tarasov and Peltier, 2002), sub-grid ice flow and surface mass balance for grid cells with incomplete ice cover (Le Morzadec et al., 2015), ice calving, a temperature-dependent sub-shelf melt scheme, a first-order approximation to geoidal deflection, and fast surface drainage and lake solver (Tarasov and Peltier, 2006). The latter is used in the ice to ocean coupling. It has a horizontal grid resolution of 0.5°longitude by 0.25°latitude.

1.3 Climate sensitivity

A key goal of this project is to analyze the response of ice and climate to mutual feedbacks, especially those due to the climate-mediated impact of each major northern hemispheric ice sheet upon the other. The influence of the North America (NA) ice sheet on the Eurasia (EA) ice sheet evolution is of particular interest. Differences in the size and extent of the NA ice sheet during different glacial intervals have been

invoked to explain large differences in EA stadial ice extent and location (Beghin et al., 2013; Colleoni et al., 2016; Liakka et al., 2016; Ullman et al., 2014; Kageyama and Valdes, 2000). For instance, during the penultimate glacial maximum ($\sim$ 140 ka) the EA ice sheet is inferred to have been larger compared to that of the LGM, while the North American ice sheet is believed to be have been somewhat smaller than its LGM size (Colleoni et al., 2016). As well, during the last glacial cycle, there is an inferred westward migration of the EA ice sheet center of mass between successive stadials (Svendsen et al., 2004).

Given the uncertainties in the response of ice and climate to past changes, one may be led to the following question: **could small perturbations in the earth/climate/ice system result in a very different pattern of subsequent ice and climate evolution?** Answering this question requires determining the climate response to perturbations in the system, such as changes in the evolution pattern of ice and the climate due to slight variations in snow and ice albedo, the configuration of each ice sheet, or the atmosphere and ocean state at the end of Eemian. For this purpose, an ensemble of simulations, each with slightly different initial conditions and model parameters is required. Such an ensemble permits exploration of the sensitivity of ice sheets and the climate evolution to changes in the state of the climate, and the results can be used to determine if the spatiotemporal pattern of the LGI is a single attractor in the phase space of possible inceptions, *i.e.* could the LGI happen in more than one way? The ensemble approach also directly addresses the parametric uncertainty of the model. Table 2.2 of Chapter 2 summarizes the impact of the ensemble parametric uncertainty on North American and Eurasian temperature and precipitation. These ensemble results offer the paleoclimate community with a (albeit crude) probability

distribution of ice and climate evolution through LGI.

An ensemble of transient simulations for the LGI interval using a fully coupled ice-climate model with all the key ice-climate feedbacks has never been produced before. This is likely due to the lack of a fast and fully coupled model prior to introducing LCice 1.0, and also the high computational expense of doing a long and large ensemble. The development of LCice and the access to large computational resources allowed me to, for the first time, establish an ensemble of fully coupled ice/climate simulations for the LGI interval, and probe the relevant role of key ice/climate feedbacks.

1.4 Climate drivers and feedbacks during glacial intervals

As the Earth orbits around the Sun, the solar forcing at the top of the atmosphere slowly changes due to variation of three orbital parameters of the Earth's motion about the sun: (1) the eccentricity (*i.e.* of the Earth's orbit around the Sun), with periodicities of approximately 100 and 400 kyr, (2) the obliquity (*i.e.* the Earth's axial tilt with respect to the Earth's orbital plane around the Sun), with a period of 41 kyr, and (3) precession of the perihelion (*i.e.* seasonal timing of when the Earth is closest to the Sun), with an average period of approximately 23 kyr (Berger, 2014). The inferred sea level record over the last 800 kyr has a dominant spectral power at 100 kyr (ie the eccentricity), with weaker signals at 41 kyr and 23 kyr (Ruddiman, 2003). However, the high latitude summer insolation signal has its strongest spectral peak at 23 kyr (and adjacent 21 and 19 kyr) followed by 41 kyr with no significant

power at 100 kyr. Therefore it is recognized that insolation variations alone cannot explain the magnitude of the climatic response, particularly the 100 kyr cycle of ice volume that has dominated the sea level signal since 800 ka (Maslin and Ridgwell, 2005). Since orbital changes alone do not appear to explain the 100 kyr timescales of glacial cycles, contributions from other processes are required, such as the amplifying effects of greenhouse gases and other climate feedbacks (*e.g.* Gallée et al., 1992; Tarasov and Peltier, 1997b; Ruddiman, 2003). In part due to the lack of capable fully coupled ice-climate models prior to this work, the role of ice climate feedbacks is poorly understood.

1.4.1 Feedbacks in the atmosphere

As the summer insolation decreases, more snow can survive to the next winter. Persistent survival of snow to the next winter is a necessary and sufficient condition for onset of local glaciation. Subsequent feedbacks can in turn accentuate snowfall and therefore ice accumulation. Specifically the resultant increase in snow extent raises the surface albedo, which acts as a positive feedback in promoting more cooling over the region, and thereby enhancing the expansion of snow and ice. As an ice sheet thickens, its surface altitude increases, which in turn decreases surface temperature. On regional scales, the presence of an ice sheet can cool the air moving over it and thus cool the surrounding ice-free areas. The resultant temperature gradient along with direct orographic forcing alters wind directions, the distribution of precipitation amount and type, and cloudiness.

On hemispheric scales, the changing land topography resulting from ice sheet

growth and retreat can modify large-scale atmospheric circulation characteristics such as changing the jet-stream path (Beghin et al., 2013) and displacing the ITCZ (Denton et al., 2010). These changes can lead to a redistribution of heat and moisture in the Northern Hemisphere and changes to the exchange of heat between hemispheres.

To better capture these feedbacks, LCice 1.0 upscales the NA and EA ice sheets from the ice model to the climate model after each coupling step, so the atmosphere can react to the changes in elevation and ice mask. A new precipitation downscaling method is used to account for orographic forcing on the high resolution GSM grid, which as shown in Chapter 2 and 4, strongly impacts ice sheet evolution. A simple radiative cloud parameterization scheme is also included to account for cloud distribution variation as a function of air column humidity. Chapter 2 details the coupling, upscaling and downscaling methods, and cloud parameterization used in LCice 1.0.

1.4.2 Feedbacks in the ocean

On average, the surface ocean transports heat poleward (although less than the atmosphere above mid-latitudes). Warm circulating ocean water under ice shelves can result in significant sub-shelf melt (*e.g.* 1454 ± 174 gigatonnes per year in Antarctic at present-day, more than the estimated calving flux (1321 ± 144 gigatonnes per year) (Depoorter et al., 2013)), drive grounding line retreat, and thereby increase net ice sheet mass loss. Therefore in LCice, a sub-shelf melt scheme dependent on upstream ocean temperature profiles is included (details in Chapter 2).

Meltwater discharge from ice sheets into the oceans (Roche et al., 2010; Ganopolski et al., 2010) can affect the thermohaline circulation. During ice sheets growth, the

runoff from the land to the ocean declines due to water being stored as ice over land. Reduction in the freshwater flux to the ocean changes the regional ocean salinity, and hence potentially the ocean circulation. Also less water returned to the ocean means a negative mass balance for the oceans, and therefore a lower sea level. The change in sea level can alter the throughflow of some of the key gateways (such as Bering Strait, and Canadian Archipelago) with resultant impacts on ocean circulation. For instance, multiple studies have shown that Bering Strait closure can result in strengthening of the AMOC, and pre-condition the ocean state for an abrupt change in the AMOC (*e.g.* Shaffer and Bendtsen, 1994; Hu et al., 2010, 2012).

LCice dynamically and self-consistently computes both runoff and the change in Bering Strait relative sea level during transient simulations. Sensitivity experiments using LCice 1.0 confirm a strong response of ice and climate to changes in meltwater runoff and Bering Strait throughflow (Chapter 4). Changing sea level can also change the land-sea mask, and expose continental shelves, which when combined with windier conditions during glacial intervals, results in a dustier atmosphere. Increases in atmospheric dust concentration and the consequent increased rate of dust deposition on ice sheets reduces the surface albedo and thereby enhances ice surface melt. However, the current version of LCice (v1.0) does not include land-sea mask changes (beyond Bering Strait) nor a dust process representation.

1.4.3 Feedbacks involving sea ice

The presence and evolution of sea ice affects the surface albedo (Liu et al., 2009). By largely insulating the ocean from the atmosphere, it also affects air-sea heat fluxes,

CO_2 fluxes, and evaporation (Cohen et al., 2013). As such, sea ice can have a major impact on downstream air temperature and precipitation rates. The growth and retreat of sea ice is therefore expected to influence downstream ice sheet evolution. On the other hand, the cooling and change in wind direction and speed induced by ice sheets can impact downstream sea ice extent. This latter coupling is examined in Chapter 3.

Sea ice formation involves brine rejection which increases the local ocean surface density (Shin et al., 2003). It therefore also plays a critical role in deep water formation, which in turn potentially influences global scale ocean circulation. Due to the importance of sea-ice feedbacks on ice and climate evolution, a key design criterion for LCice was a climate model with dynamic/thermodynamic sea-ice.

1.4.4 Feedbacks involving vegetation

Changes in vegetation cover can strongly impact seasonal albedo and humidity, and thereby alter regional temperature and precipitation. The climate model used in LCice therefore has a dynamic vegetation model (VECODE) to account for changes in vegetation type, extent, and albedo. More details about VECODE are provided in section 1.2.1.3.

A key feedback vegetation feedback not included in LCice is that involved in the carbon cycle. LCice does account for the radiative forcing of changing atmospheric concentration of CO_2 and methane as derived from ice core records.

1.5 Summary

The last million years, with various different ice and climate configurations, provides testable scenarios for models to investigate the sensitivity of the climate system on glacial time scales and under different mean states. Among different past intervals, the LGI is a good candidate for this purpose, as 1) it represents an interval of large ice growth for ∼10 kyr, followed by a relatively rapid ice retreat, 2) The LGI has been a challenge for climate models to capture, which makes it a good test case to investigate the extent to which the absence of ice dynamics and/or relevant ice-climate feedbacks in these models is responsible for this difficulty, and 3) the similarities in the global ice distribution between the end of the last interglacial and present-day makes it a more proximal analogue for present-day climate change contexts compared to full glacial conditions (*e.g.* LGM). The LGI also reduces uncertainties in initial conditions for models compared to that of LGM.

Confident examination of ice/climate model climate sensitivity on glacial time scales requires an ensemble of simulations. This necessitates a fast, computationally cheap, and fully coupled ice-climate model, able to capture the sea level variations during the LGI as inferred from proxy records. Prior to this work, there was no such model. That is the motivation behind the development of LCice 1.0 and this project. The fully coupled LCice 1.0 can simulate the growth and retreat of ice during the LGI, and is fast enough for O(10 kyr) to O(100 kyr) ensemble simulations on commodity computer clusters.

With the ability to model the coupled ice and climate evolution of LGI in approximate accord with sea level proxy-based reconstructions, I can then address three

major questions. First, what is the likely pattern of LGI ice sheet evolution over this interval? This is intertwined with the related question of the stability of LGI under small perturbations in the system. More simply, did the LGI have to happen the way it did? Finally, the difficulty that past models have faced replicating LGI sea level changes (directly or indirectly by computing surface mass balance without a glaciological ice sheet model) raises a process question: What are the key feedbacks and their relative roles in driving both the relatively rapid growth of terrestrial ice and its subsequent retreat?

1.6 Thesis overview

This thesis is written in manuscript format. Therefore, each chapter includes a more focused literature review in its introduction.

Chapter 2 describes the LCice 1.0 model that I constructed from coupling the freely available LOVECLIM earth system model of intermediate complexity and the glacial systems model (GSM). LCice addresses the need for a fast coupled ice sheet system and climate model that includes almost all the key feedbacks between ice and climate along with explicit atmospheric, ocean, sea ice, and vegetation (albeit highly simplified) dynamics.

Chapter 2 also describes the selection of ensemble model parameters and sensitivity tests performed on these ensemble parameters for the last glacial inception interval. The sensitivity of the modelled last glacial inception with respect to each of the key ice and climate feedbacks is also analyzed in this chapter. Finally, the chapter presents the selection process for a set of 500 ensemble parameter vectors to approximately "bracket reality" that will feed into the subsequent chapters herein. This process also documents the extent to which this "reality bracketing" is achieved.

Chapter 2 was published in the open access journal Geoscientific Model Development in September 2018. According the the journal article web page, as of Oct 13/19, the paper has been viewed 1262 times (including 380 downloads), and has two citations in refereed publications. The LCice 1.0 coupler has been made publicly available on an open access server. A revised GSM for use with or without the LCice coupler will be made freely available to the community after ongoing upgrades and model documentation are completed within the next year and a half.

In chapter 3, an ensemble with the afore-mentioned 500 "reality bracketing" parameter vectors is used to simulate the LGI interval with LCice 1.0. 55 ensemble members are subsequently selected based on their performance in capturing the proxy inferred mean sea level history of LGI. This ensemble sub-set is used to examine the possible spatio-temporal patterns of northern hemispheric ice sheet growth and retreat during the LGI as well as associated climate evolution.

This article will be submitted to the open access journal of Climate of the Past prior to my defence. Upon acceptance, a high variance subset of these 55 transient runs will be publicly archived on an open access server for the paleoclimate, paleo sea level, and glacial geology communities.

Chapter 4 examines the main feedbacks of the North American and Eurasian ice sheets that operate via the climate system during the last glacial inception. It is focussed on the ice to climate to ice feedbacks that control ice sheet evolution. To partially address parametric uncertainty, this analysis is via a small ensemble approach with a high variance 11 member subset of the 55 parameter vectors from chapter 3

A revision of this chapter will also be submitted to Climate of the Past prior to my defence. The revision will address a few retrospective weaknesses which I was not able to address in time for thesis submission that was under a strict deadline from both student visa and academic contexts. These weaknesses are described in the thesis summary chapter 5.

An overall summary of the thesis, some retrospective evaluation/learnings, and suggestions for future work are presented in Chapter 5.

1.7 Co-authorship statement

Prof. Lev Tarasov originally conceived this project. Prof. Tarasov is on faculty in the Department of Physics and Physical Oceanography at Memorial University. The core of the GSM component of LCice 1.0 was provided by Prof. Tarasov. Tarasov and Bahadory jointly developed the experimental design for all major project experiments.

Authorship for the research paper presented in Chapter 2 is in the following order: Taimaz Bahadory (thesis author), and Prof. Tarasov (thesis supervisor). The manuscript was prepared by T. Bahadory and critically reviewed/edited by Prof. Tarasov. Prof. Tarasov developed the advective precipitation scheme in the GSM and helped with the design of the LCice coupling scheme. Taimaz Bahadory developed LCice 1.0, and set up and analyzed the ensemble experiments.

Authorship for the research paper presented in Chapter 3 is in the following order: Taimaz Bahadory (thesis author), Prof. Tarasov (thesis supervisor), and Dr. Heather Andres (co-author). The manuscript was prepared by T. Bahadory and critically reviewed/edited by Prof. Tarasov and Dr. Andres. Taimaz Bahadory set up and analyzed the ensemble simulations.

Authorship for the research paper presented in Chapter 4 is in the following order: Taimaz Bahadory (thesis author), and Prof. Tarasov (thesis supervisor). The manuscript was prepared by T. Bahadory and critically reviewed/edited by Prof. Tarasov. Again, Taimaz Bahadory set up and analyzed the ensemble simulations.

The thesis as a whole was critically reviewed by Prof. Tarasov.

Chapter 2

LCice 1.0: A generalized Ice Sheet Systems Model coupler for LOVECLIM version 1.3: description, sensitivities, and validation with the Glacial Systems Model (GSM version D2017.aug17)

Abstract

I have coupled an Earth System Model of Intermediate Complexity (LOVECLIM) to the Glacial Systems Model (GSM) using the LCice 1.0 coupler. The coupling scheme is flexible enough to enable asynchronous coupling between

any glacial cycle ice sheet model and (with some code work) any Earth system Model of Intermediate Complexity (EMIC). This coupling includes a number of interactions between ice sheets and climate that are often neglected: dynamic meltwater runoff routing, novel downscaling for precipitation that corrects orographic forcing to the higher resolution ice sheet grid ("advective precipitation"), dynamic vertical temperature gradient, and ocean temperatures for sub-shelf melt. The sensitivity of the coupled model with respect to the selected parameterizations and coupling schemes is investigated. Each new coupling feature is shown to have a significant impact on ice sheet evolution.

An ensemble of runs is used to explore the behaviour of the coupled model over a set of 2000 parameter vectors using Present day (PD) initial and boundary conditions. The ensemble of coupled model runs is compared against PD reanalysis data for atmosphere (2 meter temperature, precipitation, jet-stream and Rossby number of jet), ocean (sea ice and Atlantic Meridional Overturning Circulation (AMOC)), and Northern Hemisphere ice sheet thickness and extent. The parameter vectors are then narrowed by rejecting model runs (1700 CE to present) with regional land ice volume changes beyond an acceptance range. The selected sub-set forms the basis for ongoing work to explore the spatial-temporal phase space of the last two glacial cycles.

2.1 Introduction

Transitions between glacial and interglacial states have been a periodic feature of the Earth's climate for the last few million years. The driver of these transitions is understood to be orbital forcing (Berger, 2014; Birch et al., 2016; Birch et al.,

2017; Hahn et al., 2015; Rind et al., 1989), with an important role for CO_2 variations (Elison Timm et al., 2015; Ganopolski et al., 2016). Nevertheless, the role that climate feedbacks play in amplifying or inhibiting the responses to these forcings is not clear. Given available proxy data, how well do I know the progression of these glacial cycles? Is there more than one way each transition could have occurred? How sensitive were these glacial cycles to small perturbations in the external forcings (*e.g.* volcanic eruptions)? In order to address these questions, I need to understand the relative importance of different feedbacks between ice sheets and other aspects of the climate system. I can build such understanding by probing this phase space with physically-based models that include the pertinent feedbacks on glacial timescales.

Temperature and net precipitation (the solid/liquid fraction thereof) encompass the main atmospheric impacts on ice sheets. Marginal ice sheet surface mass-balance is very sensitive to the vertical temperature gradient. As indicated by the observations presented by Gardner et al. (2009), the vertical surface temperature gradient ("slope lapse rate") can be significantly different from the free-air temperature lapse-rate over the Greenland ice sheet. Furthermore, neither of these vertical temperature gradients are *apriori* appropriate for downscaling near surface temperatures to a higher horizontal resolution grid. The actual vertical gradient required is that due to changing the surface topography in the climate model. However, most coupled model studies use a fixed vertical temperature gradient set to an approximate mean free-air lapse-rate (usually between 5 to 7 °C/km) to downscale surface temperatures from coarse climate model grids (Glover, 1999; Flowers and Clarke, 2002; Thomas et al., 2003; Arnold et al., 2006; Bassford et al., 2006b,a; De Woul et al., 2006; Raper and Braithwaite, 2006). An approach somewhat more self-consistent with the atmospheric

component of the climate model is provided by Roche et al. (2014). Their coupler extracts the vertical "along-slope surface temperature gradient" from the atmospheric model and uses it to downscale temperatures to the ice sheet model. They find this dynamic approach has significant impacts, especially over mountainous regions and Greenland.

Coarse grid climate models used in long-time integrations can not resolve surface slopes on the generally much higher resolution ice sheet grids to which they are coupled. Given the strong impact of orographic forcing on precipitation, this can potentially introduce large errors in surface mass balance, especially near ice sheet margins and over rough topography. Standard bi-linear interpolation schemes for downscaling precipitation to the ice sheet grid in turn preserve these errors.

Ice sheets directly affect the atmosphere via changing land surface type (affecting albedo, surface roughness, and moisture fluxes) and changing topography. Upscaling of topography from the relatively high resolution grids of ice sheet models to the course resolution atmospheric grids (especially for fast glacial cycle context models) has a range of options between conserving peak heights and mean heights. There is no clear criteria for a "best" choice and the sensitivity to this choice is generally unclear.

Ice-sheets primarily affect oceans directly through meltwater runoff, and changing ocean bathymetry and landmask (especially gateways). The effect of ice sheet runoff on the ocean, especially the AMOC, has been the focus of many studies (Timmermann et al., 2003; Rahmstorf et al., 2005; Stouffer et al., 2006; Krebs and Timmermann, 2007; Hu et al., 2008; Otto-Bliesner and Brady, 2010; Kageyama et al., 2013a; Xun et al., 2013; Roberts et al., 2014). Their findings show the modelled AMOC

is a function of the models and coupling procedures used, in addition to the initial and boundary conditions of the experiments. These experiments generally include prescribed freshwater discharge fluxes into the ocean, in part to isolate AMOC sensitivity to freshwater forcing. The feedback of the resulting climate response on ice sheet discharge is therefore absent.

The strongest direct impact of the oceans on ice sheets is submarine melt of tidewater glaciers and sub-ice shelf melt. However, for continental scale coupled models, sub-shelf melt is either completely ignored (Ridley et al., 2005), or parameterized in a highly simplified way (*e.g.* Roche et al., 2014).

In this study, my objective is to develop a coupled ice sheet - climate model which encompasses most relevant feedbacks/interactions between the cryosphere and the atmosphere and ocean for continental glacial cycle scale contexts. Through a selection of ensemble parameters, I am also working towards bracketing the strength of these feedbacks across model ensembles. I also examined sensitivity to coupling time-step by setting up three similar simulations with different coupling time-steps (100, 20, and 10 years). Features of note in the coupling I describe herein include:

1. Dynamic vertical 2 meter temperature gradient to improve the temperature downscaling from the atmosphere model to the ice sheet model.

2. An advective precipitation downscaling scheme which accounts for wind velocity and topographic slopes.

3. Dynamic meltwater routing.

4. An efficient scheme to extract approximate lat/long gridded ocean tempera-

ture fields from LOVECLIM ocean temperature profiles for sub ice shelf melt computation

Table 2.1 compares the interactions between ice sheets and climate models only infrequently included in previous coupled modelling studies to this one. There are two main interactions yet to be implemented. First, the dust cycle and its impact on atmospheric radiative balance and ice surface albedo (and therefore surface mass balance) awaits future work. Second, the LOVECLIM ocean component does not handle changing bathymetry and landmask over a transient run. It does have a parameterized Bering Strait throughflow which permits shutdown of throughflow when local water depth approaches zero.

Table 2.1: Feedbacks/interactions sporadically included in previous studies between the ice sheet model and the rest of the climate system, compared to the current study. None include changes to land mask and bathymetry except for parameterized Bering Strait throughflow.

Source	Advective precipitation	Dynamic vertical temperature gradient	Dynamic meltwater runoff routing	Sub-shelf melt	Dust deposition
Stokes et al. (2012)	✗	✗	✗	✗	✗
Yin et al. (2014)	✗	✗	✗	✗	✗
Roche et al. (2007)	✗	✗	✓	✗	✗
Gallée et al. (1992)	✗	✗	✗	✗	✗
Ganopolski et al. (2010)	✗	✗	✗	✗	✓
Roche et al. (2014)	✗	✓	✗	✓	✗
Heinemann et al. (2014)	✗	✗	✗	✗	✗
Current work	✓	✓	✓	✓	✗

Climate models used for glacial cycle contexts need to be fast enough to simulate tens of thousands of years in a reasonable time interval, while sufficiently complex to include all important climate dynamics. I tested every freely available fast model that included ocean, atmosphere and dynamical sea ice components, and found a number of published models to be numerically unstable or otherwise unable to run or port. The only stable model with all these components was LOVECLIM. The other models tested and associated porting failures are:

SPEEDO : compilation error using PGI and Intel compilers.

FOAM (v. 1.5) : no dynamic sea ice model; compilation error using PGI and Intel compilers.

OSUVic (v. 2.8) : compilation error.

CSIRO-Mk3L (v. 1.2) : compilation error using PGI, Intel, and GCC compilers; problem accessing fftw library.

The paper is structured as follows. I first introduce the models in section 2.2. Next, I describe the coupling schemes between the ice sheet model and the atmosphere and the ocean models in section 2.3. In this section, I use the last glacial inception timeframe (120 - 110 ka) to show that inclusion of each process coupling scheme can have significant impact on the evolution of major NH ice sheets. In section 2.4, I introduce my chosen set of ensemble parameters for the coupled model. In order to justify this choice of ensemble parameters, I examine the sensitivity of the coupled model to changes in each parameter for PD climate. Then I sieve the ensemble parameter set using my coupled model with historical/PD initial and boundary

conditions via a comparison against observational/reanalysis data.

2.2 Models

2.2.1 LOVECLIM

LOVECLIM (version 1.3) is a coupled Earth Systems Model of Intermediate Complexity (EMIC), which consists of atmosphere (ECBilt), ocean with dynamic sea ice (CLIO) and vegetation (VECODE) modules. It is fast enough to simulate the last glacial inception (120 ka to 100 ka) in less than 3 weeks using a single computer core. Therefore, it has been used to simulate a wide range of different climates from the last glacial maximum (Roche et al., 2007) through the Holocene (Renssen et al., 2009) and the last millennium (Goosse et al., 2005) to the future (Goosse et al., 2007).

Atmosphere The atmospheric component (Opsteegh et al., 1998, ECBilt,) is a spectral global quasi-geostrophic model, with T21 truncation, three vertical layers at 800, 500 and 200 hPa, and a time-step of 4 hours. The quasi-geostrophic structure of the model limits its ability to simulate equatorial variability and hence atmospheric interactions between the tropics and higher latitudes. To partially compensate, it has additional ageostrophic terms to improve the representation of Hadley cell dynamics (Opsteegh et al., 1998). Precipitation is computed from the precipitable water of the first layer according to a precipitation threshold for relative humidity (default 85%). The model contains simple schemes for short and long wave radiation, with radiative cloud cover prescribed by default (Haarsma et al., 1996).

Ocean The oceanic component (CLIO: Coupled Large-scale Ice Ocean) is a 3D primitive equation model with Boussinesq and hydrostatic approximations. The model is discretized horizontally on a 3°×3°Arakawa B-grid, with 20 vertical levels on a z-coordinate. This coarse resolution enables CLIO to run fast enough for glacial cycle simulations. A free surface and a parameterization of downsloping currents (Campin and Goosse, 1999) enables CLIO to receive freshwater fluxes and capture some of their impacts on dense water flows off continental shelves. Goosse et al. (2001) describe the model in detail. A major limitation of this model (and challenge for many GCMs) for paleoclimate studies is that the bathymetry and land mask can't be changed during a transient run (specifically, there is no available nor described implementation that can do so).

Sea ice The sea ice component of CLIO is an updated version of the Fichefet and Maqueda (1997) dynamic-thermodynamic sea ice model. A visco-plastic rheology (Hibler, 1979) is used for horizontal stress-balance. The thermodynamic component of the sea ice model considers sub-grid sea ice and snow cover thickness distribution, and ice and snow sensible and latent heat storage.

Vegetation VECODE is a dynamic terrestrial vegetation model with simplified terrestrial carbon cycle (Brovkin et al., 2002). The model simulates the dynamics of two plant functional types (trees and grasses), in addition to deserts, and evolves their grid-cell fractions. These fractions are determined by the contemporaneous climate state and terrestrial carbon pool. More details about the model can be found in Brovkin et al. (1997) and Brovkin et al. (2002).

LOVECLIM has been tested for both interglacial and glacial contexts. Nikolova

et al. (2013) found that the large-scale changes in climate simulated by LOVECLIM for the last interglacial were in approximate agreement with that indicated by available proxies (differences in the ± 2.5°C range for summer, and -5 to 0°C in winter). These changes were also similar to that from a full-complexity atmosphere-ocean general circulation model (CCSM3). However due to stronger polar amplification in LOVECLIM, smaller sea ice extent and higher surface temperatures are simulated in LOVECLIM compared to CCSM3 for the interglacial.

During the Last Glacial Maximum, LOVECLIM overestimates both the minimum and maximum southern hemisphere sea ice cover compared to paleo-proxy data, while CCSM only overestimates the minimum sea ice extent (Roche et al., 2012). Roche et al. (2007) also found a reasonable agreement between the atmospheric and oceanic estimates of LOVECLIM and proxy data during the LGM (*e.g.* disappearance of much of PD Siberian boreal forest, seasonal sea-ice extent, sea surface temperature). However, the Atlantic deep ocean circulation is stronger in their simulation, which opposes the general inference of weaker AMOC during the LGM.

2.2.2 GSM

The GSM is built around a thermo-mechanically coupled ice sheet model. It includes a 4 km deep permafrost-resolving bed thermal model (Tarasov and Peltier, 2007), fast surface drainage and lake solver (Tarasov and Peltier, 2006), visco-elastic bedrock deformation (Tarasov and Peltier, 1997a), Positive Degree Day surface mass balance with temperature dependent degree-day coefficients derived from energy balance modelling results (Tarasov and Peltier, 2002), sub-grid ice flow and surface mass

balance for grid cells with incomplete ice cover (Morzadec and Tarasov, 2017), and various ice calving schemes for both marine and pro-glacial lake contexts (Tarasov et al., 2012). For the results herein, ice shelves are treated using a crude shallow ice approximation with fast sliding. The GSM is run at 0.5°longitude by 0.25°latitude grid resolution.

The GSM has three new features that have not been previously documented. First, ice calving has been upgraded to the more physically based scheme of DeConto and Pollard (2016). However, my implementation imposes the additional condition that the ice cliff failure mechanism is only imposed at ice marginal grid cells. Second, a temperature-dependent sub-shelf melt scheme that also depends on adjacent sub-glacial meltwater discharge from the grounded ice sheet has been added. The melt is proportional to the water temperature to the power 1.6 and to proximal sub-glacial meltwater discharge following the Greenland fjord modelling results of Xu et al. (2013). I also impose a quadratic dependence on ice thickness to concentrate sub-shelf melt near deep grounding lines in accord with the results of process modelling (*e.g.* Jacobs et al., 1992). Finally, a first order approximation to geoidal deflection is now included. Details of these schemes will be in an upcoming submission fully describing the revised GSM.

2.2.3 Model initialization

For the results herein, PD and glacial inception model runs are initiated with PD ice sheet thickness. The initial bed-thermal temperature field is set to the PD resultant field from a mix of best-fit past calibrated and ongoing calibration model runs (*i.e.*

without LOVECLIM as in Tarasov et al. (2012) for North America).

To initialize the temperature field of existing ice sheets, results from previous transient runs are usually used in the GSM. However, this doesn't work for a cold start from PD fields, as the PD ice thickness fields won't line up fully with model results. As such, the ice temperature field is initially linearly interpolated from surface temperature to a basal temperature of -3°C. This enforces a frozen base to insure a smooth spin-up but otherwise provides warm enough ice to generate significant ice velocities. Ice velocity fields are then computed. The ice thermodynamics is subsequently partially spun-up over 5000 years (with fully coupled bed-thermal evolution). When the results of pre-Eemian Greenland and Antarctic calibrations become available, this will be used to initialize the respective Eemian ice sheet temperature and ice thickness fields.

Glacial inception surface topography is also offset from PD by the amount required to remove PD topographic discrepancies (to observed) from some past best fit calibration model runs.

As detailed below, the climate model is spun-up over an ensemble parameter dependent time interval prior to onset of the coupled model run.

2.3 Coupling

The coupler is designed to regrid and exchange data between the ice sheet model (GSM) and LOVECLIM (ECBilt and CLIO) in both directions with minimal adjustment to the model code. Figure 2.1 displays all the fields the coupler transfers between different component models and the processes involved.

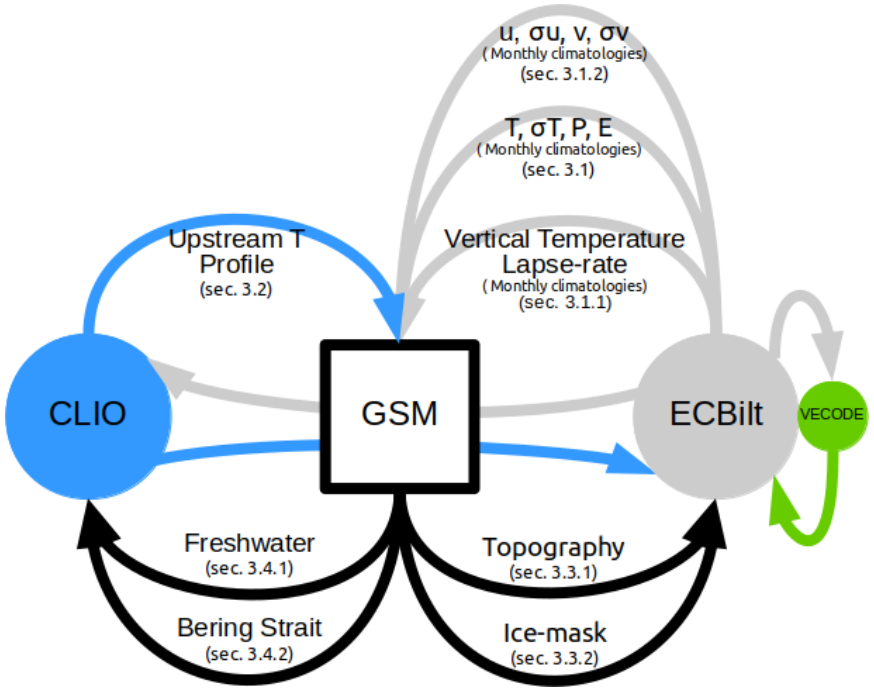

Figure 2.1: Components of the climate system and interactions between them included in the coupled model, with the section numbers in which each process is described in detail. Atmospheric fields passed from ECBilt to the GSM are monthly climatologies.

Due to the computational costs of coupling and trivial variations of ice sheets over small time-scales, the ice model and the climate model run for a certain number of years before receiving updated fields from the other model. On the other hand, using large coupling time-steps can also introduce errors into the results. To test the effect of the coupling time-step on ice sheet evolution, I used three different coupling steps (100, 20, and 10 years) to simulate the last glacial inception starting at 120 ka. With identical boundary and initial conditions for all three simulations, runs with 10 and 20 year coupling steps have less than a maximum of 3% difference in ice volume (figure 2.2). The 100-year coupling-step run (red line in figure 2.2), however, strongly

diverges from the other two during the retreat phase. This ice volume divergence is mostly due to a thinner ice in NA and EA, and a less southern extent of the NA ice sheet. A weaker response with longer coupling time-steps is expected given the delay in updating climate and ice boundary conditions for the GSM and LOVECLIM respectively. Given these results, I choose 20 years as the coupling step for all of my ensemble simulations (in part given the not insignificant overhead with the coupler as currently coded/scripted).

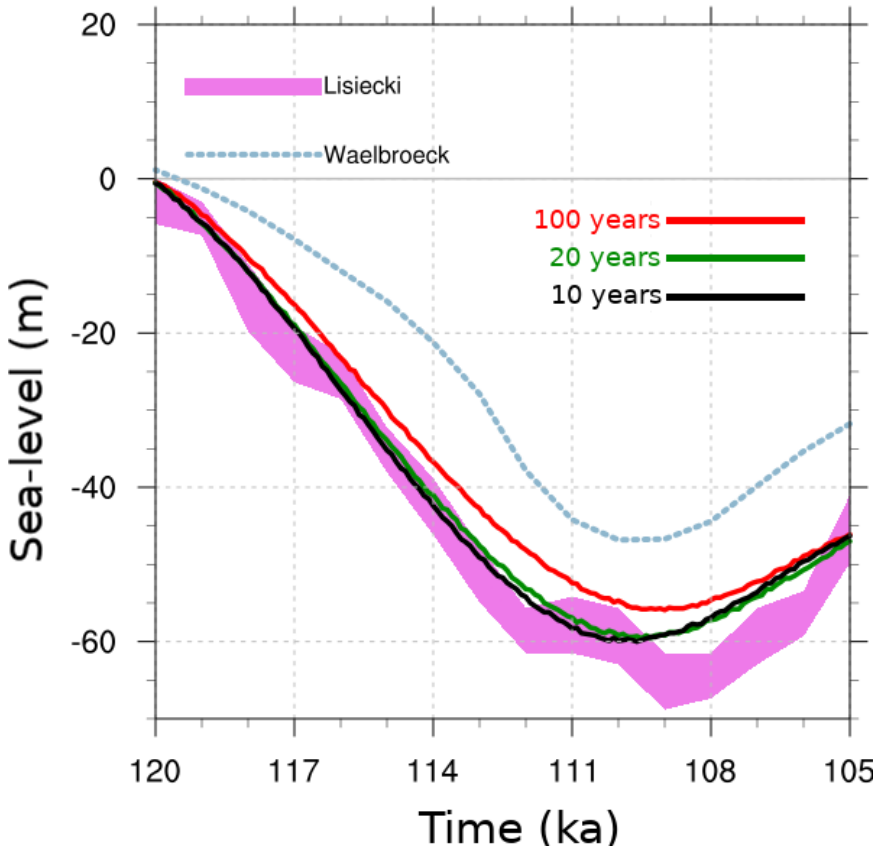

Figure 2.2: Total ice volume in sea level equivalent (m) at last glacial inception, coupled synchronously with 100, 20 and 10 year time-steps.

The ice sheet model exchanges data with both the atmosphere and the ocean models at the end of each coupling step. The fields that are passed are described in detail below.

2.3.1 Atmosphere to ice

At the end of each coupling time-step, the coupler receives climate fields averaged over the last 10 years from ECBilt and converts them to monthly-mean values. These fields include:

- 2 m near surface air temperature and standard deviation
- Vertical 2 m temperature gradient
- Precipitation
- Evaporation
- Latitudinal and longitudinal components of wind and standard deviation of each

LOVECLIM computes both 2 m near surface air temperatures (T2m) and surface (or skin) temperatures. I note at least one previous study indicates usage of LOVECLIM surface temperature for ice sheet modelling contexts (Roche et al., 2014), which I find problematic. Surface melt determination using positive degree days requires the former and rain/snow fraction determination will be more accurately estimated with the former than the latter. Ice thermodynamics would properly use the latter but this can be alleviated in part if the ice sheet model limits surface temperatures to 0°C over ice and snow for the ice thermodynamics.

Given the simplified boundary layer physics of LOVECLIM, it may be that some weighted average of its T2m and surface temperature is a more appropriate estimate of "true" 2 meter temperature. As shown in the supplement, a raw average gives somewhat better overall fits to ERA40 2 m temperatures over Greenland and Antarctica but worse fits for July over North America and especially Eurasia using the default LOVECLIM tuning. Given these mixed results (and the possibility that after retuning the average of T2m and surface temperature would give better fits), I provide an option in the coupler to extract this average temperature from LOVECLIM instead of T2m.

The large difference in spatial resolution of the two models necessitates horizontal and vertical downscaling of the climatic fields. The GSM receives climatic fields on the LOVECLIM grid, and downscales them to its own grid resolution using bi-linear interpolation.

The downscaled standard deviation of temperature (using 4-hourly ECBilt data for each month averaged over the last 10 years of each coupling time-step) is used to compute monthly Positive Degree Days, with the usual assumption of a Gaussian distribution around the monthly mean. This is opposed to the traditional practice of assuming a constant value, usually between 5°C and 7°C.

2.3.1.1 Vertical temperature gradient

Large grid resolution differences between ECBilt and the GSM result in surface elevation differences between the two models, especially in places with steep topography. The altitude dependence of temperature in such regions can drastically affect the type of precipitation and surface mass balance of the ice sheet. Therefore, in addition to

horizontally downscaling the temperature from LOVECLIM to the GSM, a vertical correction of temperature is required.

By monitoring 25 sites spread over a 15,650 km^2 area and with an altitude range of 130 to 2010 m on the Prince of Wales Icefield for two years, Marshall et al. (2007) found a mean daily vertical surface temperature gradient of -4.1 °C/km, with an average summer gradient of -4.3 °C/km. These values are less than the standard mean free-air temperature lapse-rate that is often used for extrapolations of sea level temperature to higher altitudes (-6.5 °C/km) (*e.g.* Glover, 1999; Arnold et al., 2006; Raper and Braithwaite, 2006). Marshall et al. (2007) also found a vertical surface temperature gradient of -6 to -7 °C/km on steep regions in summer, and around -2 °C/km in regions where northerly anticyclonic flow is more common. In addition, Gardner et al. (2009) found significant spatio-temporal variations in vertical temperature gradients across four glaciers in the Canadian high Arctic.

The GSM uses the near-surface vertical T2m gradient calculated by the coupler at the end of each time-step to downscale the temperature field over its high resolution grid. In each LOVECLIM grid cell, the coupler first determines the highest and lowest elevations from the GSM topography constrained by the cell's boundary. Next, the T2m for these two elevations is calculated using the inherited scheme from the LOVECLIM atmospheric model (Roche et al., 2014, as detailed in). The resulting temperatures and elevation difference between the two points is then used to calculate the temperature lapse-rate in that LOVECLIM grid cell.

Figure 2.3.a and 2.3.b show the present-day vertical T2m lapse-rate calculated by the coupler for summer and winter. The derived lapse-rate has strong spatial and temporal variation over NA and Greenland. The impact of this variation is shown

in figure 2.3.c. Starting from the same 110 ka configuration, the difference in ice thickness after 2 kyr between a dynamic temperature lapse-rate run and a control run (default LOVECLIM parameters) with 6.5 °C/km lapse rate can reach over 1 km.

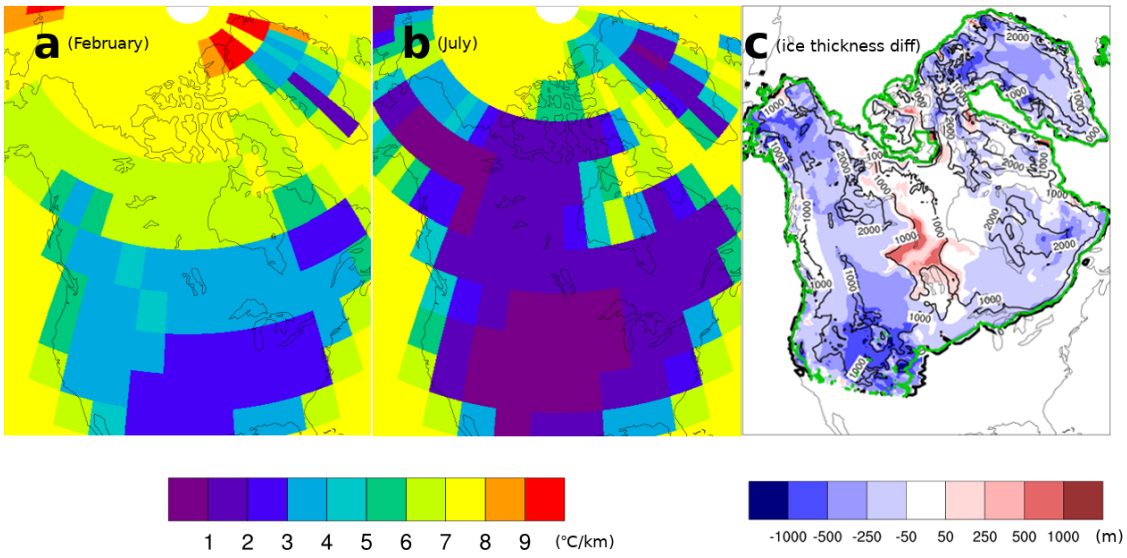

Figure 2.3: Vertical temperature lapse-rate calculated by the coupler at present day over North America in **a**. February, and **b**. July. **c**. shows the ice thickness difference between dynamic and constant 6.5 °C/km lapse rate (control) runs after running for 2 kyr, starting from the same 110 ka configuration. Black contours show the ice thickness in the control run. Thick black and green contours show the ice margin in the control and dynamic lapse-rate run, respectively.

Evaluating the appropriateness of my vertical temperature downscaling approach is difficult, especially when considering glacial/interglacial changes. Using a global climate model (CCSM3), Erokhina et al. (2017) found significantly larger surface slope lapse-rate values over the Greenland ice sheet during LGM compared to pre-industrial

values (February mean increase of about 3.7 °C/km and about 0.9 °C/km for July). In contrast, my T2m mean LGM lapse-rate over Greenland is 0.8°C/km stronger for February and 0.2°C/km weaker for July compared to that of PD. However, neither lapse rate is *apriori* an accurate choice for vertical downscaling. A need remains for a multi-resolution modelling study to compare a "true" downscaling vertical temperature gradient with the various possible lapse-rates that can be derived from a single resolution model.

2.3.1.2 Advective precipitation downscaling

LOVECLIM calculates evaporation, rain, and snow for each grid cell based on its coarse resolution surface topography and temperature fields. These fields require downscaling to the higher resolution GSM grid. A common approach is to linearly interpolate both precipitation and evaporation fields onto the high resolution ice sheet model grid, calculate the net precipitation amount, and finally determine the amount of rain and snow for each grid cell using the downscaled temperature. However, linear interpolation does not correct the damped orographic forcing due to a coarse resolution climate model grid. Here, I apply a new approach to precipitation downscaling that also accounts for orographic forcing at the ice sheet grid resolution.

The scheme assumes that orographic precipitation effects for upslope winds will be proportional to the vertical velocity induced by the surface slope and therefore to the dot product of the horizontal wind velocity and surface slope (S_{GSM} and S_{ATM}) with the latter given by:

$$S_{GSM}(\vec{u}(x, y, month, k)) = \vec{u} \cdot \nabla h, \qquad S_{ATM}(\vec{u}(x, y, month, k)) = \vec{u} \cdot \nabla h_{ATM} \quad (2.1)$$

The k in the above equations indexes a representative range of wind vectors ($\vec{u}(x, y, month, k)$) for each month. To simplify the coupling and still capture wind variation, I use monthly climatologies of mean wind velocity and its standard deviation in the determination of S_{GSM} and S_{ATM}. I compute the advective precipitation correction factor (fk_p) using in turn the S's as a function of mean, and mean $\pm$ one standard deviation and then sum over these factors with appropriate weights ($W(k)$) for a Gaussian distribution. This correction is based either on the ratio of the S terms for $S_{ATM} > 0$ (ie upslope winds) or else their difference (to transition into precipitation-shadowing). In detail, with the inclusion of a regularization term (μ, that governs the transition to precipitation-shadowing) and bounds (f_{pmin} and f_{pmax}), this takes the form:

$k = 1, 3$

$S_{ATM}(x, y, month, k) > 0 : fk_p(x, y, month, k) = MIN\left[MAX\left(\frac{S_{GSM}+\mu}{S_{ATM}+\mu}, f_{pmin}\right), f_{pmax}\right] \times W(k)$

$S_{ATM}(x, y, month, k) \leq 0 : fk_p(x, y, month, k) = MIN\left[MAX\left(\frac{S_{GSM}-S_{ATM}+\mu}{\mu}, f_{pmin}\right), f_{pmax}\right] \times W(k)$

The loop is carried out for each point on the GSM grid. The net correction for each corresponding point on the lower resolution atmospheric grid is then accumulated to generate a rescaling coefficient that is mapped back to each $f_p(x, y, month)$ on the GSM grid to ensure mass conservation. The scheme is currently implemented with $\mu = 0.005$ and $f_{pmin} = 0.2$ and $f_{pmax} = 5.0$.

The new advective precipitation downscaling results in increased ice sheet volume and southern extent for the North American ice sheet during the inception phase. This increase is largest for the southeastern sector of the ice sheet (figure 2.4). Ice thickness also decreases in some regions due to precipitation-shadowing.

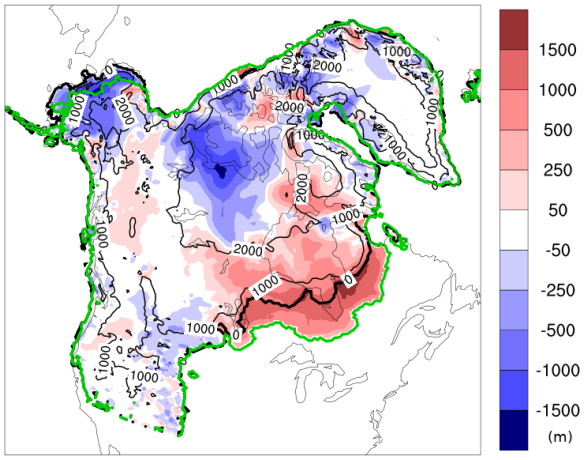

Figure 2.4: Impact of advective precipitation downscaling inclusion in the coupled model; North American ice thickness difference at 110 ka between simulations with and without the advective precipitation method. Contours show the ice thickness in the control run. Thick black and green contours show the ice margin in the control and advective precipitation run, respectively. LOVECLIM parameters are set to default values.

2.3.1.3 No bias correction

Studies of Goosse et al. (2007); Mairesse et al. (2013); Renssen et al. (2009); Widmann et al. (2010); Roche et al. (2007); van Meerbeeck et al. (2009); Otto-Bliesner and Brady (2010) demonstrate LOVECLIM's overall ability to simulate last millennium, Holocene, and the Last Glacial Maximum (LGM) climates in agreement with observed and proxy records. However, the model still suffers from a high temperature bias at low latitudes, a too-symmetric distribution of precipitation between the two hemispheres, an overestimation of precipitation and vegetation cover in the subtropics, weak atmospheric circulation, and an overestimation of the ocean heat uptake over the last decades (Goosse et al., 2010a).

The extent to which these biases are due to the tuning of LOVECLIM parameters and missing couplings with the rest of the Earth/climate system is unclear. I therefore do not apply a bias correction to atmospheric fields and instead examine the extent to which an ensemble parameter sweep can reduce the bias. As detailed below, a reduction in PD regional temperature and precipitation bias occurs for various members of my perturbed parameter ensemble.

The control run (with all LOVECLIM parameters set to their default values, and other coupling parameters as described in the caption of Table 2) shows the highest temperature bias in the "Southern NA" region (~ 5°C), with slightly colder temperatures in the "North NA" (~ 1°C). The temperature bias over EA is less significant, and is also less latitude dependent (both "Northern EA" and "Southern EA" biased by < 2°C). A reduction in regional temperature and precipitation bias is observed in various members of my later introduced ensemble of simulations for PD. The regional temperature and precipitation bias relative to observed (Table 2.3) over NA and EA can reach zero for some ensemble members for both summer and winter. Although there is no individual run with zero bias in all the regions, a number of selected runs show reduced temperature biases (between -1°C and 1°C) in all the four regions compared to that of the control run.

2.3.2 Ocean to ice: sub-shelf melt

Sub ice shelf melt is a challenge for paleo coupled ice sheet climate modelling given the dependence on unresolved basin-scale circulation. As a first order approximation, I assume that upstream ocean temperature at the same depth corresponds to the local

sub-shelf temperature. To facilitate fast and simplified coupling, given the complexity of ocean grids in most ocean general circulation models, we only extract upstream ocean temperature vertical profiles from LOVECLIM at the end of each coupling time-step for a number of chosen index sites as indicated in figure 2.5 and use these for downstream marine sectors.

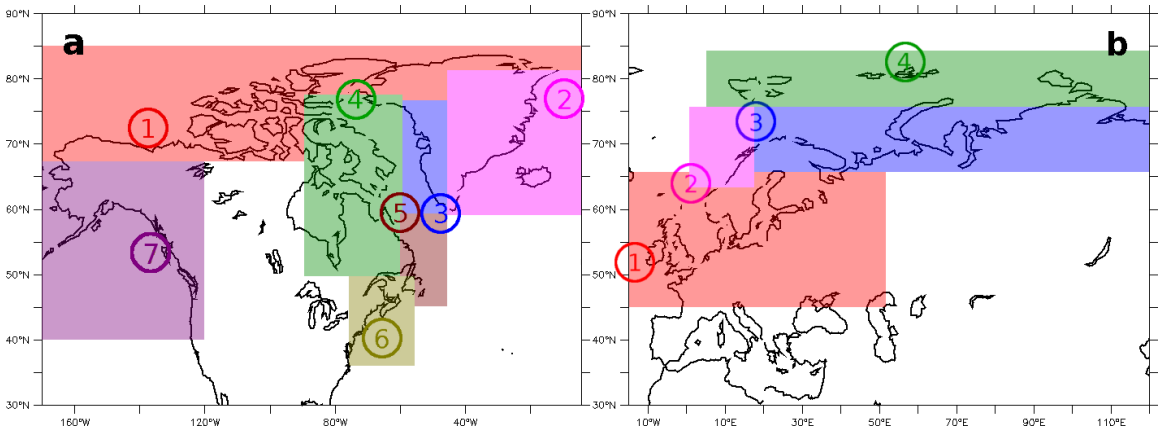

Figure 2.5: The upstream ocean temperature profile sites and corresponding downstream sectors assigned to these profiles for ocean-ice coupling in **a**. North America and Greenland, and **b**. Eurasia.

I selected these sites (7 over NA+Greenland and 4 over EA) by examining PD ocean temperature climatologies from CLIO (at various depths) while taking into account ocean currents. My site selection was predicated on the constant bathymetry and land mask of CLIO and would need updating for a model with dynamic land-mask/bathymetry. The downstream masks for the profile sites extend onto land where applicable when grounding line retreat beyond the fixed ocean mask of CLIO (ie onto the land mask) is possible.

To test the impact of this regional disaggregation of ocean temperatures, I generated three test cases: ocean temperature forcing set to PD value, to -2°C, and set to the contemporaneous average across the above index sites. Starting from a 110 ka restart, all three options have local ice thickness differences greater than 1 km after 2 kyr compared to that with the standard coupling (2.6).

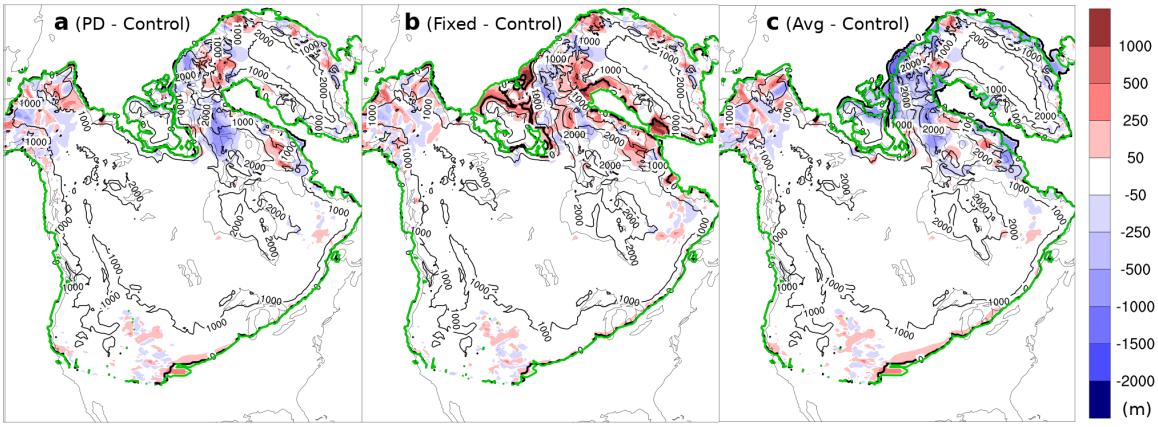

Figure 2.6: Ice thickness difference at 110 ka from the control run (dynamic ocean temperature) for: **a**. PD ocean temperature run, **b**. fixed ocean temperature at -2°C run, and **c**. temperature averaged over ocean layers run. Contours show the ice thickness in the control run. Thick black and green contours show the ice margin in the control and the other run, respectively.

2.3.3 Ice to atmosphere

Changes in both the topography and the ice-mask can affect the global circulation patterns by influencing the stationary waves and the jet-stream. At the end of each coupling time-step, the coupler receives the updated topography and ice thickness

fields from the GSM. The topography field is upscaled to the ECBilt grid and then used for the next LOVECLIM run step. Given the large difference in grid resolution, the choice of upscaling scheme is not *a priori* clear. I have therefore implemented three different schemes to upscale the topography from the GSM high resolution grid to the ECBilt low resolution grid.

2.3.3.1 Topography upscaling and ice-mask

Simple average method In this method, the coupler simply calculates a weight for each high-resolution grid cell based on the fraction of the cell located inside the coarse grid cell. These weights are then used to calculate the average altitude of each ECBilt cell from the GSM orography.

Envelope method In the envelope method, a weighted standard deviation of the altitude of all the GSM cells inside the ECBilt cell is added to the simple average altitude from the previous method. The envelope method works reasonably well to preserve the overall topographic peaks, but it can introduce a phase shift in the terrain field, broaden ridges, and raise the height of even relatively broad valleys.

$H_{i,j} = \overline{H_{i,j}} + \omega \times \sigma_{i,j}$

Here, $H_{i,j}$ is the model terrain height, ω is a predefined weighting factor (in my experiments 0.5), and $\sigma_{i,j}$ is the standard deviation at the model grid point.

Silhouette method The silhouette method combines the simple average altitude with a silhouette height. The silhouette height is defined as follows:

$H_s = \omega_1 H_{max} + (1 - \omega_1) \times \frac{(H_{sx}+H_{sy})}{2}$

where H_{max} is the maximum height of all GSM grid cells inside the ECBilt cell, H_{sx} and H_{sy} are the average peak heights obtained in each row and column of nested cells, and ω_1 is the predefined weight. The silhouette height is then used to calculate the ECBilt cell altitude using:

$$H = \omega_2 H_s + (1 - \omega_2) \times H_{mean}$$

Different combinations of weighting factors ω_1 and ω_2 will draw the gridded terrain analysis toward preserving the peaks ($\omega_2 = 1$) or preserving the mean topographic height ($\omega_2 = 0$), which allows a greater degree of freedom to determine the model terrain analysis.

2.3.3.2 Ice-mask

Another important consideration in the ice sheet - atmospheric coupling is the variation in ice extent, which changes the albedo calculated by ECBilt and, hence, affects the temperature field over the region and globally. I used the ice thickness field generated by the GSM to create the ice-mask needed by ECBilt. To do so, the high resolution ice thickness field is first regridded to the ECBilt coarse resolution grid by using one of the methods mentioned above. Any cell in the resulting grid with more than 30% ice coverage is then assumed to be ice covered.

My choice of a 30% threshold (as opposed to say 50%) was motivated by the following logic. For any atmospheric grid cell covering an ice margin segment, the temperature passed to the GSM should most importantly reflect ice covered boundary conditions local to the ablations zone of the ice sheet. Allowance for subgrid advection of warmer air masses from adjacent ice-free land somewhat tempers this logic. Given

potentially significant impacts on critical ablation temperatures and therefore ice-sheet mass-balance, this ice-fraction threshold deserves a sensitivity analysis (in future work).

2.3.4 Ice to ocean

2.3.4.1 Topographically-self-consistent and mass conserving freshwater discharge

The melting of continental ice sheets provides a freshwater source to the ocean that affects global sea level and the AMOC. Dynamical ocean models indicate that the strength of the AMOC in the North Atlantic Ocean is sensitive to the freshwater budget at the sites of formation of North Atlantic Deep Water (Rahmstorf, 1995).

As the GSM self-consistently computes surface drainage (while conserving mass) for the evolving topography while LOVECLIM surface drainage is hard-coded for PD topography, precipitation within LOVECLIM is masked out where covered by the GSM grid. The coupler then distributes GSM freshwater ocean discharge to corresponding LOVECLIM ocean discharge grid cells. Where the GSM grid edge is terrestrial, the GSM discharge is added to the corresponding LOVECLIM grid cell for internal runoff routing. As topographic gradient changes from Glacial Isostatic Adjustment (GIA) are small outside of the GSM grid, this scheme should give results close to what would be achieved with a drainage solver using a topography globally subject to GIA.

I describe the runoff routing in the coupler and the connection between the GSM and LOVECLIM drainage basins in more detail in the supplement.

Figure 2.7a provides an example of how the inclusion of meltwater runoff in the coupled model improves ice sheet growth at glacial inception. Although the impact is small at the first stages of ice formation due to small ice volumes with negligible runoff rate changes, ice in the simulation including runoff grows faster as it gains more volume. The difference reaches its maximum at 110 ka, with about 50% more ice in the run with dynamic drainage routing, including much thicker and more extensive ice over North America (figure 2.7b). Compared to the control run (no dynamic drainage routing), the AMOC strength drops by 15%, and the sea ice extent shows an increase of 5% in winter and ∼15% in summer (not shown). The combination of these AMOC and sea ice changes yields a cooler summer in the run with dynamic drainage routing, and hence less ice sheet melt.

2.3.4.2 Bering Strait

The Bering Strait is a narrow strait with a present depth of approximately 50 m between Siberia and Alaska, through which relatively fresh North Pacific water is transported to the Arctic. From there, the North Pacific water is transported to the Greenland Sea and North Atlantic. This less-saline water affects the upper ocean stratification and thus the strength of deep ocean convection and the AMOC, which in return, has impacts on the global climate (Shaffer and Bendtsen, 1994; De Boer and Nof, 2004; Hu et al., 2008).

Due to the ice sheet growth and associated sea level lowering, the Bering Strait was often closed during glacial cycles, limiting the freshwater flow from the Pacific Ocean to the Arctic. LOVECLIM does not explicitly compute the direct connection between the Pacific and the Arctic through the Bering Strait, so the transport is

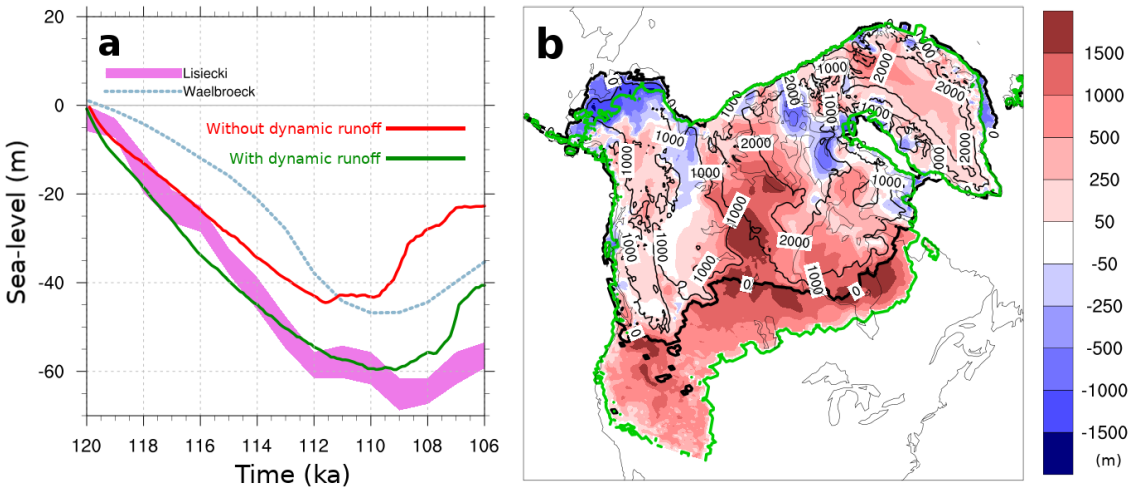

Figure 2.7: Impact of meltwater runoff inclusion in the coupled model; **a**. Total ice volume evolution at glacial inception with (green) and without (red) dynamic meltwater routing, and **b**. North American ice thickness difference at 110 ka with and without dynamic runoff routing. Contours show the ice thickness in the simulation without dynamic runoff routing. Thick black and green contours show the ice margin in the control and dynamic runoff routing run, respectively.

parameterized by a linear function of the cross-strait sea level difference in accordance with geostrophic control theory (Goosse et al., 1997). The coupler interpolates the Bering Strait scaling at each coupling step between the PD value (0.3, 50 meter depth) and a closed strait (0.0, 0 meter depth) using the relative sea level at the Bering Strait as computed by the GSM. Given the shallowness of the strait, the accuracy of the GSM in representing sea level changes (given its viscoelastic bedrock response and first order Geoidal correction) has a potentially important role here.

2.4 Ensemble parameter sensitivity analysis

Ensemble parameters were initially chosen by judgement of their control of a physical aspect of ice sheet - climate interaction (*e.g.* albedo) or by their potential impact on the coupling between the ice sheet and the climate (*e.g.* upscaling method) (Table 2.2). This choice was then validated by the following sensitivity analysis.

Table 2.2: Ensemble parameters that are varied in the historical transient simulation ensemble. Column 2: the distribution of parameter values versus their range for each parameter. Column 3: change in 1950-1980 mean summer 2 meter temperature and winter precipitation over four selected regions when each parameter is varied independently from its minimum to its maximum value. In each sensitivity run, all the other parameters are fixed to LOVECLIM default values, with spin-up length: 4000 years, simple upscaling method, default LOVECLIM cloud radiative forcing, start-year: 1500 AD, and dynamic vertical temperature lapse-rate.

Parameter	Range and Distribution	Temperature and Precipitation Sensitivity	Parameter	Range and Distribution	Temperature and Precipitation Sensitivity
Snow Albedo	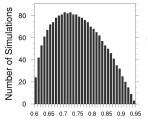	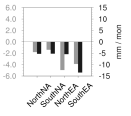	Bare Ice Albedo	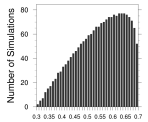	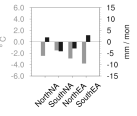
Melting Ice Albedo	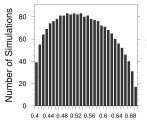	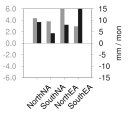	Precipitation Threshold	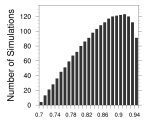	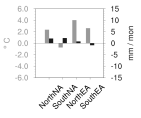
Spin-up Length (years)	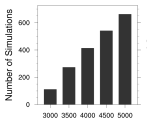	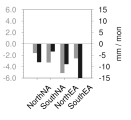	Start Year (year AD)	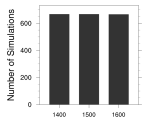	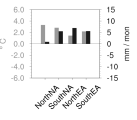
Upscaling Method	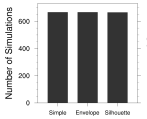	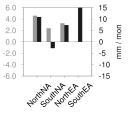	Vertical Temperature Gradient Method	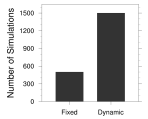	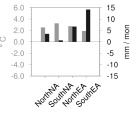
Cloud Parameterization	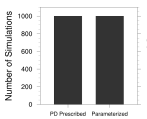	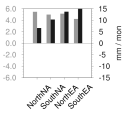			

As the context of the model development is glacial inception and deglaciation, I am interested in the ensemble performance for climate metrics which control the growth and decay of the NH ice sheets during these two stages. Therefore I use summer 2 meter temperature and winter precipitation over land. To enable comparison against observations, my sensitivity analysis is based on transient runs over the historical interval (up to 1980 CE).

Since glacial inception and deglaciation are triggered at different latitudes in NA and EA, I have divided each continent into diagnostic north and south zones (called "NorthNA", "SouthNA", "NorthEA", and "SouthEA"). The sensitivity of the coupled model is tracked for each individual zone. The "NorthNA" and "SouthNA" zones cover latitude ranges of 65-75°N and 40-60°N over NA, respectively. "NorthEA" and "SouthEA" are defined over 70-80°N and 55-70°N latitude bands, respectively. The regional boundaries are illustrated in figure 2.8.

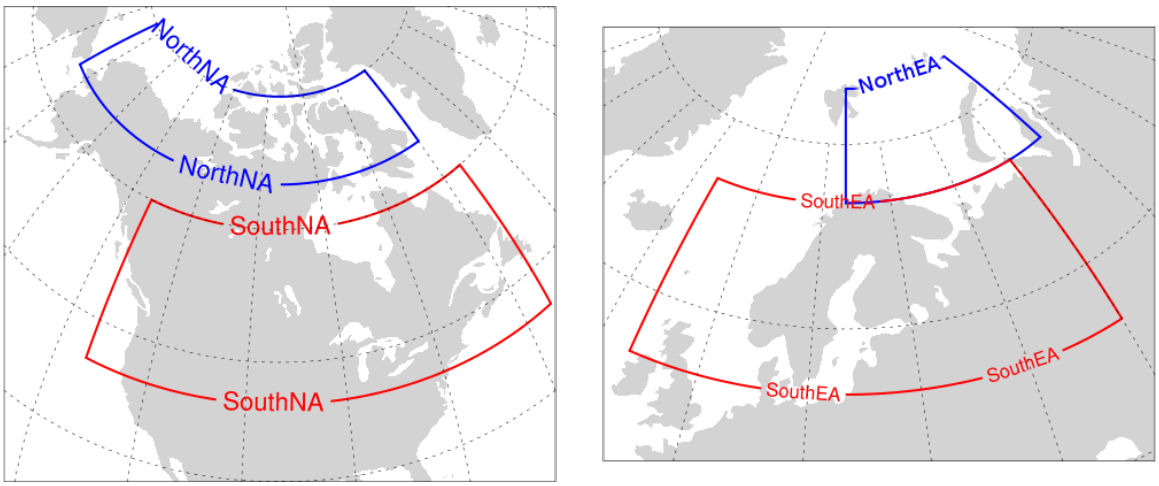

Figure 2.8: Selected north and south zones over North America and Eurasia for present day sensitivity analysis.

The third column in Table 2.2 shows the sensitivity of T2m and precipitation in the coupled model to changes in each parameter through its range for four different latitudinal bands over NA and EA averaged over the 1950-1980 interval. For easier comparison, all figures use the same temperature and precipitation scales. The sensitivity to each parameter for the four regions is different for temperature and precipitation. For instance, switching between PD radiative cloud forcing and cloud parameterization strongly affects both temperature and precipitation over all regions, while changing the snow albedo has its strongest impact on EA temperatures and precipitation (Table 2.2). Each of the ensemble parameters has an impact of at least 4°C on temperature and/or 1 cm/month on precipitation over the given parameter ranges. I take this as justification for their continued use as ensemble parameters.

In the following subsections, I further describe the parameters used in the ensemble simulation. Later, I will show the chosen set of ensemble parameters is adequate for bracketing the relevant (temperature and precipitation) fields of the climate system.

2.4.1 Snow and ice albedo

Changes in the snow and ice area and type have an amplifying effect on climate by modifying the surface albedo. During summer, the balance between absorbed and reflected solar energy at the ice sheet surface is the dominant factor controlling surface melt variability in the ablation zone (van den Broeke et al., 2008). The parameterization of the surface albedo in LOVECLIM takes into account the state of the surface (frozen or melting) and the thickness of the snow and ice covers (Goosse et al., 2010a). I include all types of snow and ice albedo (ie snow, melting snow, and

bare ice) in my ensemble parameter set.

The "Snow Albedo", "Bare Ice Albedo", and "Melting Ice Albedo" rows in Table 2.2 show the range of albedo values for each type and their climate sensitivity. Increasing snow albedo results in a reduction of winter precipitation over all four regions with an extended effect over summer temperatures, as expected. However, the same feedback is not as straightforward for bare ice albedo and melting ice albedo. Although the increase in bare ice albedo shows an expected cooling effect over all regions with a smaller influence on precipitation, an increase in melting ice albedo causes all regions to get warmer between 4 and 6°C and increases the winter precipitation.

2.4.2 Climate initialization/spin-up

Before starting a coupled transient climate simulation, it is necessary to allow the atmosphere and ocean to adjust to the initial boundary conditions and external forcings. Model spin-up, and therefore the initial state of the climate system, can be a major source of uncertainty in climate modelling especially given the millennial timescale of deep ocean circulation.

The general approach to spin-up the ocean is to run the ocean to an equilibrium state under fixed external forcings (*e.g.* Manabe et al., 1991; Johns et al., 1997). However, as the climate system is unlikely to ever be in equilibrium, this choice lacks justification. I include two parameters to control the initial state of the system: LOVECLIM spin-up start year, and LOVECLIM spin-up length. All spin-ups are performed using transient orbital and CO_2 forcings ranging from 3000 to 5000 years but without the GSM coupling. The combination of these two spin-up control pa-

rameters results in slightly different coupled transient start times, each with different initial ocean and atmosphere states. For the runs herein, I constrain the spin-up to end between 1400 and 1600 CE. Increasing the spin-up length has a cooling and drying effect in the coupled model with PD boundary and initial conditions, while starting the transient coupled run from earlier years results in slightly warmer and wetter conditions (Table 2.2).

2.4.3 Upscaling

The three different upscaling methods described in section 2.3.3.1 are evenly distributed between ensemble members as shown in Table 2.2. By switching between three methods, I calculate the highest temperature and precipitation changes over four regions and plotted in the last column of Table 2.2. The highest temperature sensitivity to the upscaling method is recorded in NorthNA followed by the NorthEA zones, and the highest precipitation sensitivity is seen in the SouthEA zone.

2.4.4 Precipitation threshold

ECBilt accounts for humidity, and thus precipitable water, only between the surface and the 500 hPa layer. Above 500 hPa, the atmosphere is assumed to be dry, so all the water transported by atmospheric flows into this region precipitates. Below the 500 hPa layer, ECBilt precipitates all the excess water above a fixed threshold (default 0.83) multiplied by the vertically integrated saturation specific humidity (Goosse et al., 2010a). This parameter has the largest relative impact for NorthEA temperature (4°C over the parameter range equivalent to 60% of mean).

2.4.5 Cloud radiation parameterization

The representation of clouds is one of the largest sources of uncertainty in models. They play an important role in regulating the surface energy balance of ice sheets, with competing warming and cooling effects at the surface through changes to short- and long-wave radiative fluxes. The effect of ice sheets on cloud formation is also significant. The growth of ice sheets results in tropospheric cooling and a reduction in humidity. This colder and drier troposphere displaces the upper tropospheric stratiform clouds downward, and reduces the low level stratiform cloud cover around the ice sheets (Hewitt and Mitchell, 1997).

The total downward and upward long-wave radiative scheme in ECBilt is a function of the vertical profile of the temperature, the concentration of various GHGs, and the humidity, and is computed for both clear-sky and cloudy conditions. The radiation computed for each grid cell is then the weighted average of these two conditions based on the cloud coverage. The default ECBilt configuration prescribes radiative cloud coverage to the PD ISCCP D2 data-set (Rossow, 1996). The total downward and upward shortwave radiative fluxes depend on the transmissivity of the atmosphere, which also relies on the prescribed cloud cover (Goosse et al., 2010a).

Given the importance of cloud radiative feedbacks on ice sheet evolution, the use of a prescribed PD cloud cover for paleoclimate modelling lacks justification. Therefore, we have added a simple cloud parameterization scheme similar to the precipitation parameterization scheme as described in section 2.4.4. The only difference here is the humidity threshold for cloud formation, which is assumed to be 10% less than the precipitation threshold, allowing cloud cover without precipitation. Including the

dynamic cloud cover radiation feedback in the coupled model slightly decreases the total ice volume at glacial inception (figure 2.9) through reduced humidity during glacial conditions reducing the cloud cover.

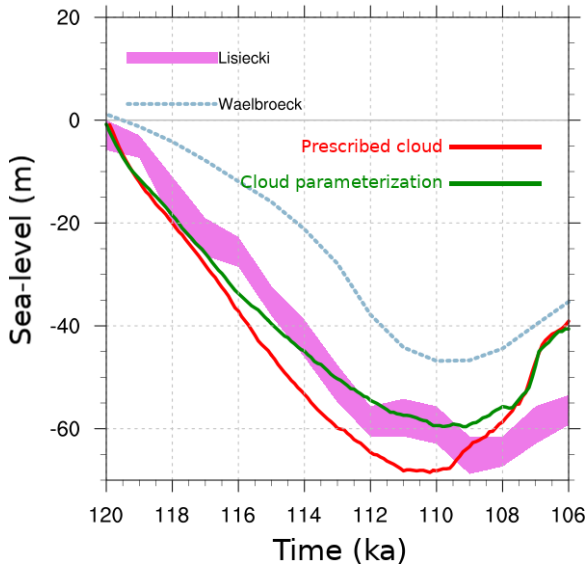

Figure 2.9: Total ice volume at the last glacial inception with the cloud parameterization (green) and with the PD cloud cover forcing (red).

As evident in the "Temperature and Precipitation Sensitivity" column in Table 2.2, regional temperature and precipitation is sensitive to each of my ensemble parameters in the coupled model. However, due to the non-linearity of the climate system, the combined effect can be significantly different. In the next section, I explore the coupled model response to all these parameters in an ensemble of simulations.

2.5 Present day ensemble results

The fast runtime of the coupled model permitted an initial ensemble of 2000 PD simulations using the fully-coupled GSM-LOVECLIM and varying the model parameters described above. I chose the PD interval to permit comparison of the coupled model output against observational data and to select a better fit sub-ensemble for transient paleo runs. All simulations are spun-up using transient forcings (orbital (Berger, 1978) and GHG Law Dome (for recent CO2 data) and Dome C (Etheridge et al., 1998; Monnin et al., 2001) (for pre-industrial to 5 ka)) for 3000 to 5000 years without the GSM coupled, followed by a transient coupled run ending at year 1980. The ensemble parameter values were generated via a Latin-Hypercube scheme with increased weighting near LOVECLIM default values.

Given a priority to "bracket reality" and limitations of the component models, I chose to not use climate characteristics for the sub-ensemble filter. My focus on coupled ice and climate and my choice to avoid bias corrections led to a trial criteria based on ice volume changes (between 1700 and 1980 CE). Therefore I used the PD simulated NH ice sheet growth to sieve out parameter vectors with major surface mass-balance biases. I first considered a less than 0.1 m SLE change in ice volume requirement for each of the 3 northern ice sheet regions. But this already fell below my target size of 500 simulations with NA being the problematic region (figure 2.10). So we changed the criterion to be the 500 runs with the least amount of ice volume change over each ice sheet. The sub-ensemble NA simulations have ice volume less than 0.15 m SLE and ice volume changes for the other two ice sheets well below 0.1 m SLE (figure 2.10). Crucial to our "reality bracketing", there are about 80

sub-ensemble members with ice loss over the given time interval.

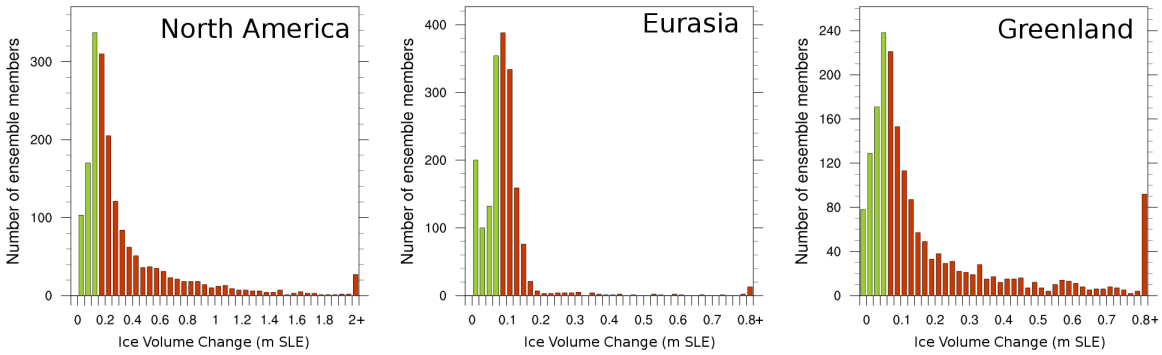

Figure 2.10: The distribution of ice volume change over NA, EA, and Gr, between 1700 and 1980 CE in 2000 ensemble runs. Green bars represent the selected 500 ensemble members, and red bars represent the rest.

From here on, I focus on the 500 member sub-ensemble results. Figure 2.11 shows the Greenland region ensemble mean thickness and standard deviation at PD. The largest ice thickness changes occur at the southern margins of the Greenland ice sheet. Eastern NA ice expansion is concentrated in the high Arctic (Ellesmere Island and adjacent) where PD ice caps exist.

2.5.1 2 meter temperature and precipitation

The ensemble distribution of the annual mean global T2m anomaly with respect to observations shows that the majority of the ensemble members fall within ± 3°C from observation (grey bars in figure 2.12). However, as ice sheet build up is a function of both temperature and precipitation, most of the warm biased simulations fail to maintain ice-free conditions over NA and EA during PD due to a high winter

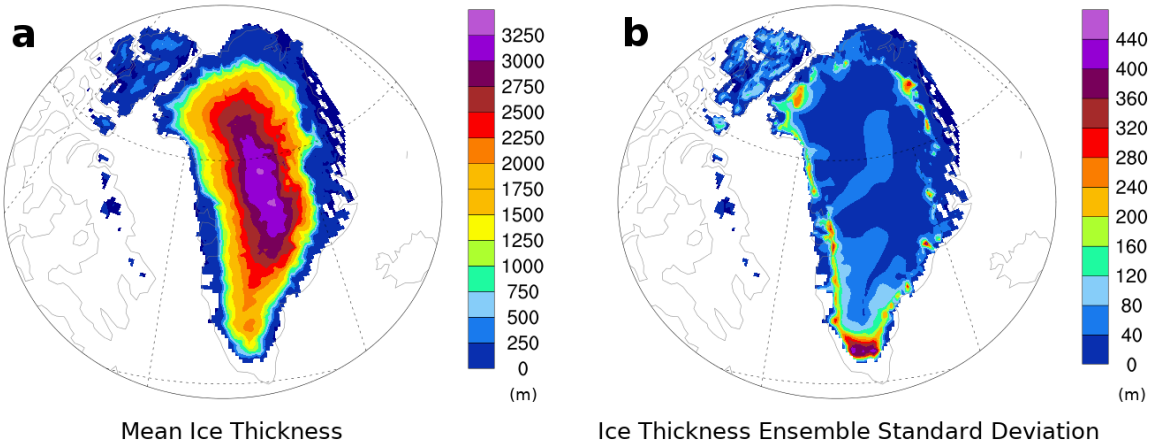

Figure 2.11: Greenland ice thickness ensemble **a**. mean, and **b**. standard deviation at PD.

precipitation bias (Table 2.3).

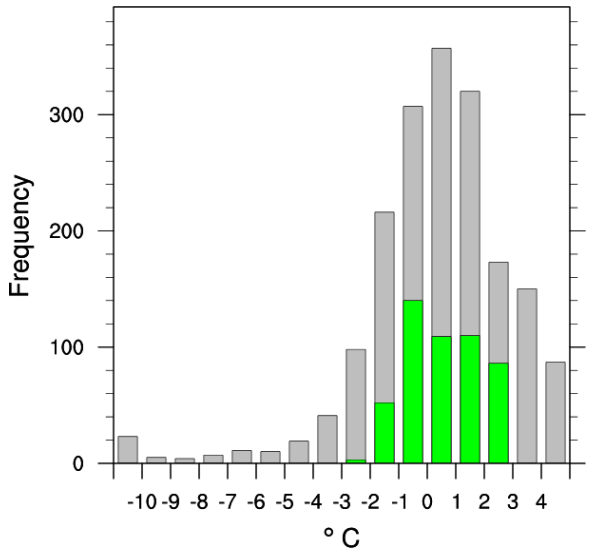

Figure 2.12: The distribution of global annual mean 2 meter temperature difference between ensemble members and observations averaged from 1950 to 1980 CE. Grey and green bars represent the 2000 ensemble members and the top-performing 500 ensemble members respectively.

Table 2.3: The sieved sub-ensemble and observed mean summer and winter 2 meter temperature and precipitation averaged over four latitudinal bands for the 1950-1980 CE interval.

		Summer		Winter	
Zone		T2m (°C)	Precipitation (mm/month)	T2m (°C)	Precipitation (mm/month)
NorthNA	Model Ens.	6.3±2.3	54.3±14.3	-25.2±3.9	20.0±5.4
	Observation	4.7	30.6	-27.9	10.5
SouthNA	Model Ens.	18.0±2.1	85.2±19.7	-7.7±2.1	56.4±5.3
	Observation	15.0	68.5	-9.7	49.4
NorthEA	Model Ens.	5.6±2.3	33.4±5.6	-8.3±5.5	16.7±6.9
	Observation	3.3	27.2	-14.0	8.9
SouthEA	Model Ens.	14.9±1.8	60.7±10.4	-3.2±2.0	55.1±10.4
	Observation	12.9	59.7	-5.6	43.5

My four latitudinal bands defined in Section 2.4 (Table 2.3) provide more relevant temperature metrics for NH ice sheet contexts. All four regions have higher ensemble mean seasonal T2m and precipitation compared to observations. However, the observations are covered well within two standard deviations for all regions and temperature is covered within one standard deviation for most regions.

The seasonal cycle provides a partial test of a model's response to orbital forcing on Milankovitch scales. The ensemble mean seasonal cycle (difference between mean summer and mean winter) is within one standard deviation of the reanalysis data for all regions and for both temperature and precipitation (Table 2.3). Furthermore, aside

from NorthEA, the diagnostic regions have a mean difference between summer and winter ensemble temperatures within a degree C of that of the reanalysis climatology.

2.5.2 Northern hemisphere jet-stream

Jet-stream latitude and oscillations have a strong control over storm-tracks and the boundary between polar and subtropical air masses. They are therefore critical factors in controlling where and when an ice sheet margin advances or retreats. Due to the low vertical resolution of ECBilt, I compare the ensemble zonal mean of the 200 hPa zonal wind (as opposed to the more usual 300 hPa diagnostic level) with observations in winter and summer over NA and EA (figure 2.13a). The ensemble shows good agreement in capturing the maximum zonal velocity, but there is a 10 to 15 degree shift northward in the latitude of the jet in both seasons. This is likely due to the reduced temperature gradient between low and high latitude.

I also compare the 30-80°N meridionally averaged meridional wind at 200 hPa of the ensemble mean and the observations to diagnose the Rossby waves. In the summer, the longitudes of the troughs and ridges from the Pacific Ocean to the Atlantic Ocean largely match the reanalysis output within ensemble range (red line in figure 2.13b) with the largest discrepancies over the Eurasian region. During the winter, although the general pattern of the jet-stream oscillations still agrees between the model and the observations (troughs over Eurasia and North America), the mismatch between ensemble members and observations becomes more significant given the higher Rossby wave number of the model ensemble.

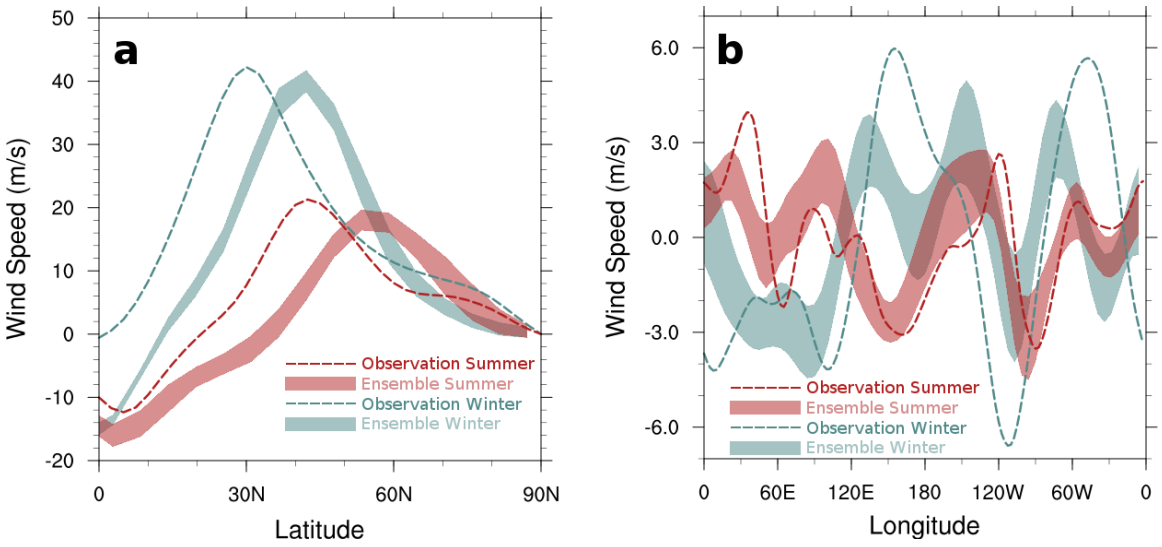

Figure 2.13: **a**. Zonal average of the zonal component of the 200 hPa wind velocity, and **b**. meridionally average of the meridional component of the 200 hPa wind velocity over the NH. Filled areas show the model ensemble mean and the two standard deviation range. Dashed lines represent observational data. Blue is for winter and red for summer.

2.5.3 Sea ice

High latitude sea ice acts as an insulator for both heat and moisture between the atmosphere and ocean, the two controlling factors for terrestrial ice sheet surface mass-balance. I use the area and minimum latitude extent of the NH sea ice as relevant diagnostics. The general warm bias of the ensemble is reflected in the reduced ice area of the ensemble for both seasons, barely capturing the observed area within the one standard deviation range of the ensemble (figure 2.14). Both March (maximum) and September (minimum) NH sea ice areas show gradual decreases in the ensemble mean as the greenhouse gas concentration increases in the model.

My filter condition for my sub-ensemble still permits a wide response of modelled components. For instance, averaging from 1950 to 1980 CE, the Pacific Ocean sea ice shows higher sensitivity to ensemble parameters during its maximum seasonal extent than the Atlantic. The sea ice minimum latitude in the Pacific ranges from 60°N to 45°N (not shown), in comparison to the observed value of 60°N (Walsh et al., 2015).

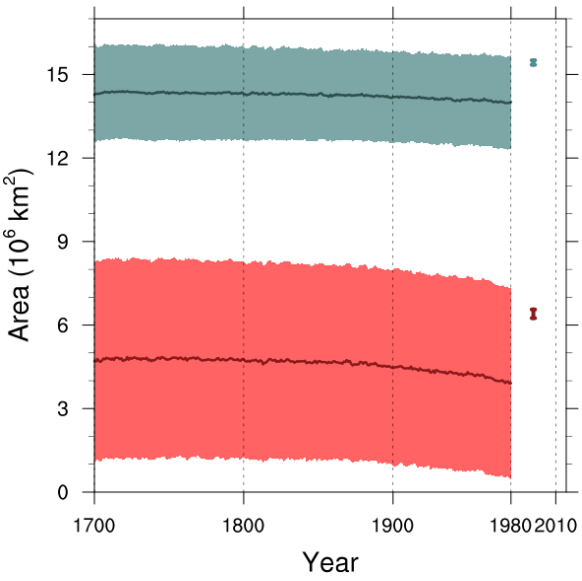

Figure 2.14: Maximum (March: blue) and minimum (September: red) sea ice area ensemble mean ± one standard deviation. The vertical lines represent observational 1981-2010 March and September mean sea ice area within one standard deviation (Walsh et al., 2015).

2.5.4 AMOC

The AMOC transports large amounts of heat and salinity between high and low latitudes. Both paleoclimate proxy records (McManus et al., 2004) and climate model

simulations (Liu et al., 2009) show that the AMOC experiences significant changes over a glacial cycle.

My "bounding reality" criteria is not met for at least two AMOC features of the sub-ensemble. The PD ensemble mean AMOC strength is weaker than the reanalysis data from European Center of Medium-Range Weather Forecasts (Balmaseda et al., 2008). The temporal mean of the reanalysis data is only captured by the maximum ensemble range (figure 2.15a). The ensemble mean shows a slight increase in AMOC strength from 1965 to 1980 CE, which is not seen in ORA-S3. As well, the temporal variability of the CLIO AMOC lacks the strong amplitude of the low frequency component of observations (as displayed by the maximum and minimum (time averaged) AMOC strength runs in figure 2.15a).

The maximum AMOC stream-function strength is seen around 50°N at 1 km depth. The ensemble variance is also highest in the same region, in addition to 0°latitude at the same depth (figure 2.15b).

2.6 Conclusions

I have coupled an Earth System Model of Intermediate Complexity (LOVECLIM) with a 3D thermomechanical coupled ice sheet systems model (GSM) using LCice 1.0. The coupling efficiently captures most of the relevant feedbacks/interactions between the ice sheet and the atmosphere and ocean models. My coupled model includes a parameterized sub-shelf melt using upstream ocean vertical temperature profiles, a simple cloud parameterization scheme to improve the radiative forcing representation in the atmosphere model, a dynamical vertical temperature gradient, and a dynamic

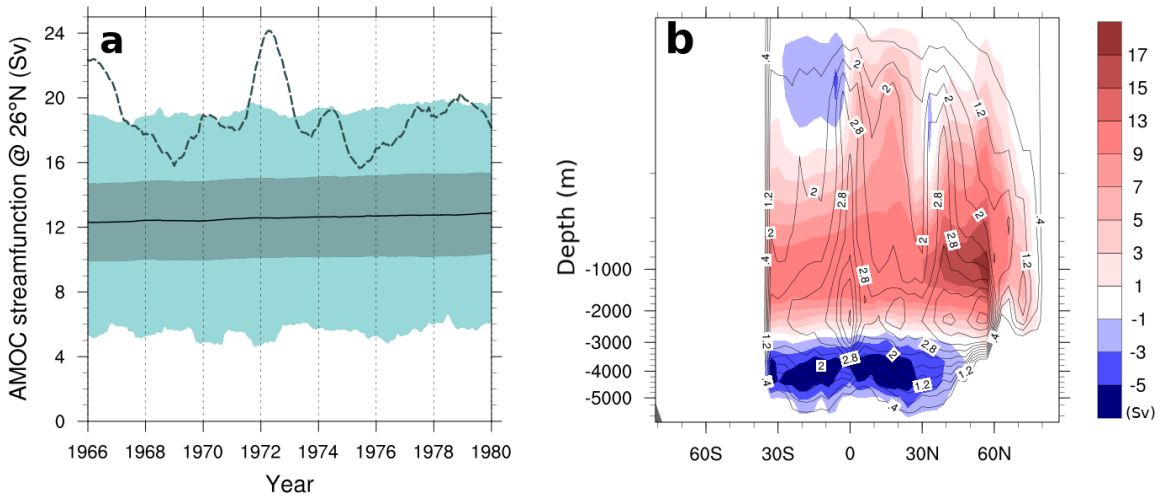

Figure 2.15: **a**. Maximum AMOC strength at 26°N between 1966 and 1980 CE. Black solid line: ensemble mean; dark blue area: ensemble mean ± one standard deviation; light blue area is bounded by the simulations with the maximum and minimum AMOC strength (time averaged); dashed line: ORA-S3 (Balmaseda et al., 2008). **b**, AMOC stream-function mean (filled colors) and ensemble standard deviation (contour lines).

meltwater runoff routing. I also introduce a new precipitation downscaling scheme that accounts for the change in surface slopes between the coarse resolution climate model grid and the higher resolution ice sheet model grid. Each of the above features has significant impact on modelled ice thickness (shown directly or via changes in temperature and/or precipitation).

I have presented a set of ensemble parameters to generate an ensemble of runs that "bracket reality" and have shown that each ensemble parameter has a significant impact on modelled PD regional temperatures and/or precipitation. The new coupled model was subject to a Latin hypercube parameter sweep of 2000 ensemble

simulations for PD boundary and initial conditions. I extracted a sub-ensemble of 500 model runs according to modelled PD NH ice volume changes. The mean of the sub-ensemble is warm and wet-biased for the NH ice sheet region. However, the model ensemble still brackets reanalysis precipitation and temperature fields within two (ensemble) standard deviations for all regions and within one standard deviation for half of the regions for the case of temperature.

The ensemble's performance at capturing the seasonal cycle is much better. The ensemble mean difference between summer and winter for all four regions is well within one standard deviation of reanalysis values for both temperature and precipitation (and within one degree C for three of the four regions). This provides some confidence that the model responds adequately to orbital forcing (at least for components that operate on sub-annual time-scales).

The "reality bracketing" criterion is not met for certain features of atmospheric circulation (especially winter-time Rossby wave number) and AMOC strength and variance. Another key limitation of LOVECLIM is the inability to change bathymetry and landmask (aside from the parameterized Bering Strait throughflow). The paleoclimate and ice sheet modelling communities would be well served by a modern successor to LOVECLIM for large ensemble glacial cycle time scale contexts that permitted transient changes to bathymetry and landmask.

The coupled model runs at about 1 kyr/day on one core and therefore enables large ensembles of full glacial cycle integrations. As a step towards this, my subset of 500 ensemble members is being used for inception and deglaciation ensemble experiments with the coupled model.

Chapter 3

The phase space of last glacial inception from coupled ice and climate modelling

Abstract

I present an ensemble of Last Glacial Inception (LGI) simulations for the Northern Hemisphere that largely captures inferred ice volume changes within proxy uncertainties. This ensemble was performed with LCice 1.0, a coupled ice sheet and climate model, varying parameters of both climate and ice sheet components, as well as the coupling between them. The spatio-temporal pattern of ice growth and subsequent retreat in both North America (NA) and Eurasia (EA) has some sensitivity to parameter changes, especially with respect to rates of ice growth and retreat. I find that the inception of ice over NA and EA is initially best characterized by the nucleation of ice at high latitude and high elevation sites, followed by subsequent spreading and merger. The

conversion of snow fields over central northern Canada plays an important role in the merging of eastern and western ice regions in NA.

The inception ice volume peak lags the summer 60°N insolation minimum, but by ∼2 kyr less than proxy reconstructions. There is little evidence that the growth of ice over NA affects its development over EA, although ice volumes consistently peak earlier over EA than NA. The inception peak in North America is characterized by a merged Laurentide and Cordilleran ice sheet, with Davis Strait covered in ice in ∼80% of simulations. Ice also connects Greenland and Iceland in all runs by 114 ka.

The Eurasian ice sheet at its peak varies across ensemble runs between a continuous ice sheet to multiple smaller ice caps. In both continents, the colder high latitudes grow ice through the entire simulation, while lower latitudes lose ice after ∼110 ka. We find temperature decreases over the initial phases of the inception lead to the expansion of NA ice sheet area, and that subsequent precipitation increases contribute to its thickening. EA ice sheet area also expands with decreasing temperatures, but sea ice limits any increases in precipitation, leading to an earlier retreat away from the EA maximum ice sheet volume.

3.1 Introduction

Reconstructions of sea level change from corals and oxygen isotope records (*e.g.* Waelbroeck et al., 2002; Siddall et al., 2003) along with some limited inferences from glacial geology (Clark et al., 1993a) indicate that between about 120 and 115 ka, large ice sheets formed rapidly in the Northern Hemisphere (NH) (Clark et al., 1993b). By 110 ka, mean sea level is inferred to have been approximately 45-65 m lower than present

(Lambeck and Chappell, 2001; Waelbroeck et al., 2002; Lisiecki and Raymo, 2005) or about half of that inferred for LGM. Contrary to the common perception that ice sheet growth is a much slower process than ice sheet retreat, this large last glacial inception (LGI) growth in ice volume occurred over approximately the same duration ($\sim$10 kyr) as the last deglaciation. This rapid ice sheet growth was subsequently followed by ice retreat for the next 10 kyr (Bard et al., 1990; Chappell et al., 1996; Gallup et al., 2002).

Two complementary paradigms have arisen to explain the rapidity of the LGI ice growth over North America: widespread thickening of snowfields (Calov et al., 2005) and spreading from high elevation nucleation sites (Weertman, 1964). However, the pattern of reconstructed LGI ice growth and decay is too poorly constrained to differentiate between them. The terrestrial record was largely destroyed by subsequent ice advance and retreat, and any proxy materials that may have survived are scattered and have large uncertainties (Lambeck and Chappell, 2001). A previous attempt to simulate the inferred sea level drop during LGI supported the widespread snowfield thickening paradigm (Calov et al., 2005). The model used in that study employed very low resolution (51°longitude by 10°latitude for atmosphere, approximately 100 km for the ice sheet model) and lacked atmospheric dynamics. Only 3 transient simulations were presented. Given the uncertainties in the proxy data and models, a much larger ensemble of simulations that captures these uncertainties is required to assess how representative this result is of the actual growth of ice sheets during the LGI.

Ideally, model studies of LGI would employ sophisticated Earth System Models (ESMs) at high resolution bidirectionally coupled to ice sheet models to produce

ensembles of transient experiments that span the uncertainties of the relevant data and processes, but this is computationally too expensive. Instead, model studies of LGI tend to make one of two simplifications. First, general circulation model- (GCM) based studies treat the climate in a sophisticated way, but rely on a small number of snapshot experiments without interactive ice sheets. Ice sheet boundary conditions are prescribed which can lead to a modelled climate that is inconsistent with the prescribed ice extent (Pollard and PMIP-participating groups, 2000). Furthermore, the reliance of these studies on at most a few model runs severely limits any possible uncertainty assessment. Second, experiments performed with ice sheet and climate models coupled together tend to employ EMIC. These model configurations include interactive ice sheets and can be run with transient boundary conditions. However, their low climate model resolution means more processes must be highly parametrized, and simplified representations mean some key feedbacks are not modelled at all.

Due to such simplifications, most LGI model studies have been unable to simultaneously simulate the required rapid ice build-up until around 110 ka as well as the subsequent retreat (*e.g.* Calov et al., 2009). Prior to the development of the LCice 1.0 (Bahadory and Tarasov, 2018), the one modelling study that did capture both the growth and retreat phases of LGI did so using an EMIC coupled to an ice sheet model (Ganopolski et al., 2010). However, its success depended on the use of an *ad hoc* dust parameterization scheme and temperature bias correction. LCice 1.0 is so far the only fully coupled ice sheet-climate model capable of simulating both the rapid growth and retreat phase of the LGI (Bahadory and Tarasov, 2018) without using any bias correction and *ad hoc* dust forcing. It includes the main feedbacks between the ice sheet and the atmosphere and ocean that have not been resolved in previous

coupled EMIC/ice sheet modelling studies (Bahadory and Tarasov, 2018). It is also fast enough to generate ensembles of glacial cycle timescale transient simulations.

Thus, I employ LCice 1.0 in this study to generate an ensemble of transient LGI simulations to address a series of questions. How did each ice sheet evolve through its inception phase, and which of the two aforementioned paradigms best describes this evolution? More fundamentally, is the spatio-temporal pattern of glacial inception a single attractor in the phase space of possible inceptions, or could small changes in initial conditions or physics properties (*e.g.* mean snow albedo) lead to a different pattern? This question includes an examination of the extent to which the evolution of ice sheets in Eurasia (EA) and North America (NA) are correlated. Expanding this phase space analysis to the climate component, I also examine how the climate conditions (insolation, carbon dioxide, temperature and precipitation) facilitate the rapidity of ice growth and retreat. Besides providing answers to these first-order questions about the LGI, the dataset presented here can contribute to greater understanding of the dynamics of the LGI by raising more questions about the manner in which the climate and ice sheets co-evolve under such wide-ranging conditions.

In section 3.2, I first review LCice 1.0 and its components, and the choice of my parameters for the ensemble study. I subsequently provide the results for my ensemble, and discuss the phasing of LGI in terms of ice sheet and climate evolution.

3.2 Experimental setup

As detailed in Bahadory and Tarasov (2018), ensemble parameters were chosen to reflect key uncertainties in LCice. I ran an ensemble of 500 simulations of LGI for the

North American, Greenland, and Eurasian ice sheets using the coupled model LCice 1.0. These 500 simulations were sieved from a larger ensemble of 2000 simulations covering the pre-industrial to present day interval. Only 55 out of 500 inception simulations could approximately replicate the total pattern of sea level lowering due to ice sheet build up, followed by sea level increase, as suggested by reconstructed proxies of Waelbroeck et al. (2002); Lisiecki and Raymo (2005). The rejected simulations generally underestimated total ice volume, though a small number of simulations captured appropriate growth but with no subsequent retreat phase. For the rest of this paper, the term "ensemble" refers to this sieved group of 55 simulations.

3.2.1 Ensemble parameters and sensitivity analysis

The ensemble approach samples over the parametric uncertainty of the model. The ensemble of simulations presented here are based on varying 18 parameters, 5 of which are found in LOVECLIM, 9 in the GSM, and 4 in the coupler. The LOVECLIM ensemble parameters include snow albedo, bare-ice albedo, melting ice albedo, the humidity threshold for parametrized precipitation, and the cloud parameterization scheme. The GSM ensemble parameters address uncertainties in basal drag, ice calving, sub-shelf melt, and deep geothermal heat flux. Ensemble parameters related to the coupling procedure include spinup length and start time, upscaling method, and the method used to calculate the vertical temperature gradient. Each ensemble parameter and associated sensitivity analysis for the coupled model is described in detail in Bahadory and Tarasov (2018).

3.2.2 Initial conditions

Since the extent of the Greenland ice sheet during the Eemian is not well constrained, the initial state of the ice sheet at the start of the ensemble simulations is set to its present-day configuration. Future work will use an initialization from ongoing Greenland ice sheet model calibration. The initial climatic state is provided by a 3 to 5 kyr LOVECLIM spinup under transient orbital and greenhouse gas forcing, with the present-day topography given as the boundary condition.

3.2.3 Models

3.2.3.1 LOVECLIM

LOVECLIM is a coupled EMIC, consisting of a quasi-geostrophic atmosphere (ECBilt), a primitive equation ocean with dynamic sea ice (CLIO) and dynamic vegetation (VECODE). The atmospheric spatial resolution is T21, and the ocean and sea ice have a resolution of 3°. It is fast enough to simulate LGI (120 ka to 100 ka) in less than 3 weeks using a single commodity core. It has therefore been used to simulate a wide range of different climates from the LGM (Roche et al., 2007) through the Holocene (Renssen et al., 2009) and the last millennium (Goosse et al., 2005) to the future (Goosse et al., 2007).

Interpretation of model-based results always requires cognizance of model limitations. Aside from the simplified atmospheric dynamics and low grid resolution, a key limitation of LOVECLIM for my study is the fixed land-ocean mask. With an inferred LGI maximum sea level drop of approximately 45-65 m, throughflow through ocean gateways can change significantly (including complete closure of Bering Strait).

LOVECLIM is unable to handle a changing land mask, except for the Bering Strait, where throughflow is parametrized as a function of modelled sea level and regional ice sheet cover. Other potentially important factors which can affect the results include simplified radiation and hydrology schemes, and missing feedbacks of dust on radiative forcing.

3.2.3.2 GSM

The glacial systems model (GSM) is built around a thermo-mechanically coupled ice sheet model. It includes a 4 km deep permafrost-resolving bed thermal model (Tarasov and Peltier, 2007), fast surface drainage and lake solver (Tarasov and Peltier, 2006), visco-elastic bedrock deformation (Tarasov and Peltier, 1997a), Positive Degree Day surface mass balance with temperature dependent degree-day coefficients derived from energy balance modelling results (Tarasov and Peltier, 2002), sub-grid ice flow and surface mass balance for grid cells with incomplete ice cover (Morzadec and Tarasov, 2017), and various ice calving schemes for both marine and pro-glacial lake contexts (Tarasov et al., 2012). For the results herein, ice shelves are treated using a crude shallow ice approximation with fast sliding. The GSM runs at 0.5°longitude by 0.25°latitude grid resolution.

3.2.3.3 LCice 1.0 coupler

The LCice coupler is designed to extract, regrid, and exchange the required fields between atmosphere and ocean components of LOVECLIM and the GSM asynchronously (*i.e.* LOVECLIM and the GSM are run sequentially with boundary conditions from the other model fixed between data exchanges). The time between data

exchanges was chosen to be 20 years as the optimal balance in sensitivity tests between efficiency and proximity to shorter coupling timestep solutions (Bahadory and Tarasov, 2018).

Fields passed from the ice sheet to the atmosphere include ice mask and surface elevation, the latter via one of the three included schemes (simple, envelope, and silhouette, the choice of which is under ensemble parameter control). The atmosphere to ice coupling includes the monthly mean and standard deviation temperature and monthly mean precipitation, evaporation, wind direction and magnitude, and vertical temperature lapse-rate. LCice 1.0 uses an innovative scheme to downscale precipitation to the ice model grid that accounts for orographic forcing on the GSM grid resolution topography. Temperature downscaling uses the dynamical (evolving) vertical surface temperature gradient field of LOVECLIM. The coupler also includes a simple radiative cloud parameterization to compensate for the present-day prescribed radiative cloud cover of LOVECLIM.

In ice sheet-ocean interactions, the GSM determines the runoff routing, and passes freshwater fluxes to the ocean model, while the ocean model provides the GSM with vertical temperature profiles, required to calculate sub-shelf melt. Details of each component of the coupling and their influence are described in Bahadory and Tarasov (2018).

Given model limitations, there is no one best run in the ensemble. Instead, different runs have different features, each of which will likely have different patterns of misfits against inferred proxy records. In the following results, I crudely interpret feature frequency in the ensemble to be a partial metric of feature likelihood, though this is far from a rigorous probabilistic analysis.

3.3 Results

The LCice 1.0 ensemble reproduces the reconstructed pattern of rapid ice sheet volume growth and retreat during the LGI in 55 of the 500 runs. The total Northern Hemisphere ice volume averaged over the ensemble of 55 runs is plotted in figure 3.1. No single ensemble parameter is found to explain the difference between runs that achieve this pattern and those that do not, so it appears this response is a result of non-linear interactions between multiple parameters.

The maximum ice volume achieved by the LCice 1.0 ensemble during inception is lower than that inferred by Lisiecki and Raymo (2005), but within the collective uncertainty of the two reconstructions presented here (Waelbroeck et al., 2002; Lisiecki and Raymo, 2005). This under-estimation is likely due in part to the absence of any contribution from the Antarctic ice sheet (and perhaps Patagonian and Tibetan ice caps). Relatedly, the under-estimated maximum ice sheet volume is also consistent with the fact that the simulated ice sheet volumes never reach the peak rate of ice growth indicated by sea level estimates of either reconstruction, and they start to retreat approximately 2 kyr earlier than in the reconstructions. This represents a shorter phase lag between the timing of the sea level minimum and the 60°N summer insolation curve (orange line in figure 3.1) in the simulations compared to the two reconstructions. It is especially striking that the Lisiecki and Raymo (2005) stadial peak occurs almost exactly halfway between the 60°N JJA (mean June July August) orbital minimum at 114.5 ka and the subsequent maximum at 104 ka. Figure 3.1 also includes a sea level reconstruction from the Red Sea (Siddall et al., 2006) which was not used in the filtering process. This reconstruction suggests an even faster decrease

in pre-stadial sea level compared to that of the other two records. Furthermore the timing of the sea level minimum and subsequent sea level rise is slightly advanced of the ensemble mean. The differences between the 3 reconstructions illustrates their collective uncertainty. It is unfortunate that proxy-based sea level reconstructions do not give explicit temporal uncertainties which would enable better evaluation of the phase discrepancies between model- and proxy-based inferences.

A second test of the representativeness of these simulations for the LGI is made between temperature changes from a glaciological inversion of the GRIP ice core δ^{18}O record (Dansgaard et al., 1993; Tarasov and Peltier, 2003) and annual-mean temperatures calculated from the model grid cell containing its location. The ensemble mean 2m temperature anomaly relative to 119 ka follows the general trend of GRIP reconstructed temperatures in figure 3.2 until $\sim$ 112 ka. Individual runs have higher decadal to centennial scale variance than that of GRIP record. However, the large millennial scale variability of the GRIP record inversion is not captured by the simulations. The ensemble-mean annual temperatures from the GRIP site subsequently diverge from reconstructed temperatures after approximately 111 ka. At this time, simulated temperatures increase at the GRIP site following insolation changes, whereas there is no evidence of a similar increase in the GRIP record temperature inversion. Instead, reconstructed GRIP temperatures exhibit multi-millennial timescale oscillations around stable, stadial (cold state) temperatures. It is unclear what mechanism would sustain stadial temperatures over central Greenland under increasing insolation, especially since the simulations consistently predict that strong warming should result. It may be this discrepancy reflects in part a lack of accounting for at least two standard sources of uncertainty in water isotope to temperature inversions:

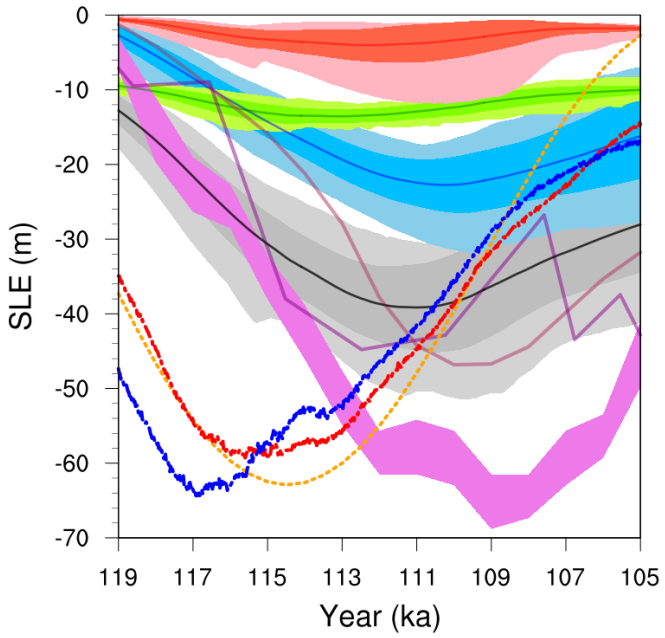

Figure 3.1: The time evolution of total (black), NA (blue), EA (red), and Greenland (green) ensemble mean ice volumes in m sea level equivalent (SLE) between 119 and 105 ka. The dark areas show one standard deviation away from the mean. The light areas show the minimum and maximum ice volumes in the ensemble. The purple area, light purple, and dark purple lines show the respective proxy-based sea level reconstructions from Lisiecki and Raymo (2005), with 1 sigma, Waelbroeck et al. (2002), and Siddall et al. (2006). The orange line depicts the timing of insolation changes at 60°N. The JJA ensemble mean temperatures over 50°N-65°N of NA and 60°N-75°N of EA are shown as thick-dotted blue and red lines, respectively.

changes in the moisture source region and changes in the seasonal distribution of precipitation.

3.3.1 Glacial inception phase-space

Now that I have established that LCice 1.0 is able to capture both the ice sheet growth and retreat phases of the LGI, I explore how consistent the patterns of the ice growth and retreat are between ensemble members. I start by analyzing the spatial patterns of EA and NA ice sheets at two diagnostic time intervals: first, the early stage of ice build up, and second, during the peak of the inception around 112 ka. Next, I explore the consistency of ice and climate evolution between these two intervals and during the subsequent retreat phase.

3.3.1.1 Spatial pattern of first appearance of ice

Despite having different start times (due to different calendar start years between 122 ka and 119 ka and spinup lengths varying between 3 to 5 kyr), all simulations start growing ice in the first 100 years of simulation (figure 3.3.a). Therefore, I analyse the spatial patterns of the first appearance of ice in the first 1000 years of simulation, rather than aggregating simulations according to a common calendar year.

In NA, the patterns of initial ice build-up are highly consistent over the Canadian Archipelago and Ellesmere island, but differences arise in central Canada and the Rockies during the first 1 kyr of simulation (figure 3.3). Land ice first appears in NA over the Canadian Archipelago (especially Ellesmere and Devon Islands) in all runs, while the Rockies and eastern NA are almost ice-free (figure 3.3.a). This is in agreement with studies that suggest the first ice nucleation in NA occurs over the

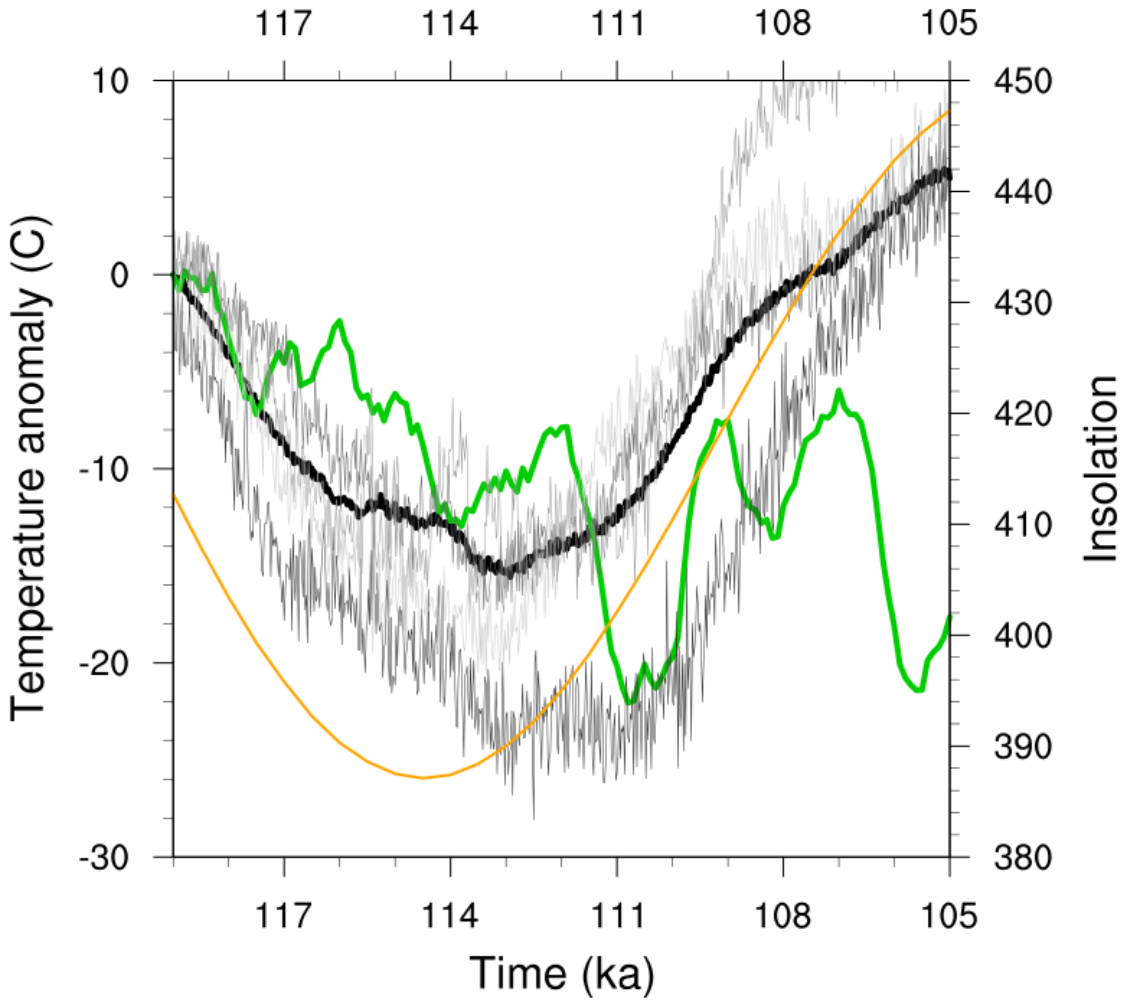

Figure 3.2: Annual mean 2 m temperature anomaly relative to PD for the GRIP ice-core (green) (Dansgaard et al., 1993; Tarasov and Peltier, 2003), ensemble mean (thick black), and three individual runs (gray lines). The orange line depicts the timing of insolation changes at 60°N.

Canadian Archipelago with further growth, merger, and then expansion to southern and western regions (Weertman, 1964). This result is also consistent with the ongoing presence of extensive glaciers and small ice caps in this region.

Within approximately 500 years, ice expands southward over Baffin Island and westward over the western Canadian Archipelago, and it also begins to nucleate over central northern Canada and high-elevation regions of the Rockies in some of the runs. The appearance of ice over central northern Canada supports the widespread snowfield thickening paradigm by Calov et al. (2005). After 1 kyr, the smaller ice caps in the Canadian Archipelago start merging, and the eastern margin of Baffin Island becomes fully ice-covered in all the simulations. In the simulations with most extensive ice, the Cordilleran ice sheet over the Rockies merges with the Innuitian ice sheet over the Canadian Archipelago to form a single ice complex. However, in most runs, central northern Canada, the eastern Rockies and northern Labrador and Quebec remain ice-free. Thus, the first 1 kyr of my results suggest a combination of the two paradigms contributing to initial appearance and spreading of ice.

The evolution of EA ice has more cross-ensemble variability compared to that of NA. It has long been understood that EA ice is more sensitive to orbital forcing and climate variations (*e.g.* Tarasov and Peltier, 1997a) due to the smaller size of the EA ice sheet and related higher margin length to area ratio. In EA, ice growth begins over Svalbard within the first 100 years of simulation, with the most extensive simulations also showing ice cover over other islands in the region. Once Svalbard is completely covered with ice and there is some ice cover on most of the islands in the region, ice growth shifts southward to the high-elevation regions of mainland Fennoscandia. (figure 3.3.a and b). By the end of 1000 years of simulation, the higher elevation

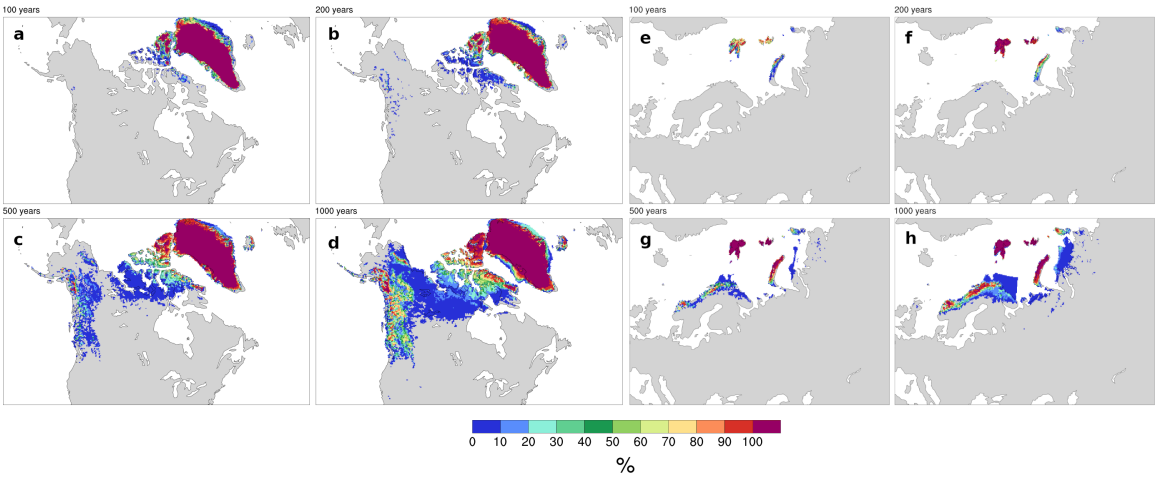

Figure 3.3: **Left**. NA ice thickness ensemble probability distribution after **a** 100, **b** 200, **c** 500, and **d** 1000 years of simulation. **Right**. EA ice thickness ensemble probability distribution after **e** 100, **f** 200, **g** 500, and **h** 1000 years of simulation.

regions of Fennoscandia are ice-covered in the majority of runs, but there is still little evidence of ice cover over the Barents and Kara Seas, northern Russia, or at latitudes south of 65°N. Even in the simulations with the most extensive EA ice cover, there is no single ice sheet present over continental EA by this time.

3.3.1.2 Spatial pattern of the Last Glacial Inception maximum ice

To capture the maximum in ice volume for EA and NA during the LGI, I consider time slices for 114 ka, 112 ka, 110 ka and 108 ka in figures 3.4 and 3.5. I aggregate my simulation results according to their boundary condition years rather than their simulation years.

The NA ice sheet extent prior to and at the peak time is generally consistent between runs, with ice covering the Rockies and central and northeastern Canada including Hudson Bay (*cf.* figure 3.4). The Greenland and Iceland ice sheets are con-

nected in all runs by 114 ka. Also, Alaska is fully ice-covered in all of the simulations, while Labrador and eastern NA remains ice-free, likely due to warm model biases in this region. The main differences between ensemble members occur along northern Alaskan ice margins (with 40% of ensemble runs covering Bering Strait at 114 ka), southern Canada, and Baffin Bay, where approximately 80% of simulations create an ice bridge connecting the Laurentide and Greenland ice sheets across Davis Strait. This ice bridge generally starts out from a merger of opposing ice shelves. For some (but not all) ensemble runs, it can also ground right across the Strait and therefore isolate Baffin Bay from the Labrador Sea.

After the stadial peak in NA ice volume, the main variation between ensemble members appears in the rate of ice retreat. Initially, while the ice margin rapidly retreats to higher latitudes along the south-eastern margin in simulations with smaller ice sheets, simulations with larger ice sheets show little change in ice extent. This difference in behaviour leads to the largest difference in ice extent over Hudson Bay at 110 ka, when approximately 20% of the simulations cover the entire area and 30% are ice-free in this region. By 108 ka, the Laurentide and Cordilleran ice sheets are separated in only 10% of the simulations, fewer than 20% of runs simulate a connected Greenland-Iceland ice sheet, and the ice bridge across Davis Strait has also disappeared in more than 90% of runs.

Similar to the early phases of the inception, ice extent over EA is more variable between ensemble members around the stadial peak time (116 ka to 112 ka) compared to NA (figure 3.5). At this time, fewer than half of simulations develop a single ice sheet in the northern mainland of EA, while the rest of the runs display multiple distinct ice domes over Scandinavia, Svalbard, Novaya Zemlya, and northern Siberia.

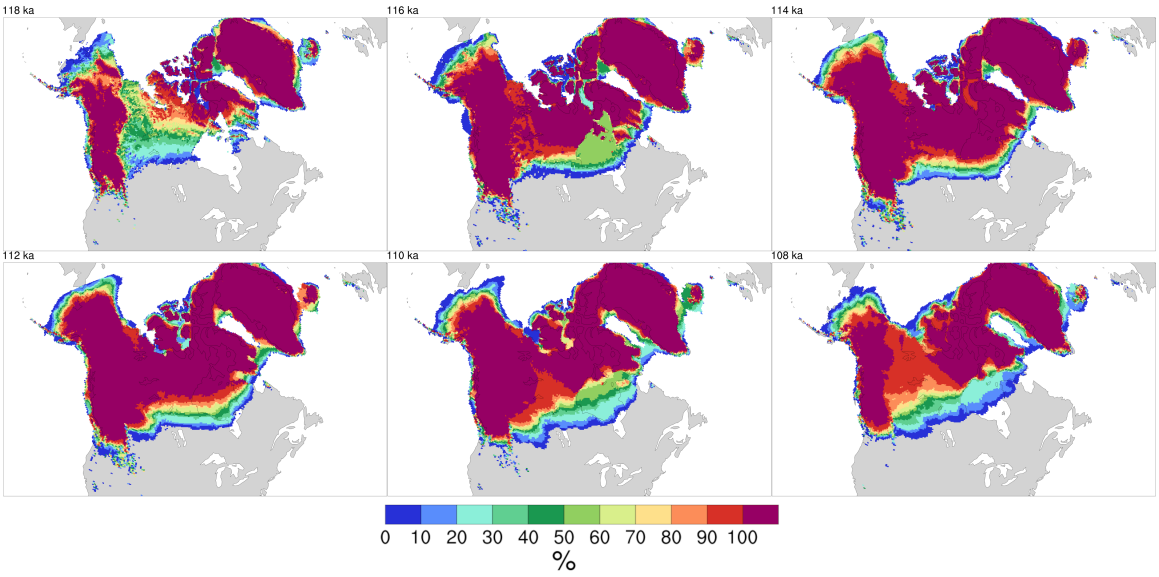

Figure 3.4: NA ice thickness ensemble probability distribution at **a** 118 ka, **b** 116 ka, **c** 114 ka, **d** 112 ka, **e** 110 ka, and **f** 108 ka. The 118 ka and 116 ka are included to provide the history before the peak and are not discussed.

Scotland exhibits some ice cover in the majority of runs, but the North Sea remains ice-free. As with the ice sheets in NA, the larger EA ice sheets retreat after 112 ka more slowly than the smaller ones do, but fewer than 10% of runs have a single Fennoscandian ice sheet by 108 ka (figure 3.5f).

3.3.2 Temporal pattern of ice evolution across the ensemble

As shown in the previous section, the patterns of ice growth and retreat are not consistent through the LGI in all regions, especially in EA. The speed with which regions become ice-covered and ice-free vary between ensembles members for both the NA and EA. To diagnose the development of these ensemble member differences in time, I subdivide NA and EA into four sectors each (outlined in figure 3.6) and

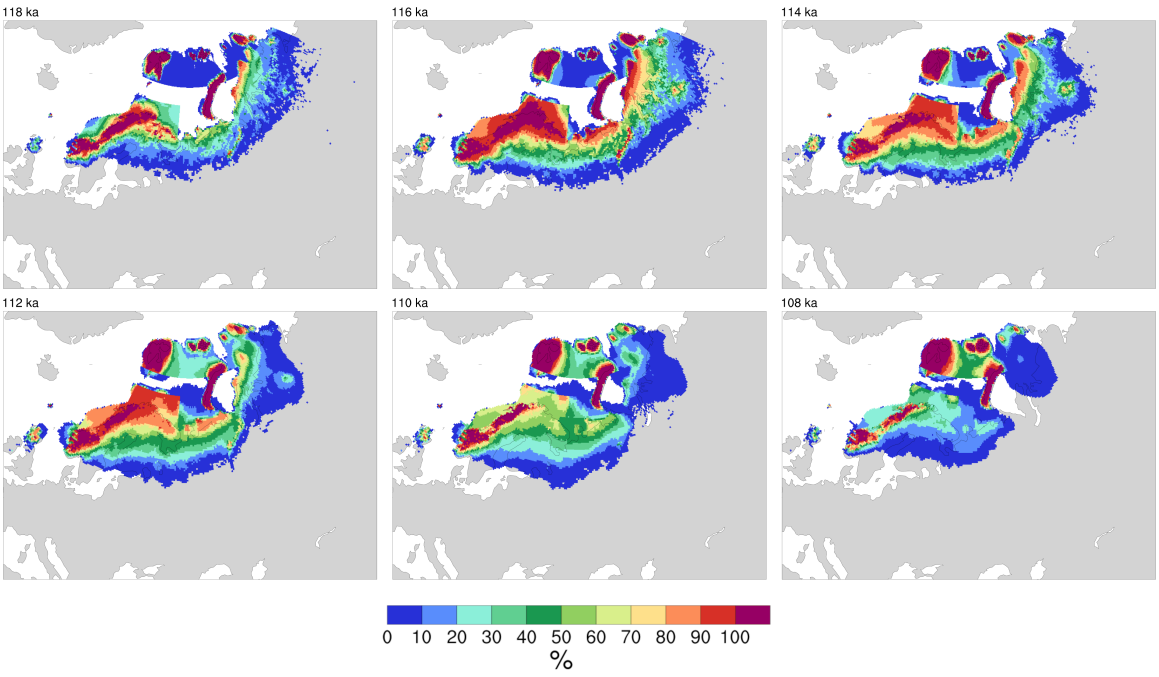

Figure 3.5: EA ice thickness ensemble probability distribution at **a** 118 ka, **b** 116 ka, **c** 114 ka, **d** 112 ka, **e** 110 ka, and **f** 108 ka. The 118 ka and 116 ka are included to provide the history before the peak and are not discussed.

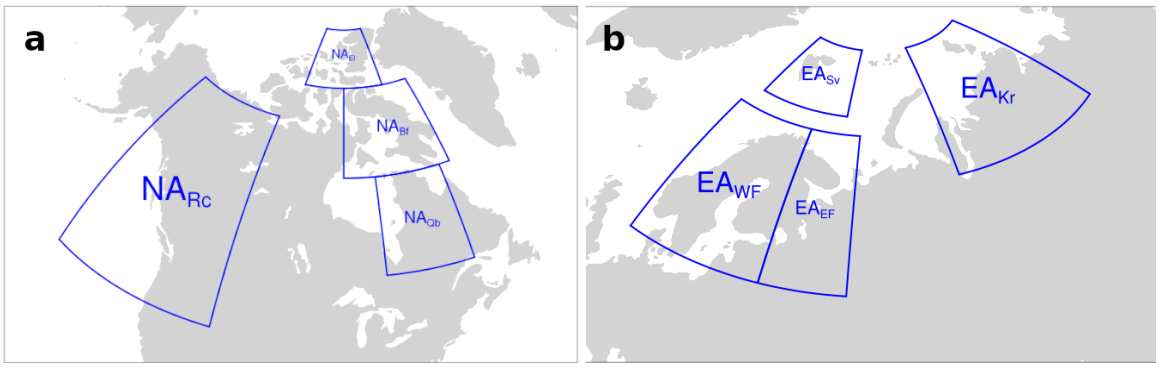

Figure 3.6: **a**. NA subregions, and **b**. EA subregions

examine the evolution with time of ice volume in each sector.

The NA sectors include the Canadian Archipelago separated into Ellesmere Island (NA_{El}) and Baffin Island (NA_{Bf}), Quebec (NA_{Qb}), and the Rockies (NA_{Rc}). The EA sectors include the north-western Barents Sea and Svalbard (EA_{Sv}), the Kara Sea and nearby land (EA_{Kr}), and eastern and western Fennoscandia (EA_{EF} and EA_{WF}).

3.3.2.1 North American ice sheet

In all regions in figure 3.7 except NA_{El}, ice volume increases to a maximum sometime between 112 ka and 109 ka and then decreases. In NA_{El}, the coldest region of NA, ice volume increases throughout the LGI in most simulations. Generally, the ice sheet growth phase is more consistent between runs than its retreat phase. In sector NA_{Bf} in figure 3.7b, $\sim$10% of simulations lose between 1 and 1.5 m SLE of ice between 112 and 107 ka and maintain a constant ice volume afterwards. The rest of the runs show a range of behaviors, from almost no ice loss to 80% loss. In contrast, in NA_{Qb}, the most southern and warmest subregion, the maximum ice volume varies between almost zero to more than 1 m SLE, and no simulation sustains ice cover until the

end of the LGI. The NA_{Rc} region spans the widest range of latitudes, but it also contains some of the highest-elevation sites of NA. It shows both strong ice growth and a wide range of ice loss scenarios over the LGI. Notably, ice develops over western NA (NA_{Rc}) at the same time as it is growing in the east.

One pattern that emerges most strongly in NA_{Qb} is that the runs with larger ice sheets tend to have delayed peak times. This is consistent with the observation in the previous section that runs with the largest NA ice sheet extent had a delayed retreat time relative to the smaller ice sheets.

3.3.2.2 Eurasian ice sheet

In EA, the most northern (and coldest) sector, EA_{Sv} has steadily increasing ice volume throughout the LGI. This pattern is similar to that observed for NA_{El}. Otherwise, the rest of EA sectors show ice growth and retreat patterns similar to NA_{Qb}, where there is a wide variation in the total ice volume reached and (near-) complete ice loss by the end of the LGI. These regions also reproduce the tendency for larger ice sheets to have later peak ice volumes, ranging between 114 and 110 ka.

3.3.3 Relationships between changes in the North American and Eurasian ice sheets

I have examined the build-up and retreat of ice sheets in NA and EA independently. Past modelling studies indicate that the presence of NA ice can affect conditions over EA (Beghin et al., 2013; Colleoni et al., 2016; Liakka et al., 2016; Ullman et al., 2014; Kageyama and Valdes, 2000) and therefore potentially EA evolution. Thus, I consider

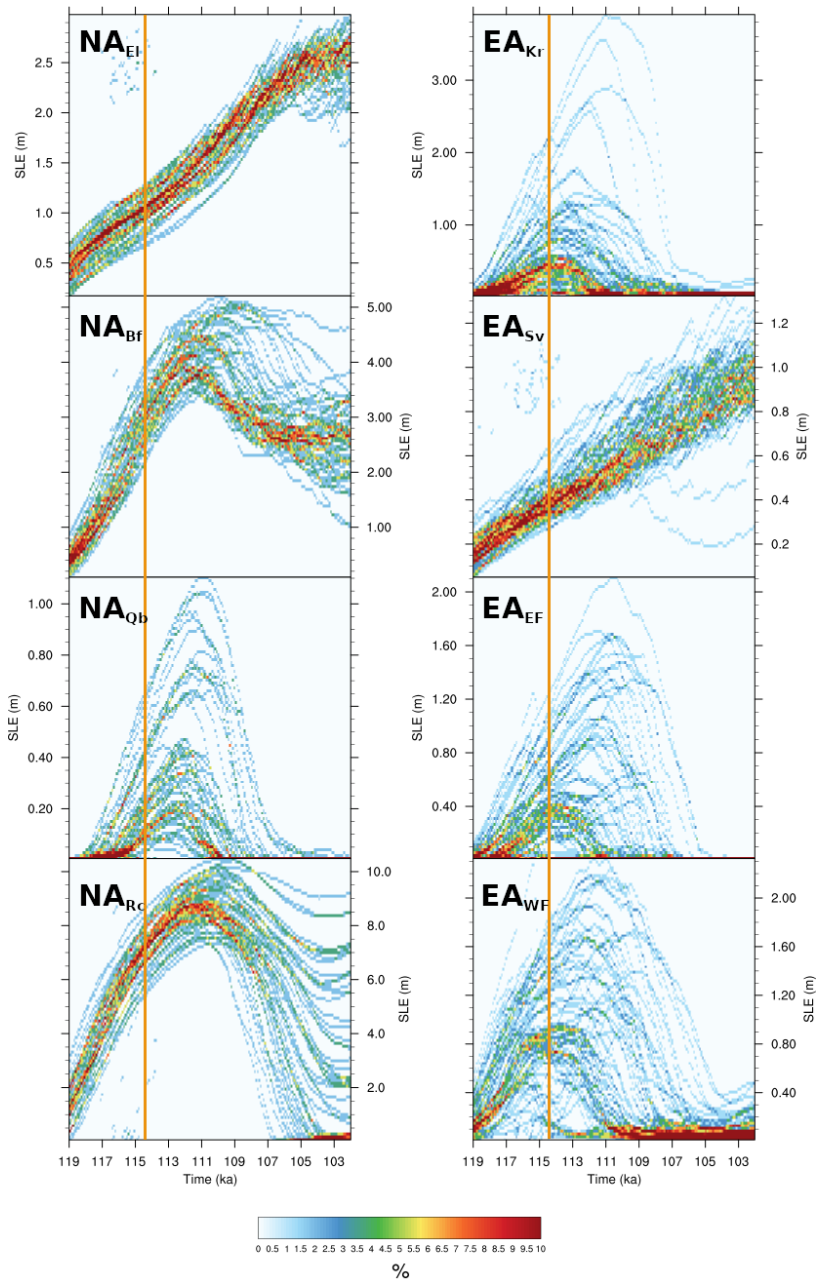

Figure 3.7: **Left**. NA ensemble distribution of ice volume during LGI in NA_{El}, NA_{Bf}, NA_{Qb}, and NA_{Rc}. **Right**. EA ensemble distribution of ice volume during LGI in EA_{Kr}, EA_{Sv}, EA_{EF}, and EA_{WF}. The vertical orange line shows the timing of the minimum summer insolation at 60°N.

next whether there is any evidence for such a relationship acting in this ensemble.

Comparisons of EA maximum ice volume versus NA maximum ice volume in figure 3.8 indicate that there exists no simple relationship between these two fields. Small NA ice volumes correspond to small EA ice volumes. However, when NA ice volumes are larger, figure 3.8 suggests a possible bifurcation in the runs. More ensemble runs would be required to validate this suggestion.

Although there is no clear connection between the volumes of NA and EA ice sheets, there is a relationship between the timing that the peak ice volume is reached in these two regions in most ensemble members. In figure 3.9a, the peak ice volume nearly always occurs earlier in EA than in NA. This result is expected given the smaller size and related stronger sensitivity of the EA ice sheet to orbital forcing. The duration of this lead depends strongly on model parameters and ranges between 200 years to 6 kyr. In a small subset of runs, the EA ice volume peaks early ($\sim$115 ka) regardless of the timing of the NA ice volume peak (possible further evidence of the aforementioned possible bifurcation).

The correlation in the timing that maximum ice volumes are reached in NA and EA in most runs in figure 3.9a may indicate that these ice sheets are affecting each other's growth and retreat, or it may indicate that the parameter choices that lead to larger ice sheets in one region also encourage growth in the other. One plausible mechanism whereby the NA ice sheet may affect the development of the EA ice sheet is through a reduction in hemispheric temperatures. However, there is no evidence of this, as the timing of maximum EA ice volume (figure 3.9c) has no consistent phase relationship with the timing of EA minimum temperature. Thus, if there is a means by which the NA and EA ice sheets are affecting each others' development, it is not

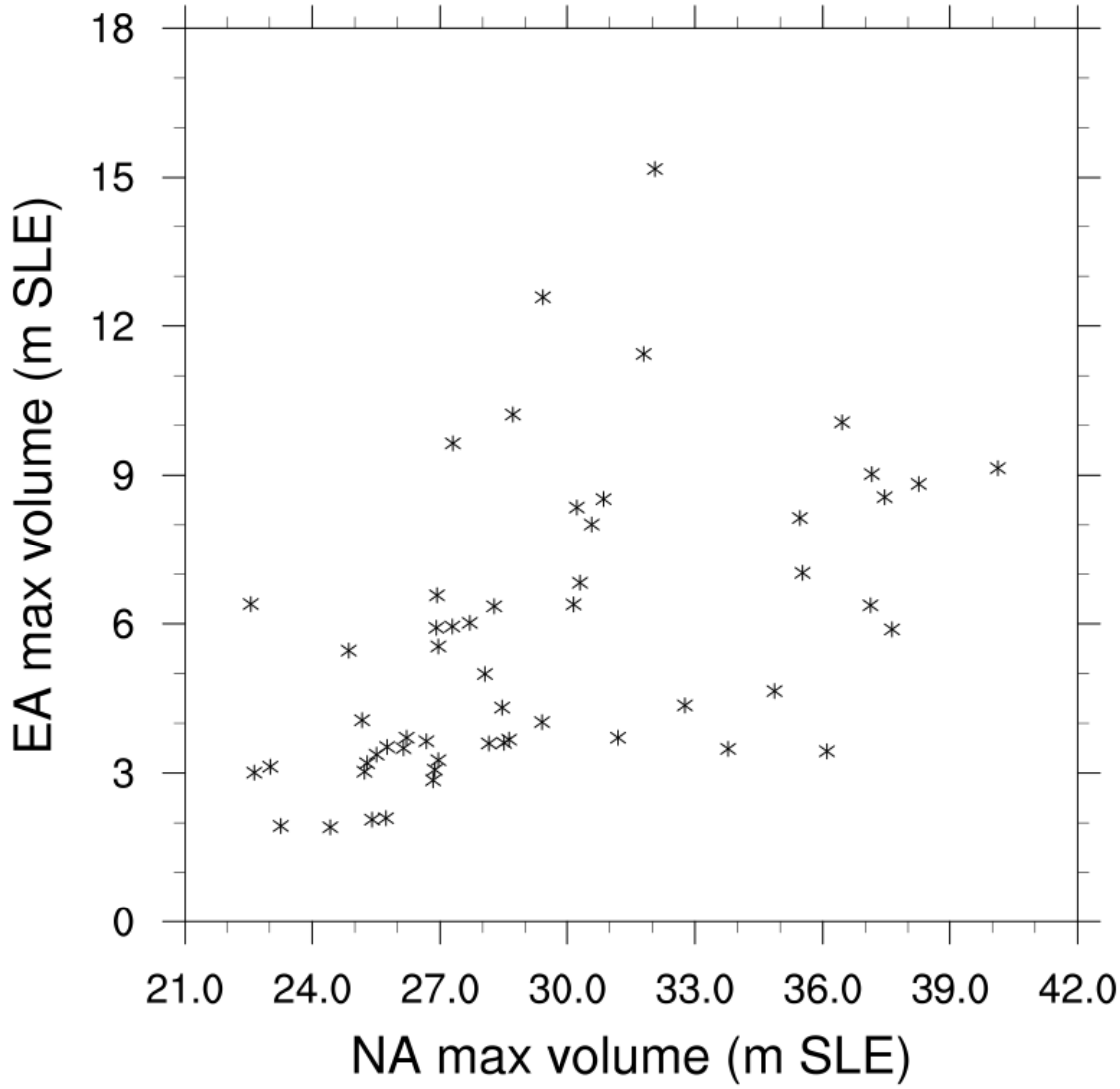

Figure 3.8: The maximum volume of the NA and EA ice sheets for individual runs.

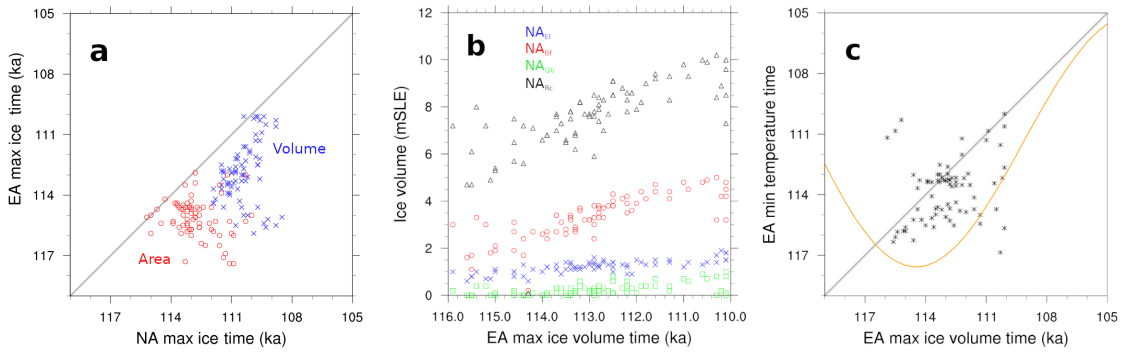

Figure 3.9: **a**. Timing of the EA ice volume (blue) and area (red) peak with respect to the NA peak time. **b**. Ice volume in NA sectors at the time of EA maximum ice volume. blue: NA_{El}; red: NA_{Bf}; green: NA_{Qb}; black: NA_{Rc}. **c**. Timing of the EA minimum temperature and maximum ice sheet volume for individual runs. The orange curve shows the summer (JJA) insolation at 60°N.

clear from the results here. Additional experiments to isolate the impact of each ice sheet on the other one are analyzed in Chapter 4.

3.3.4 Climate of the Inception

Having documented the phase space of ice sheet changes and identified the more robust features in my ensemble of LGI simulations, I now consider relevant controls from the climate system. To that end, I focus on temperature and precipitation as the two main controls on ice sheet thickness and extent (at least for terrestrial components). These are themselves affected by Northern Hemisphere sea ice (which alters the exchange of heat and moisture between the atmosphere and ocean), the AMOC (through changes to oceanic heat transports to high latitudes), and the latitude of the jet stream (through changes to atmospheric heat transports and the locations of

storm tracks).

Northern summertime temperature and annual precipitation are ice-sheet relevant climate characteristics that most directly control ice sheet extent and thickness. For my ensemble, both temperature and precipitation of NA and EA (figure 3.10) show abrupt reductions early in the LGI interval initially in phase with the reduction in insolation at 60°N. In NA, temperature and precipitation reach their respective minimum values approximately 2.5 kry and 1.5 kyr earlier than insolation. A weakening influence of insolation changes at this point is expected. Since the relatively high albedo ice sheets and sea ice tend to be fairly extensive by this time (figures 3.4, 3.5 and 3.10), insolation will be a smaller contributor to the regional energy balance. But to actually explain the phasing of the temperature minimum relative to the insolation minimum, other contributors must be invoked. An increase in the radiative forcing from the atmospheric concentration of CO_2 (purple timeseries in 3.10) after 116.5 ka and especially a subsequent decrease after 114.5 ka approximately correspond with the interval of discrepant NA mean summer temperature change (relative to insolation forcing). The possible role of changes in AMOC and sea ice cover are examined below.

Why NA temperature resumes warming shortly after its minimum at $\sim$ 117 ka is not clear. However, it continues to increase throughout the remainder of the period with a brief hiatus at $\sim$ 114 ka.

Thus, the early stages of ice growth in NA appear to be dominated by ice sheet expansion in response to regional cooling, since precipitation is decreasing. In snapshots of near-surface temperature and ice sheet elevation from a single simulation in figure B.5, the ice sheet margins during this time tend to be located between the -2°C

to 2°C isotherms in most regions except for those with high levels of accumulation (*e.g.* the Rockies). NA ice sheet area reaches its maximum between 114 and 113 ka, when both temperature and precipitation are increasing (see figures 3.9a and 3.10). However, the NA ice volume continues to grow until approximately 111 ka through a thickening of the ice sheet (*cf.* supplemental figure B.5) in response to increasing precipitation under continuing cold temperatures. Eventually, the NA ice sheet begins to lose mass after further increases in temperature and precipitation. At this time, the southern margins of the ice sheets tend to fall between the 0°C and 4°C isotherms, and the ice sheets retreat from the south while remaining otherwise thick. In this way, the ice sheet growth and retreat phases are asymmetrical.

In EA, temperature and precipitation also show an abrupt but weaker reduction in the early inception. The ensemble mean EA summer temperature and precipitation minima have a longer duration interval than that of NA. EA temperature and precipitation gradually increase until ∼111 ka, when the sea ice area starts to decline. After this time, both temperature and precipitation increases accelerate.

In assessing the contributions of sea ice, the AMOC and the jet stream, summer sea ice has the strongest correlations with temperature and precipitation changes in EA. Late winter sea ice shows no consistent pattern of change over this time period and is not related to ice sheet volumes in either NA or EA (see supplemental figure B.1). However, its summer extent varies in correspondence with Northern Hemisphere temperatures: it peaks prior to the minimum in insolation at 60°N, remains extended, and then decreases. The onset of major sea ice retreat at approximately 111 ka is in phase with a rapid acceleration of both NA and EA summer warming and annual-mean precipitation. Deciphering the causal relationships of this phasing requires

future sensitivity studies. However, at the very least, one can infer that sea ice has a positive feedback role for both precipitation and temperature at this time.

Neither the AMOC nor the jet stream exhibit any consistent changes that coincide with temperature and precipitation or ice sheet changes. In 80% of the runs, the AMOC gradually increases during the glacial inception to a maximum of 22 Sv around 108 ka. After this, it decreases once more to its initial values of 16 to 18Sv. In the remaining 20% of runs, the AMOC oscillates between two values. Similarly, there are no evident changes in the latitude of the North Atlantic jet stream in any of the runs. Previous work indicates that the position of the North Atlantic jet stream depends on the latitude of the south-eastern margin of the NA ice sheet (Andres and Tarasov, 2019). For the current ensemble, the NA ice sheet remains north of the preferred latitude for the jet stream at all times, so the ice sheet is unable to directly influence the jet stream in this way.

3.3.5 Discussion

The first appearance of ice on land in NA is as early as 119 ka over Ellesmere Island. This is consistent between all runs and consistent with present-day ice cover. From there, it spreads south to Baffin Island and west over the rest of the Canadian Archipelago. However, within 500 years of simulation, it also begins to nucleate over central north Canada in some of the simulations. Ice appears on high-elevation regions of the Rockies at this point as well in some of the runs. In the most ice extensive runs, the Cordilleran and Innuitian ice sheets merge across central northern Canada to form a single Laurentide ice sheet within 1000 years. Considering the first appear-

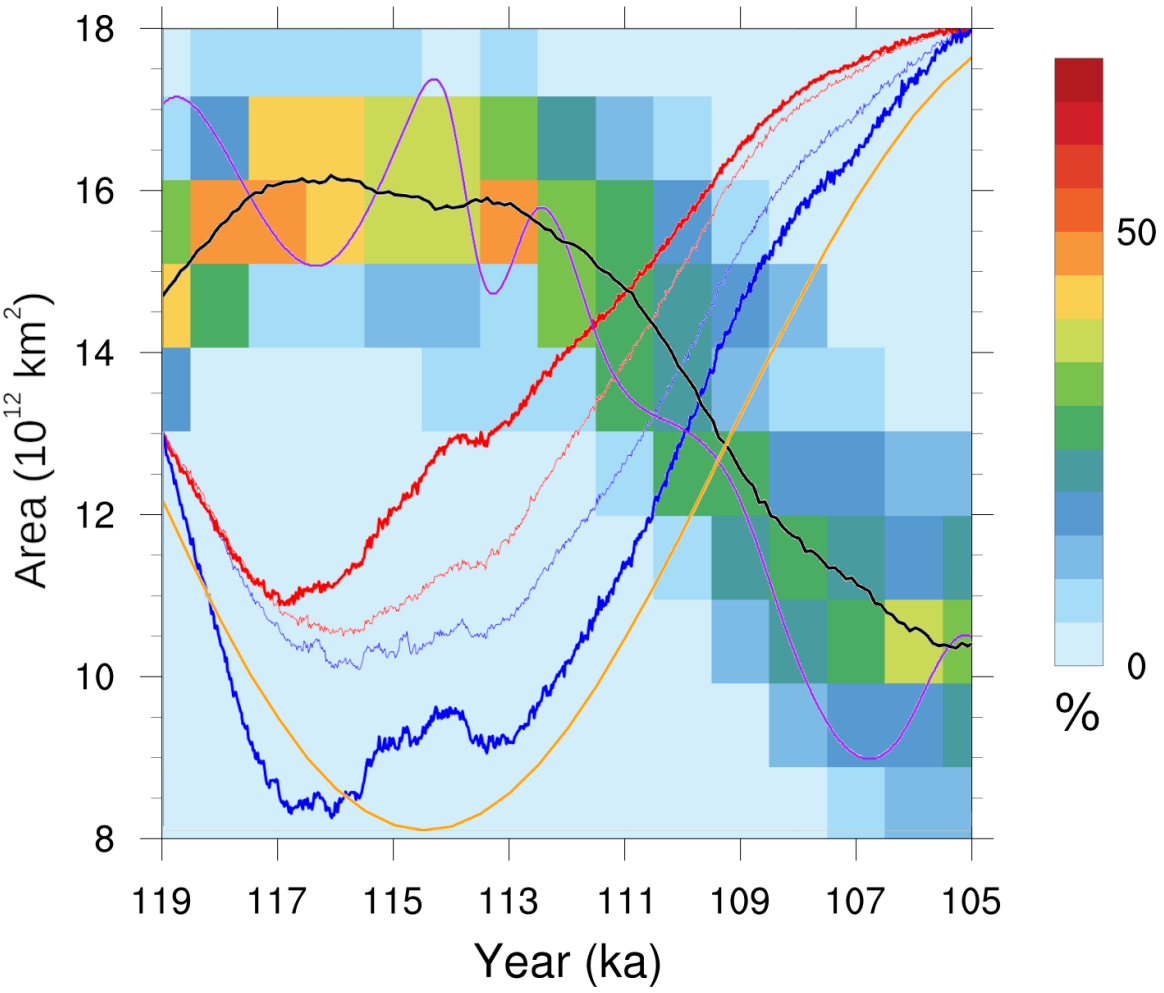

Figure 3.10: The ensemble distribution of Northern Hemisphere late summer sea ice total area. The black line shows the ensemble mean sea ice area. The blue lines show the scaled ensemble mean summer temperature anomaly with respect to 119 ka in NA (thick) and EA (thin). The red lines show the scaled ensemble mean annual precipitation anomaly with respect to 119 ka in NA (thick) and EA (thin). The orange line represents the summer insolation at 60°N. The purple line shows the changes in $\log(CO_2)$ to approximately capture its effective radiative forcing. Temperature, precipitation, insolation, and CO_2 are plotted solely for the sake of phase comparison, and therefore their actual values are not indicated.

ance of ice in the Canadian Archipelago in all runs, and inconsistent nucleation of ice in central north Canada prior to merger of the Canadian Archipelago ice caps, these results support a combination of the two hypotheses of glacial inception. Specifically, inception starts with nucleation in high latitudes and high elevations with subsequent relatively fast snowfield spreading across northern Canada. By the inception peak, a single ice sheet covers Canada, parts of the northern United States, and Alaska in all runs, with ∼80% of runs covering Davis Strait with an ice bridge. After the inception peak, all NA sub-regions except NA_{El} lose ice, while ice in NA_{El} grows with a smaller rate.

Over EA, there is a much greater contrast than over NA between the runs with the most and least extensive ice cover. Ice initially forms over Svalbard, Novaya Zemlya, and Spitsbergen. It then expands to more southern-located islands, followed by high-elevation sites in northern Fennoscandia and northern Russia. There is no contiguous Barents/Kara ice sheet, but there is some eastward filling of the northern Baltic Sea from what is now Sweden. The absence of continental shelf ice expansion is perhaps due to some combination of higher sea level and uncertainties in the GSM marine ice treatment (*e.g.* with respect to grounding line advance). Similar to NA_{El}, ice in EA_{Sv} continues to grow through the inception interval. The pattern of ice evolution in lower latitudes becomes more variable across the ensemble by the start of the retreat phase. However, most EA sub-regions except EA_{Sv} completely lose ice by the end of the inception.

Maximum NA and EA inception ice volumes are not well correlated across the ensemble. In simulations where NA ice volume tends to be small, the EA ice volume also tends to be small, but there is no such clear connection for intermediate- to

large-sized ice sheets. However, I do find that the EA ice sheet consistently reaches its maximum ice volume prior to the NA ice sheet, although the time lag is quite variable between runs (200 yr to 6 kyr). Chapter 4 examines in detail the impact of the NA and EA ice sheets on the evolution of each other.

I performed an initial assessment of the influence that climate fields play in LGI ice sheet evolution. At the beginning of the LGI, temperature and precipitation over NA and EA decrease steadily and the summertime sea ice area expands. The consequent southward shifting of JJA isotherms ranging between -2°C and +2°C drives the areal expansion of the NA ice sheet southern margin, and likely that of EA as well. Both NA and EA mean summer temperature and mean annual precipitation reach their LGI minimum in approximate synchrony with the time of late-summer maximum Northern Hemisphere sea ice area, and slightly in advance of the JJA 60^o N insolation minimum. The subsequent increase in precipitation occurs relatively abruptly over NA, unlike the increase in temperature and decrease in late-summer sea ice area. During this time, the NA ice sheet area remains extended and its volume continues to increase through ice thickening.

EA mean summer temperature and mean annual precipitation on the other hand do not increase during this period until the sea ice area starts to decline. Due to this controlling effect by sea ice, there is no equivalent period of thickening for EA, and its retreat begins much sooner after the minimum in insolation than for the NA ice sheet. Unexpectedly, in a small subset of runs, the EA ice sheet begins to retreat prior to the minimum in insolation at 60°N and prior to its local minimum in summer temperatures. By 111 ka, insolation, northern summer temperatures and annual precipitation all increase rapidly, and summertime sea ice extent decreases

rapidly. At this time, both EA and NA retreat rapidly. With a stronger influx of upstream ice during its retreat (especially compared to its initial growth), the NA ice margin now lags the northward displacement of the -2 to +2°C isotherms.

3.4 Conclusions

This is the first study to examine possible patterns of ice sheet growth and retreat during the LGI in a coupled ice and climate model only subject to orbital and GHG forcing. I used LCice 1.0, a coupled ice sheet and climate model, to generate an ensemble of 500 transient simulations of the LGI that differ according to the combination of parameters and parameterizations used in the climate component (LOVECLIM), the ice sheet component (the GSM) and the coupling between them. Of these 500 simulations, 55 simulations reproduced the reconstructed patterns of sea level changes during the LGI. In this paper, I document the patterns of ice growth and retreat exhibited by North American and Eurasian ice sheets in these 55 runs.

I applied two tests of the representativeness of these simulations to historical changes during the LGI: comparisons of total sea level changes with time, and comparisons of near-surface air temperatures at the location of the GRIP ice core. Maximum LGI ice volume is under-estimated in the ensemble relative to that inferred by Lisiecki and Raymo (2005), although it lies within the collective uncertainties of reconstructed values (especially after accounting for the absence of an Antarctic component in the model). Another possibly significant discrepancy is the timing of the LGI sea level minimum, with my model ensemble sea level minimum occurring approximately 2kyr earlier than that of the Lisiecki and Raymo (2005) and Waelbroeck

et al. (2002) reconstructions. Part of this discrepancy may be due to the absence of a modelled (and likely out of phase) Antarctic ice sheet contribution in LCice 1.0, but part may also be due to dating uncertainties in the proxy based reconstructions.

The ensemble mean temperature is in approximate agreement with an inverse reconstruction from the GRIP ice core during the cooling phase of the inception. Subsequently, a strong warming in the model driven by orbital and greenhouse gas forcing is absent in the reconstruction. Given regional warming is robust across the ensemble and the lack of a plausible physical mechanism to sustain cold, stadial conditions under increasing insolation, I suggest the discrepancy may be due in part to uncertainties in the δ^{18}O to temperature inversion. The model also fails to capture the millennial scale variance of the proxy record.

One of the main questions addressed by this study is whether there is a single likely evolution of ice configurations during the LGI or whether the evolution is sensitive to model parameters. My results indicate that the ice evolution pattern is different in the two continents, and also varies between the growth and retreat phases.

The regional LGI pattern of ice evolution for NA and EA starts with the high elevation and high latitude nucleation paradigm (first over Ellesmere Svalbard and Franz Joseph islands, then the northern Rockies, and Baffin and Novaya Zemlya islands). Subsequent nucleation over lower latitudes is followed by wide snowfield expansion/thickening over central northern Canada, merging eastern and western NA ice in all runs.

The EA ice sheet is more sensitive to ensemble parameters, and varies between a single ice sheet to multiple ice caps at its peak volume. The peak in the EA ice sheet's volume occurs prior to the NA ice sheet in all runs. After the LGI ice volume peak,

retreat happens across most sectors except for continued (though slower) growth in the most northern Ellesmere and Svalbard sectors. Aside from the latter, EA tends to have almost complete ice loss by 104 ka. The post-LGI stadial ice mass loss rate and temperature and precipitation increases in EA have higher correlation with sea ice retreat compared to that for NA ice, temperature, and precipitation.

Two perhaps novel features pertaining to NA and Greenland may be of interest to glacial geologists. The Greenland ice sheet and Icelandic ice cap are connected in all runs by 114 ka. Furthermore, there is an ice bridge between NA and Greenland across Davis Strait in approximately 80% of ensemble runs.

An intended contribution of this study is its ability to foster new research about LGI. I will make a subset of the simulations described in this paper publicly available via an online archive for other groups to use. I especially hope that the field data community will use this archive to test, refute, and/or validate which, if any, of the model-derived trajectories (and characteristics thereof) for LGI are consistent with the paleo record.

Chapter 4

The role of the Northern Hemispheric Ice Sheets in Last Glacial Inception

Abstract

I examine the dynamical role of the Northern Hemisphere ice sheets during the last glacial inception. Specifically, I compare the impact of various climate mediated feedbacks of the evolving ice sheets upon themselves and each other. My analysis is based on sensitivity ensembles using the fully coupled ice sheet - climate model LCice 1.0 (Bahadory and Tarasov, 2018).

Within the context of the orographic and thermal impacts of the Northern Hemispheric ice sheets, I find moderate to high sensitivity of the Eurasian (EA) ice sheet to the configuration of the larger North American (NA) ice complex (with up to 10 % ensemble mean variations at peak inception and close to factor 3 variations during the subsequent retreat). The topography and extent (via

albedo) of the North American ice sheet impacts the strength and location of the North Atlantic low pressure system, temperature and precipitation patterns, and therefore the ice distribution over EA. Due to a combination of their relative sizes and the much larger upstream distance, the NA ice complex is less sensitive to the size of the EA ice sheet (less than 5% in ice volume), unless the EA ice sheet extent and thickness is fixed at its inception maximum. This latter case is the only experiment to lack a deglaciation phase over the 120 ka to 105 ka interval.

With regards to ice-ocean interactions, both termination of Bering Strait throughflow or shutdown of freshwater runoff from the ice sheets, strengthens the Atlantic Meridional Overturning Circulation inducing the largest reduction in Northern Hemisphere ice sheet volume of all of my experiments. In all these experiments, the response of the Eurasian ice sheet is much stronger than the NA ice sheet, both in terms of total ice volume and regional ice distribution differences.

4.1 Introduction

The last glacial inception is a period of rapid ice sheet build-up of about 45 m to 65 m sea level equivalent (mSLE) within the 120 to ∼110 ka interval, with subsequent 10 kyr of ice retreat. This relatively rapid transition into and partly out of glacial conditions offers a stringent test of our understanding and representation of the climate system in computer models and their sensitivity to orbital and greenhouse gas (GHG) forcing.

To date, only one study relying on just orbital and GHG forcing has captured this fast growth, and subsequent retreat (Bahadory and Tarasov, 2018). This model is to

date arguably distinguished for this context by the explicit incorporation of most of the key feedbacks between ice sheets and climate. I posit that this is a key reason for the success of this study. Simply put, the evolving ice sheets have a major impact on glacial inception climate that previous studies have inadequately captured. Herein I examine and to an extent quantify this impact and how it feeds back onto ice sheet evolution. This examination may be better understood by first listing the processes that make up these feedbacks.

Ice sheets have four main impacts on the rest of the climate system. First, through evolving extent of relatively high albedo ice, ice sheets can change the regional radiative balance. Second, their changing topography (along with a smaller order impact from their induced changes on surface roughness) can alter atmospheric circulation. Analyses using general circulation climate model simulations indicate that the presence of the Laurentide ice sheet can split the jet-stream into a weaker northern and much stronger southern branch (Kutzbach and Guetter, 1986). This would impact the storm tracks and associated heat and moisture transport to EA (Kleman et al., 2013; Roe and Lindzen, 2001; Liakka, 2011). Manabe and Broccoli (1985) suggests this could be the main driver of cold North Atlantic air, inducing thick and widespread sea ice cover over the North Atlantic.

The third main impact of ice sheets on the rest of the climate system is via changes to the distribution of freshwater fluxes into the ocean. This occurs directly via ice sheet melt and calving. Additionally, it occurs indirectly with changes in regional drainage routing from ice damming of rivers and proglacial lakes as well as topographic changes (*e.g.* Tarasov and Peltier, 2006) due to glacial isostatic adjustment (GIA). The induced changes in regional ocean salinity can then alter the rate of sea

ice production and extent as well as deep ocean convection (and associated formation of North Atlantic Deep Water, Labrador Sea intermediate water, and Antarctic Bottom water) and thereby the Atlantic meridional overturning circulation (AMOC) (Hu et al., 2008). Tests of the climatic impact of ice sheet induced changes in freshwater flux into the ocean have been a mainstay of recent paleoclimate modelling intercomparisons (Braconnot et al., 2007b; Kageyama et al., 2013b). However, the fluxes are often injected uniformly across a specified North Atlantic sector that ignores how liquid fluxes from the continents are actually likely to be transported (Condron and Winsor, 2012). It was shown in Bahadory and Tarasov (2018) that inclusion of dynamic runoff in fully coupled ice and climate modelling of the last glacial inception results in larger northern hemisphere ice sheets, more extensive ice cover in southern and western NA, and thinner ice in northern Alaska.

The last direct impact of ice sheets and associated topographic evolution on the rest of the climate system is via changing sea level, especially the associated opening and closing of ocean gateways. Previous modelling studies have shown reduced Bering Strait throughflow boosts deep convection in the North Atlantic Ocean, therefore strengthening the meridional overturning circulation and northward heat transport, which consequently promotes melting of ice sheets in North America and Europe (Shaffer and Bendtsen, 1994; Hu et al., 2010, 2012, 2015).

The above impacts of ice on climate are in turn subject to various further feedbacks within the (non-ice sheet) climate system. For instance, sea ice extent is sensitive to the Atlantic Meridional Overturning Circulation (AMOC) and the location of the polar front. Brine rejection from sea ice production in turn is a major driver of deep ocean convection which in turn is a major control on AMOC strength. Sea ice

presence/absence more generally strongly impacts heat, moisture, and momentum fluxes between the atmosphere and ocean. Changing sea ice extent also amplifies the meridional temperature gradient between low and high northern latitudes which in turn can affect the transport of both heat and moisture to higher latitudes (Vettoretti et al., 2000).

The changing state of the climate system in turn acts on ice sheets via 3 main drivers. First, changes in near surface air temperature affect surface mass balance as well as the rheology of ice. The effective viscosity of ice can change by 2 orders of magnitude over the relevant range of temperatures within present-day ice sheets. Warm summer temperatures can also induce meltwater ponding on ice shelves. This in turn can trigger ice calving from crack propagation due to hydrostatic pressure.

The second climate driver of ice sheets is changing precipitation which is the other key control on surface mass balance of ice. It also indirectly acts on ice sheet thermodynamics given that surface accumulation rates largely control the rate of vertical cold advection through the ice sheet.

Finally, ocean temperatures and circulation control submarine melt which can dominate ice shelf mass loss, as is currently the case for Antarctica (Rignot et al., 2013; Khazendar et al., 2016).

LCice 1.0 resolves each of these drivers and therefore the complete feedback loops. The model dynamically resolves the synoptic scale features of atmospheric circulation and includes most of the major feedbacks between the ice sheet and the rest of the climate system. In detail it includes: topographically self-consistent dynamic meltwater runoff routing, sub-shelf melt driven by modelled ocean temperatures, dynamic adjustment of Bering Strait throughflow, accounting for orographic forcing of

precipitation on the much higher resolution ice sheet grid and a dynamic vertical temperature lapse-rate. This is a major improvement compared to older coupled ice sheet - climate models, which were either one-way coupled, or only included some of these feedbacks.

In this paper, I use LCice 1.0 to examine the sensitivity of the Northern Hemisphere ice and climate system to feedbacks from ice sheet evolution. This examination is via a set of sensitivity experiments that isolate individual ice on climate drivers detailed above. The choice to restrict attention to the role of the Northern Hemisphere ice sheets is in large part due to computational, model development, and project size constraints. A further justification is that glacial inception sea level rise has been inferred to be mostly sourced in the Northern Hemisphere (Gallup et al., 2002; Huybrechts, 2002).

4.2 Model description

LCice 1.0 incorporates full two-way (asynchronous) coupling of LOVECLIM v1.3 and version D2018.may18 of the GSM. A brief description of each of the components are provided below. For more details about the LOVECLIM and LCice 1.0 coupler, refer to Goosse et al. (2010b) and Bahadory and Tarasov (2018) respectively.

4.2.1 LOVECLIM

LOVECLIM consists of stochastic-dynamic 3 level atmospheric (ECBilt), primitive equation ocean (CLIO) and dynamic vegetation (VECODE) modules. It is fast enough to simulate the last glacial inception (120 ka to 100 ka) in less than 3 weeks

using a single computer core. Therefore, it has been used to simulate a wide range of different climates from the last glacial maximum (Roche et al., 2007) through the Holocene (Renssen et al., 2009) and the last millennium (Goosse et al., 2005) to the future (Goosse et al., 2007).

4.2.2 GSM

The core of the GSM is a thermo-mechanically coupled ice sheet model. It includes a 4 km deep permafrost-resolving bed thermal model (Tarasov and Peltier, 2007), fast surface drainage and lake solver (Tarasov and Peltier, 2006), visco-elastic bedrock deformation (Tarasov and Peltier, 1997a), Positive Degree Day surface mass balance with temperature dependent degree-day coefficients derived from energy balance modelling results (Tarasov and Peltier, 2002), sub-grid ice flow and surface mass balance for grid cells with incomplete ice cover (Le Morzadec et al., 2015), and various ice calving schemes for both marine and pro-glacial lake contexts. For the results herein, ice shelves are treated using a crude shallow ice approximation with fast sliding. The GSM is run at 0.5°longitude by 0.25°latitude grid resolution, with separate grids for NA and EA.

4.2.3 Coupler

The LCice 1.0 coupler permits an adjustable coupling time-step (20 year herein). LOVECLIM limitations restrict land-mask changes to relative sea level controlled changes in Bering Strait throughflow. This fixed land-ocean mask of the LOVECLIM does not prevent ice from growing over the continental shelves, as the GSM considers

the relative sea level variations in the coupled regions when simulating the ice volume, determining ice shelf location, and computing subshelf melt.

4.3 Experimental design

Three sets of experiments examine the following:

- The impact of ice sheet topography and albedo on the ice/climate system
- The impact of ice sheet induced sea level changes on the Bering Strait throughflow, and hence the rest of the ice/climate system
- The impact of ice sheet induced changes to surface runoff on the ocean circulation, and hence the rest of the ice/climate system

To partly address parametric uncertainty of the model, each sensitivity experiment consists of an 11 run ensemble, for which LCice 1.0 parameters were chosen from an earlier ensemble of 55 simulations (*cf.* Chap. 3). Each sensitivity experiment is detailed below.

4.3.1 Fixed NA and EA ice sheets

To largely isolate the orographic and radiative impacts of each ice sheet on the climate and hence the evolution of the other ice sheet, from other factors such as albedo and surface fluxes (momentum, moisture, sensible heat), I set up two groups of ensemble simulations. In one group, I completely removed one of the ice sheets (*noNA* and *noEA*) from the LCice coupling. In the other group, I removed the orographic effect of each ice sheet by setting ice thickness to 1 m (*flatNA* and *flatEA*) in the coupler. To

maintain other feedbacks (such as hemispheric sea level change coupling between ice sheets), both ice sheets were still modelled in the GSM. I do not have ensembles for removal of the radiative effect alone (black ice) as seasonal snow cover will still largely retain the albedo impact. Two additional ensembles have one of the NA and EA ice sheets fixed at their maximum volume and extent during the inception period (*maxNA* and *maxEA*) in the coupler (but again the GSM evolved both ice sheets dynamically). In all the fixed NA experiments, Bering Strait throughflow in LOVECLIM was only a function of EA ice volume. Table 4.1 summarizes the ensembles with fixed ice sheets simulations.

4.3.2 Fixed Bering Strait

Two ensembles with the Bering Strait kept closed (*BS0*) and opened (*BS1*) during the whole simulation isolate the impact of changing Bering Strait throughflow. The results for this experiment are discussed in section 4.4.4.

4.3.3 Fixed meltwater runoff

I incorporate three ensembles with fixed meltwater runoff: runoff flux fixed at its present day value extracted from LOVECLIM simulation climatologies with PD (present-day) boundary conditions for each month (*fluxPD*), with imposed zero runoff from the NA and EA GSM grid regions (*flux0*), and with the runoff routing fixed at its present day configuration (routPD). In the *flux0* and *fluxPD* experiments, the runoff is only held constant in the regions covered by the GSM grid. Table 4.3 summarizes the runoff sensitivity experiments with results discussed in section 4.4.3.

Table 4.1: List of the ensembles with fixed NA and EA ice sheets

Ensemble ID	**Topography**	**Albedo**	**Description**
noNA	no	no	The NA ice sheet in the GSM has no impact on LOVECLIM
flatNA	no	YES	Only the NA ice mask is passed to LOVECLIM
maxNA	YES	YES	The NA ice sheet topography and ice mask input to LOVECLIM are fixed to the maximum value during the inception simulation
all above			NA has no impact on Bering Strait throughflow
noEA	no	no	The EA ice sheet in the GSM has no impact on LOVECLIM
flatEA	no	YES	Only the EA ice mask is passed to LOVECLIM
maxEA	YES	YES	EA ice sheet topography and ice mask input to LOVECLIM are fixed to the maximum value from the *ctrl* simulation
ctrl	YES	YES	Complete GSM-LOVECLIM coupling: LOVECLIM receives the dynamical topography, sea level contribution, and albedo of both ice sheets

Table 4.2: List of the ensembles with Bering Strait open and close

Ensemble ID	**Bering Strait Flow**	**Description**
BS0	no	No flow through the Bering Strait at all times
BS1	YES	Bering Strait depth is kept at its PD level
ctrl	Varies	Bering Strait flow is affected by relative sea level change and ice sheet coverage

Table 4.3: List of the ensembles with meltwater runoff flux fixed

Ensemble ID	**Runoff**	**Description**
flux0	zero	no runoff into ocean from the regions covered by the NA and EA GSM grids
fluxPD	fixed flux	the NA and EA runoff fluxes are fixed at their PD values
routPD	fixed routing	the NA and EA runoff routings are fixed at their PD configurations
ctrl	varies	runoff flux and routing are calculated at runtime, and updated at every coupling time step

4.3.4 Parameter vectors

Ensemble parameter vectors components were previously selected to address major sources of uncertainty in LCice (Bahadory and Tarasov, 2018). They include parameters from: LOVECLIM (snow albedo, bare-ice albedo, melting ice albedo, precipitation threshold, cloud parameterization scheme), the GSM (basal drag, ice shelf flow, calving, and sub shelf melt), and the coupling (spin-up length and start time, upscaling method, vertical temperature gradient calculation method). Parameter values for each ensemble member are provided in supplemental table C.1.

4.3.5 Initial conditions

As the Eemian extent of the Greenland ice sheet is not well constrained, ensemble runs start with PD ice thickness and surface elevation. Ice and bed temperatures are spun up with contemporaneous surface temperatures to near thermal equilibration starting from an initial basal ice temperature of -10°C. LOVECLIM spinup for each ensemble run is under transient orbital and GHG forcing with fixed PD ice. Spinup interval is under ensemble parameter control and ranges 3 to 5 kyr.

4.4 Results and discussion

Below, I first examine the orographic and radiative impact of each ice sheet on the climate system and the other ice sheets. To minimize the local feedbacks from each ice sheet on its own evolution, I initially compare the four ensembles during the early stages of the inception, when the ice sheets are not large enough to significantly alter regional climate. I then compare ice evolution around the inception peak and

subsequent retreat phase after 110 ka. In subsequent sub-sections, I investigate the sensitivity of the ice sheets and the climate system to the change in the treatment of surface runoff flux and routing as well as the change in Bering Strait throughflow.

4.4.1 Fixed NA ice sheet

Considering first the ice sheet response, there is an apparent non-linearity with *ctrl* EA ice volume well below that of all other fixed NA experimental results (figure 4.1.right), including both *maxNA* and *flatNA*. This is due (in large part if not wholly) to the confounding changes in Bering Strait throughflow in *ctrl* compared to that of the other 3 experiments which lack NA ice sheet contributions to Bering Strait sea level change (consider *BS1* and *BS0*). Unlike all the fixed NA experiments, *ctrl* experiments all have Bering Strait closure starting approximately at the time the ice volume time series starts to diverge from that of the *flatNA* runs. A new fixed NA *ctrl* experiment will soon be completed that applies the same Bering Strait treatment.

The *noNA* and *flatNA* ensemble mean EA ice sheet volume histories slowly diverge over the simulation period with the *noNA* runs having somewhat larger EA ice sheets especially towards the subsequent interstadial ($\sim$8% mean difference at peak volume, $\sim$45% at 105 ka, solid red and blue lines in figure 4.1.right). The difference between the two experiments does not fully isolate the impact of ice sheet albedo and surface roughness as there is year round snow coverage over much of the NA region in the *noNA* ensemble, hence replicating the flat ice conditions. But the residual seasonal albedo difference (along with change in surface roughness) provides a result contrary to what one would expect based on a positive albedo feedback given that *noNA* has

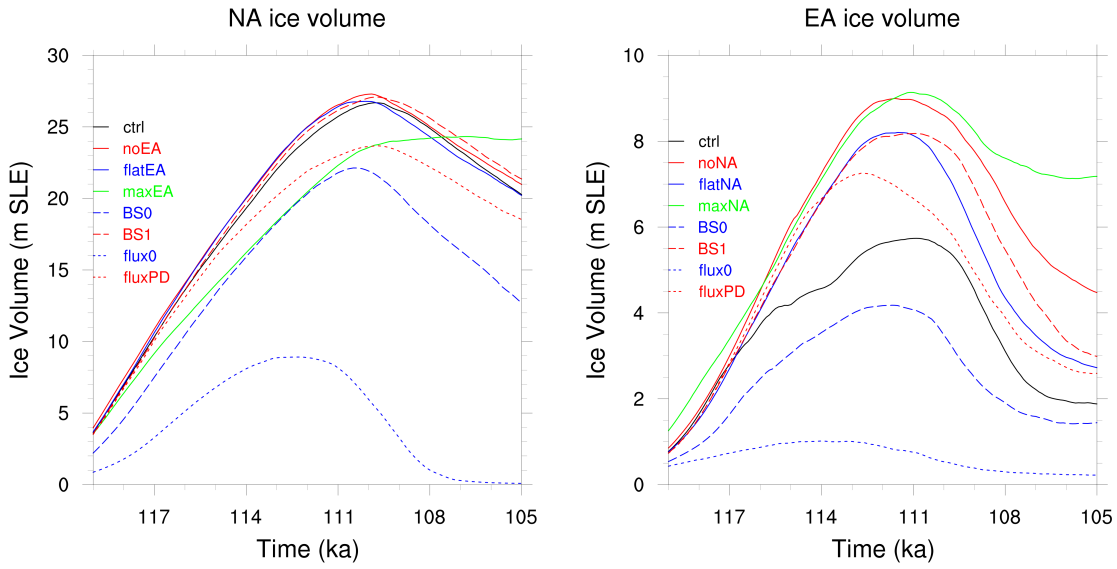

Figure 4.1: NA and EA ensemble mean ice volume in meters of sea level equivalent (m SLE) for all the sensitivity experiments.

more ice than *flatNA*.

The *maxNA* runs evolve more differently (solid green line in figure 4.1.right). The ensemble mean EA ice sheet under *maxNA* is larger than that of all other ensembles during all but the mid growth phase. *maxNA* most distinctly has a much weaker post stadial retreat. This response is at odds with the results of Beghin et al. (2015), for which a higher NA ice sheet resulted in smaller EA ice, such that with full LGM size NA ice, EA ice cover was restricted to Svalbard. The difference between *maxNA* and *flatNA* encapsulates the maximum impact of ice sheet orography with confounding influence from albedo from changing ice extent.

The relative ice volume chronologies hide larger differences in regional ice thickness between the four ensembles. *maxNA* has the thickest and most extensive high latitude ice (from Svalbard to Spitzbergen), while *flatNA* and *noNA* have the thickest ice over

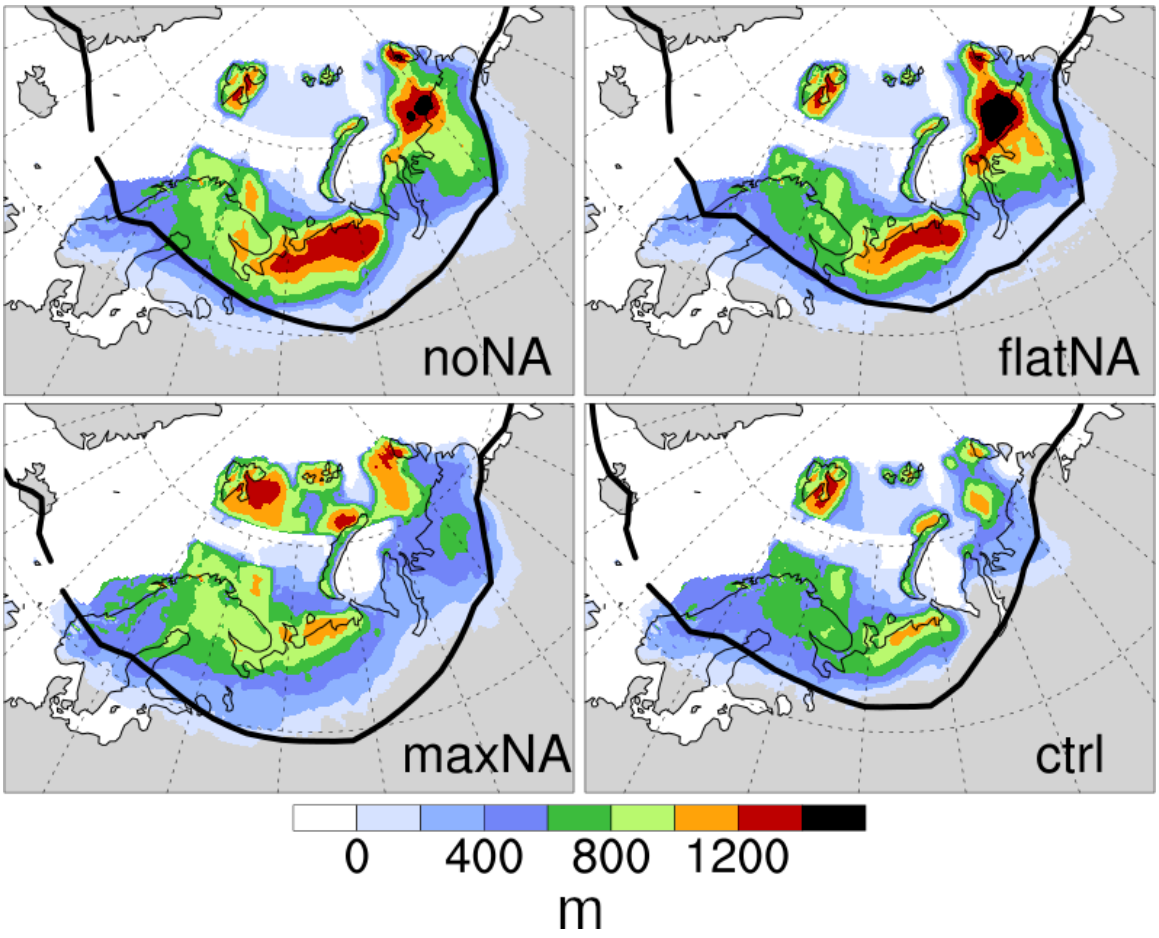

Figure 4.2: The ensemble means of the EA ice sheet thickness (filled colors) and summer (JJA) mean 2m 0°C isotherm (solid black line) at 110 ka for the four experiments.

continental northern Russia (figure 4.2). *ctrl* has the thinnest ice in most regions. This is likely due to Bering Strait closure in the control run, which reduces Arctic Ocean outflow through Fram Strait, which in turn strengthens AMOC and thereby increases heat transport to higher latitudes of EA. It should be noted that the straight marine ice boundaries in figure 4.2 are a spurious result of the rectangular downstream ocean sectors within which the identical upstream dynamic vertical ocean temperature profile is assigned for computing submarine ice melt in the GSM.

To more clearly discern how the ensembles deviate from each other over time I divide the EA region into three sectors (characterized by transect lines A, B, and C in figure 4.5). To minimize the influence of the EA ice sheet feedback on the climate, I first focus on the early stages of the inception.

4.4.1.1 Early inception

Two features stand out when comparing the 119 ka *maxNA* ensemble mean ice field against that of *ctrl* and the other two fixed NA experiments (figure 4.3). First, the 119 ka *maxNA* ensemble mean has much more southern extent of continental ice even though the mean JJA 0°C isotherm is hardly displaced relative to that of the other three experiments. Latitudinal 119 ka transects for LOVECLIM mean JJA 2 m air temperature and annual precipitation (without orographic corrections) also do not clearly explain the difference. I suspect the likely source are orographic forcing corrections on the GSM grid to precipitation [and will expand this analysis during the PhD defense presentation with GSM precipitation fields].

The second distinguishing feature is the more extensive marine ice north of 75°N in *maxNA* that is all but absent in the other three experiments. Given the continental location of the JJA 0°C isotherm in figure 4.3 as well as similarity in latitudinal temperature transects (figure 4.5), this difference in high latitude marine ice extent can only be due to colder Barents and Kara Seas in *maxNA*. This correlates with larger northern hemisphere (NH) sea ice extent (green contours in figure 4.4), which potentially could limit ocean heat transport to this region.

The larger sea ice area however does not reduce the annual precipitation in the Barents-Kara seas (BK) at the early stages of the inception (figure 4.5). Instead, a

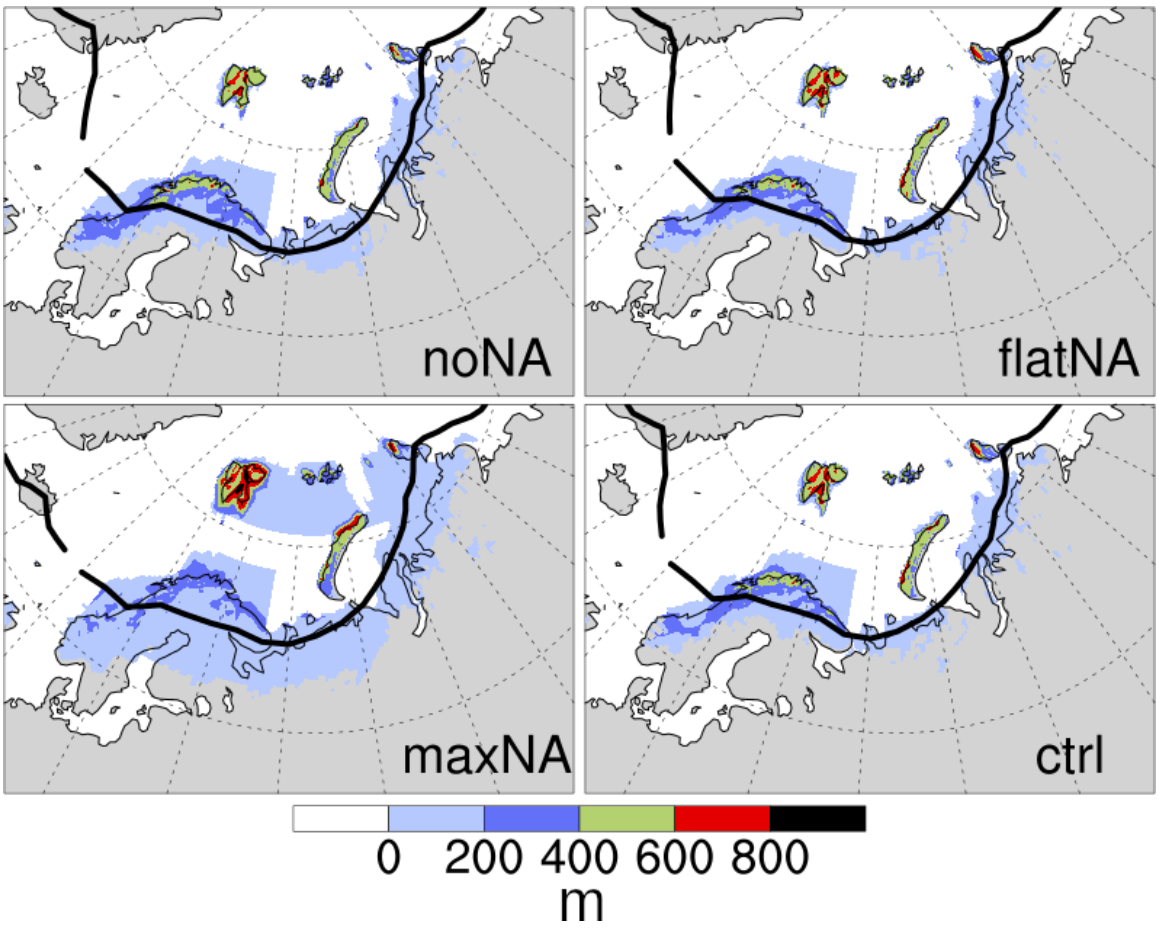

Figure 4.3: The ensemble means of the EA ice sheet thickness (filled colors) and summer (JJA) mean 2m 0°C isotherm (solid black line) at 110 ka for the four experiments.

stronger Iceland low in the *maxNA* ensemble compared to that of *noNA* and *flatNA* enhances moisture transport from sea ice free region of the North Atlantic (figure 4.4). This enables faster early inception ice growth over Svalbard (figure 4.3 and 4.5).

4.4.1.2 Inception stadial and later

At around inception peak, in all three longitudes the coldest ensemble has the most extensive ice sheet (*maxNA* in the western and central EA, and *flatNA* in the eastern EA) (figure 4.6). The relationship between regional ice thickness and temperature or precipitation is not as clear for the ensembles. In the western EA, all simulations have a relatively similar ice thickness over Svalbard, while below 74°N, *noNA* is the thickest one, followed by *maxNA* and *flatNA*. In the central and eastern EA, *maxNA* is the third thickest in low- and mid-latitudes, although still the most extensive one, while *noNA* and *flatNA* are the first and second thickest, respectively. This indicates a tendency for increased ice accumulation over western EA in the presence of a larger NA ice sheet.

BK and high latitudes of eastern EA (the 100°E transect in figure 4.6) are the only regions where *maxNA* has the thickest ice in higher latitudes. The difference in BK is significant (over 8 times thicker than other ensembles), similar to the large difference between *maxNA* and others at 119 ka (figure 4.5). As the temperature in all ensembles are below zero in this region, and *maxNA* has the lowest precipitation, analysis of the downscaled temperature and precipitation in this region is required.

In all latitudes and transects, the *ctrl* ensemble has the smallest ice sheet, except over Svalbard, where its ice thickness is similar to the other.

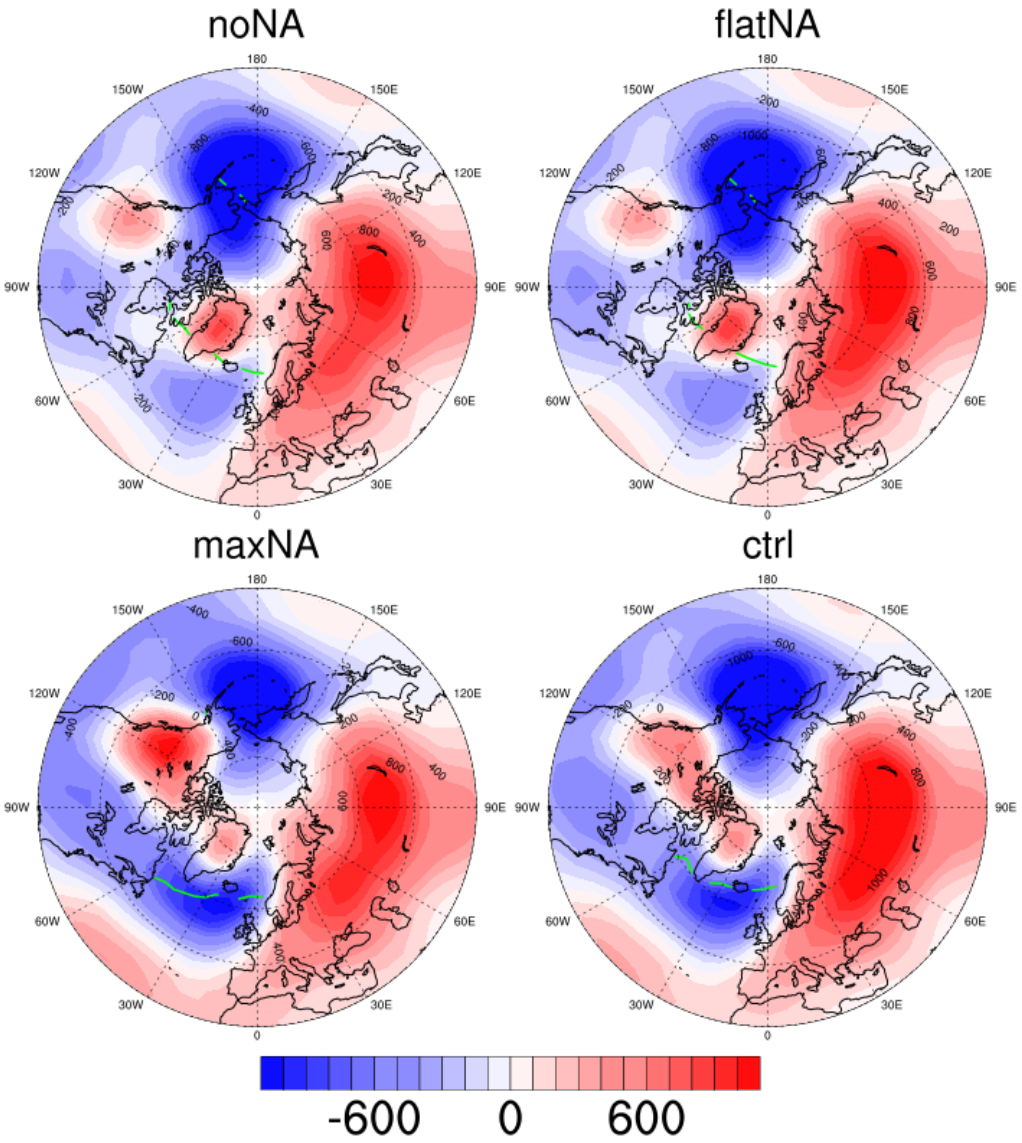

Figure 4.4: The 800 hPa winter geopotential zonal anomaly in the four ensembles at 119 ka. The green lines show the extent of sea ice in summer.

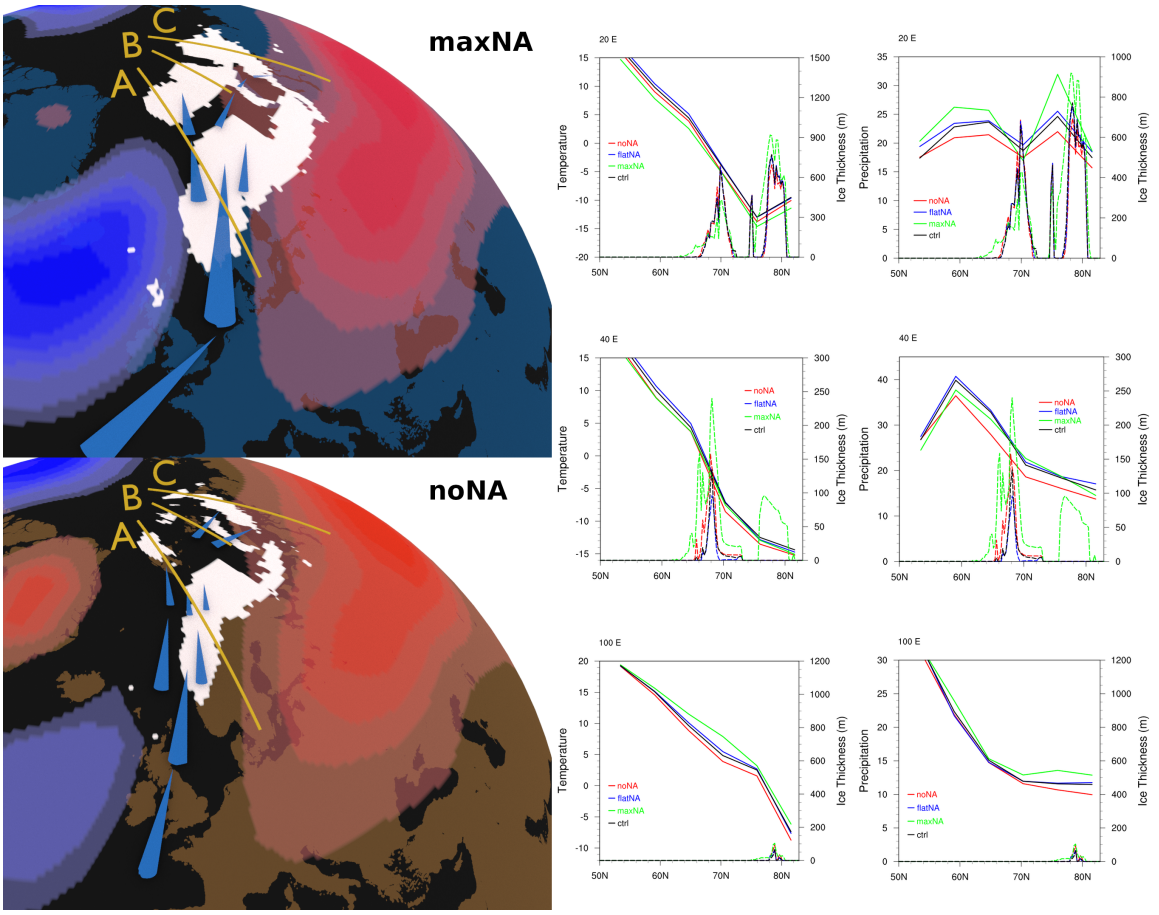

Figure 4.5: The EA ice sheet (white areas) and 800 hPa geopotential zonal anomaly (blue and red regions) at 119 ka in the *maxNA* ensemble (top-left) and noNA ensemble (bottom-left). The blue arrows and their thickness show the direction and strength of moisture transport to EA. The blue and orange colors of the continents in the *maxNA* and *noNA* map plots represent the background cooling caused by the presence/absence of the NA ice sheet. The three left plots show the ice thickness, mean summer (JJA) air temperature, and yearly mean precipitation profiles (from LOVECLIM and therefore without orographic corrections on the GSM grid) for the four ensembles at **A** 20°E longitude, **B** 40°E longitude, and **C** 100°E longitude.

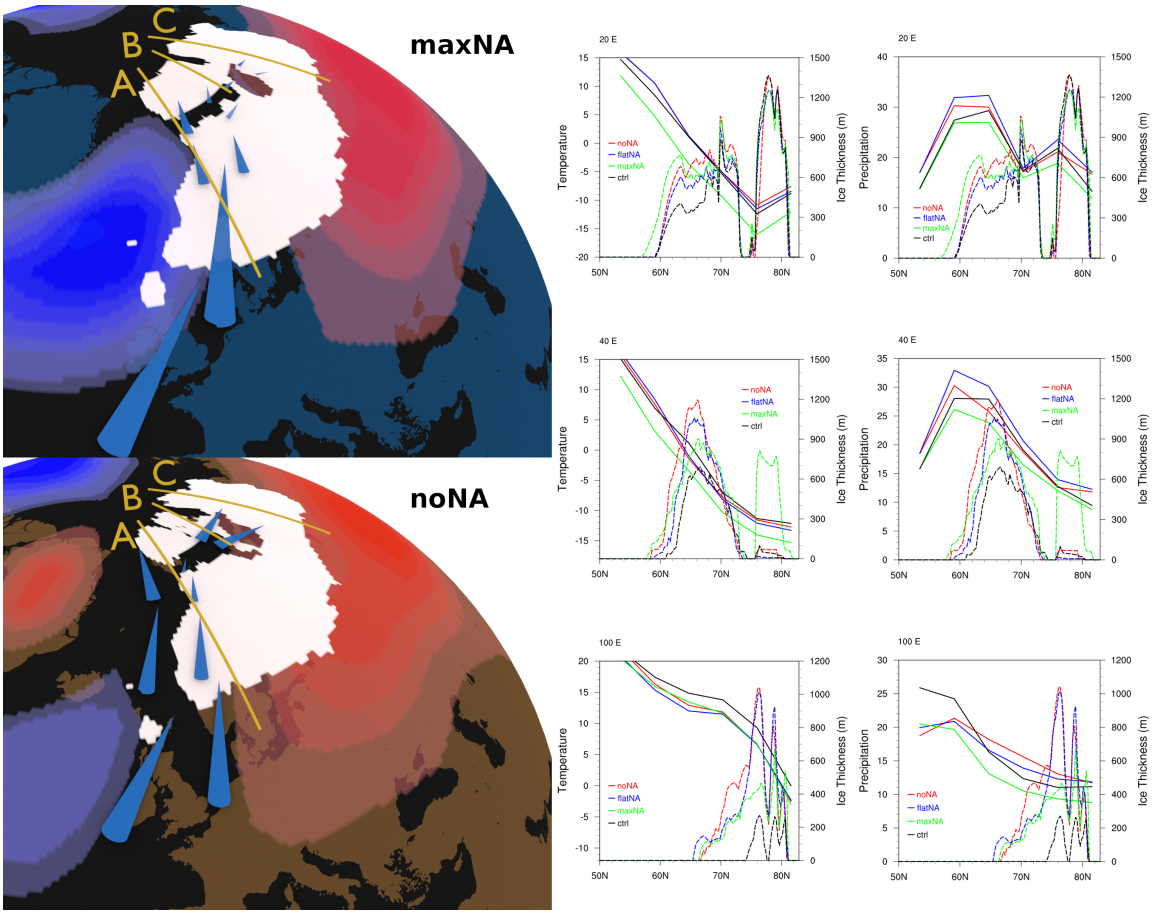

Figure 4.6: The EA ice distribution (white areas) and 800 hPa geopotential zonal anomaly (blue and red regions) at 112 ka (around the peak) in the *maxNA* ensemble (top-left) and *noNA* ensemble (bottom-left). The blue arrows and their thickness show the direction and strength of moisture transport to EA. The blue and orange colors of the continents in the *maxNA* and *noNA* map plots represent the background cooling caused by the presence/absence of the NA ice sheet. The three left plots show the ice thickness, mean summer (JJA) air temperature, and yearly mean precipitation profiles (from LOVECLIM and therefore without orographic corrections on the GSM grid) for the four ensembles at **A** 20°longitude, **B** 40°E longitude, and **C** 100°E longitude.

4.4.1.3 Atlantic meridional overturning circulation

In these four ensembles, the strength of the AMOC during the growth phase of the inception is strongly affected by the initial configuration of the NA ice sheet (figure 4.7). The *maxNA* ensemble starts with a stronger AMOC than the other three ensembles. The *ctrl* run starts with an AMOC relatively close to the *noNA* and *flatNA* ensembles, and as ice sheets build up over NA and EA, the AMOC strength quickly grows to values close to that of the *maxNA* ensemble. Both *flatNA* and *noNA* only have a small (< 2 Sv) increase in AMOC which terminates prior to 114 ka.

Due to the absence of a dynamical NA ice sheet in *noNA*, *flatNA*, and *maxNA*, the meltwater runoff into the ocean only varies with changes in the EA ice sheet volume in these three experiments. These three experiments also have similar treatments for Bering Strait depth changes (only driven by changes in EA ice volume). Therefore the much stronger AMOC in *maxNA* compared to that of *noNA* and *flatNA* must be entirely due to changes in wind stress on the ocean induced by the different NA topography.

The large growth and subsequent decay in the *ctrl* AMOC and timing thereof is likely due to the combination of all major ice on climate feedbacks. Prior to 116 ka, Bering Strait in the *ctrl* is largely open, and changes in NA orographic forcing of atmospheric circulation with growing NA ice along with changing runoff must play the critical role. At approximately 116 ka, Bering Strait loses throughflow in *ctrl*, and remains closed until approximate 110.5 ka and thus well after the large decay in *ctrl* AMOC that ends about 113 ka. To isolate the effect of Bering Strait transport and terrestrial runoff, I have set up two more experiments, to examine the impact of

runoff (section 4.4.3), and the impact of Bering Strait throughflow (section 4.4.4).

4.4.2 Fixed EA ice sheet

Except for *maxEA*, the EA ice sheet has a much smaller impact on NA ice sheet evolution (solid lines in figure 4.1.left). NA ice growth is similar in the *ctrl*, *flatEA*, and *noEA* experiments. *maxEA* starts with more gradual growth due to warmer JJA temperature (at least for the transect in figure 4.8) and unlike the other three, it has continuous though weaker growth after 112 ka. This growth is abetted by slightly increased precipitation (figure 4.8) and about a 2°C colder regional JJA temperature at its more northerly located southern ice margin compared to that of the other three experiments in the indicated transect.

4.4.3 Meltwater runoff

To isolate the sensitivity of the NA and EA ice sheets to changes in the meltwater runoff flux, I performed three ensemble simulations: 1. meltwater flux fixed at its present day (*fluxPD*) value, *i.e.* , the rate of runoff to the ocean does not change with ice volume change, 2. no meltwater at all (*flux0*), and 3. the *ctrl* run, in which the meltwater flux and routing is determined by the change in ice volume and surface topography at each coupling step (details in Bahadory and Tarasov, 2018, supplement). In a separate ensemble simulation, I fixed the runoff routing to its present day conditions, and allowed the coupler to determine the runoff flux dynamically through the simulation. However, perhaps due to limited drainage sites into the ocean in LOVECLIM and the coarse resolution of these drainage sites (*cf.*

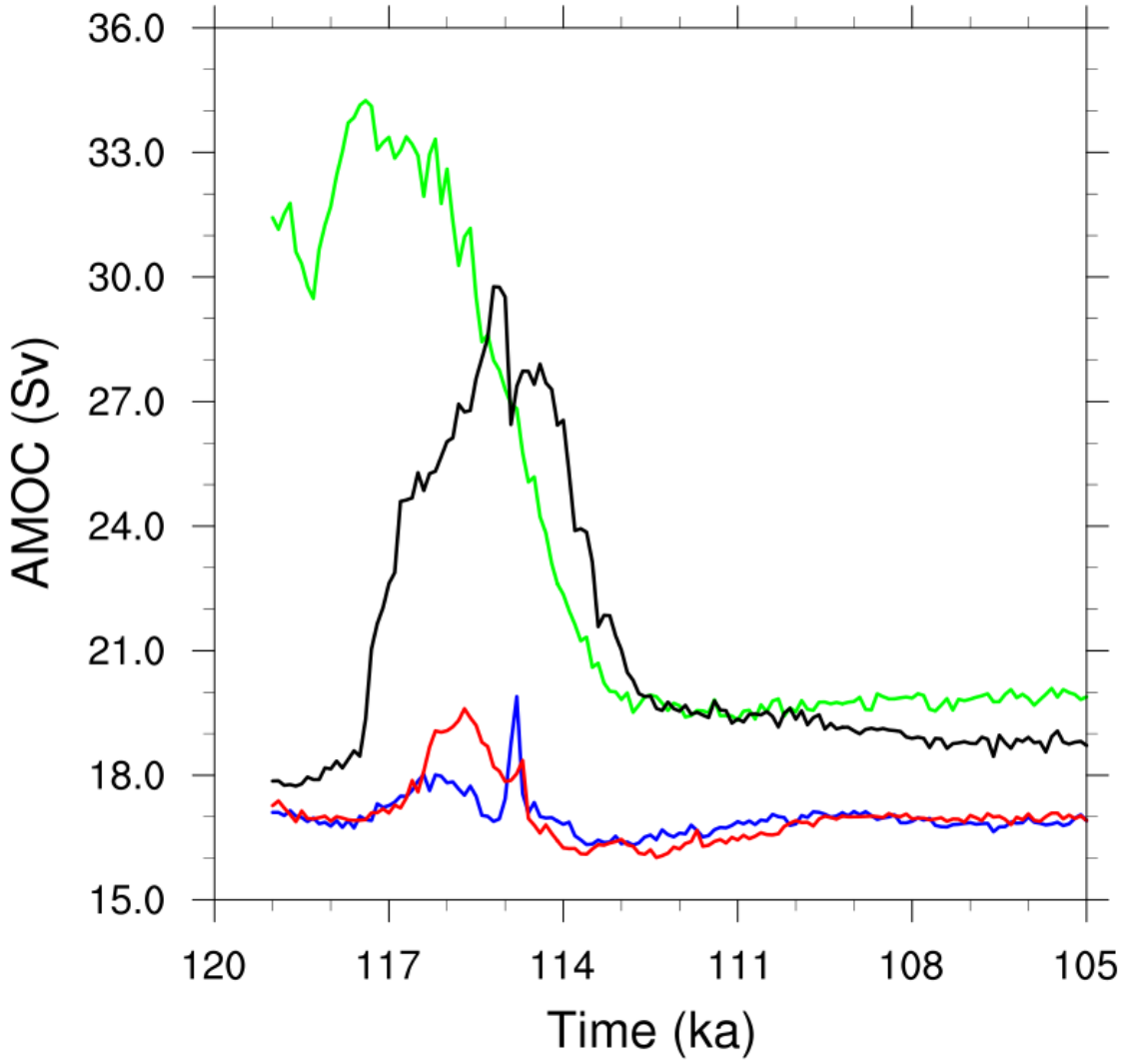

Figure 4.7: Maximum AMOC strength in the North Atlantic for *noNA* (red), *flatNA* (blue), *maxNA* (green), and *ctrl* (black) during the last glacial inception.

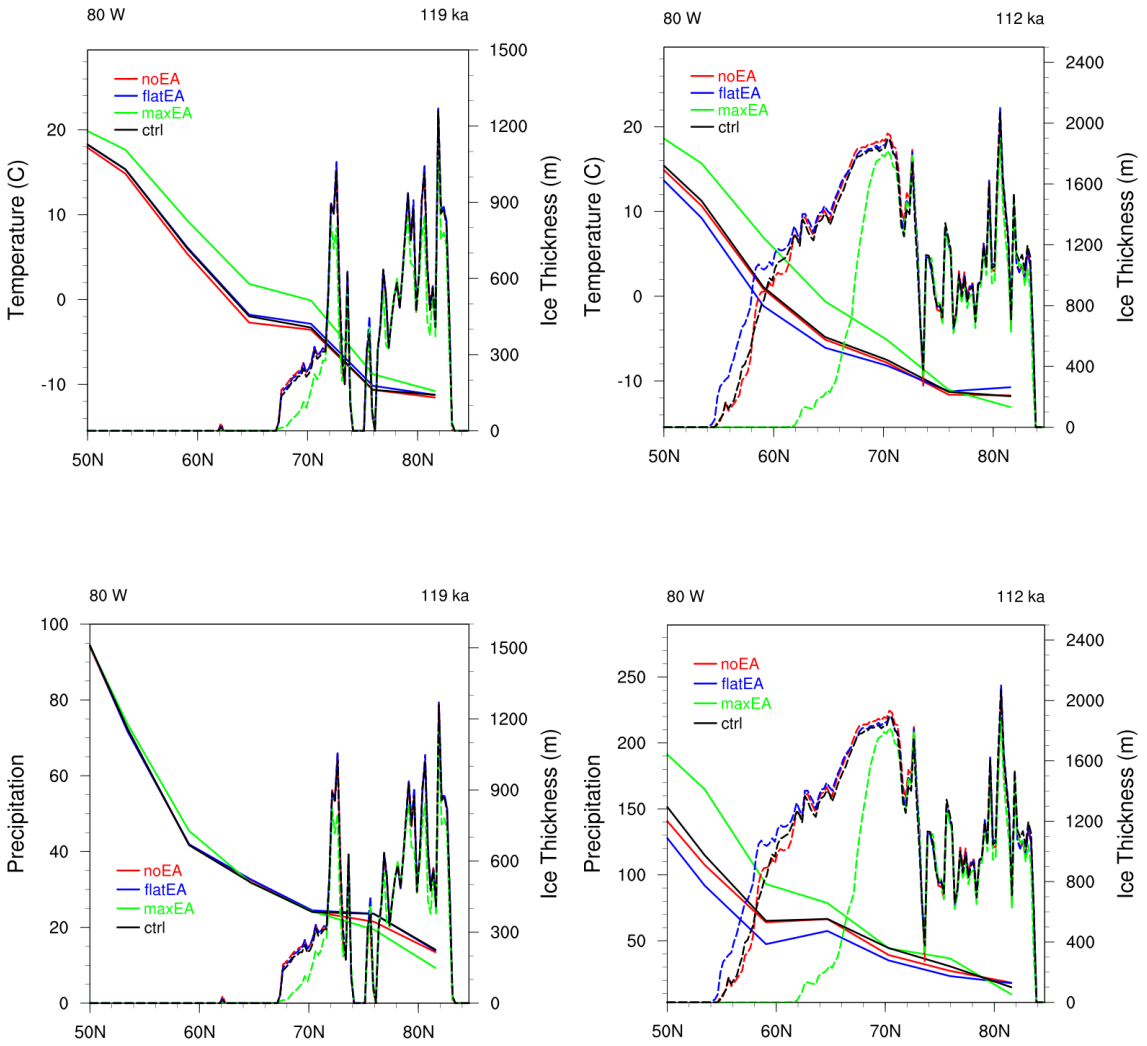

Figure 4.8: Ice thickness, temperature (first row), and precipitation (second row) profiles along the 80°W in NA at 119 ka (left column), and 112 ka (right column) for fixed EA ice sheet experiments (*noEA* red, *flatEA* blue, *maxEA* green, and *ctrl* black). Dashed lines show the ice thickness, and solid lines temperature or precipitation.

supplement of Bahadory and Tarasov, 2018), no significant changes occur in the evolution of the ice and climate compared to the *ctrl* experiments with dynamic routing (not shown). Therefore, I focus on the forced flux experiments in the rest of this section.

The *flux0* experiment, though unphysical, offers a reference bound for the role of surface runoff on climate. It produces the smallest NA and EA ice sheets of any experiment herein (figure 4.1). This is due to higher surface temperatures for all given EA and NA transects (supplemental figure C.4, C.5, and C.7) reaching beyond 10°C for the two most western EA transects. These higher temperatures are in turn due to a much stronger AMOC (almost a factor three of the *fluxPD* value, figure 4.10) resulting from the reduced freshwater fluxes into the ocean.

The enhanced freshwater fluxes into the ocean of the *fluxPD* experiment results in a weaker AMOC than that of *ctrl* for the 118.5 ka to 110 ka interval (figure 4.10). This in turn results in western EA cooling (figure 4.9) and more EA ice for *fluxPD*, especially during the interval when *ctrl* is growing (figure 4.1) and therefore subject to reduced net freshwater flux to the ocean. The *fluxPD* ensemble mean also has a LGI peak ice volume occurring more than 2 kyr in advance of *ctrl*, and thereby 2 kyr closer to the time of minimum 60°N JJA insolation at 114.5 ka. Thus the reduced rate of ice growth from change in freshwater fluxes appears to explain much of the phase delay between orbital forcing and maximum EA ice volume.

The NA response to *fluxPD* is opposite to that of EA, with an approximate 15% reduction in peak LGI ice volume (figure 4.1) compared to *ctrl*. At least for the 80°W transect in supplemental figure C.7, this is due to slightly warmer temperatures apparently only partially offset by enhanced precipitation. The smaller *fluxPD* LGI

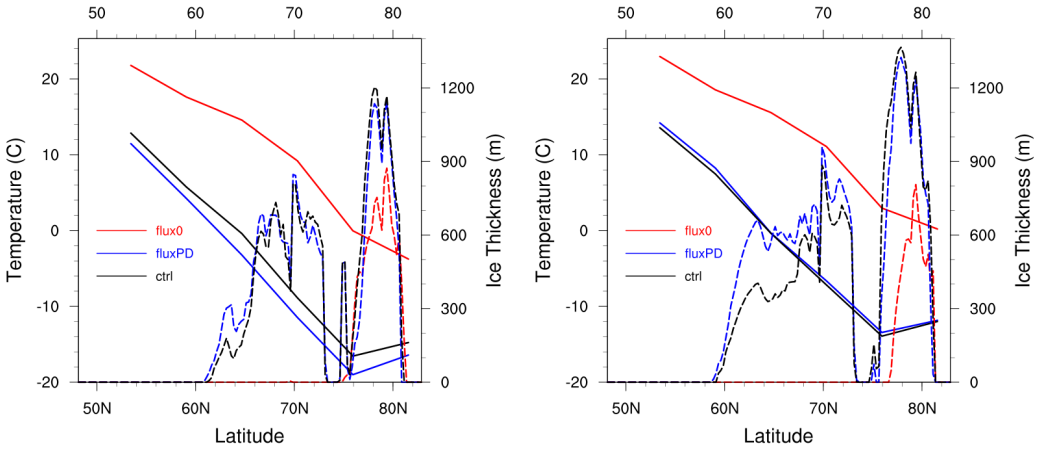

Figure 4.9: Ice thickness (dashed lines) and mean summer (JJA) temperature (solid lines) profiles at 20°E for *flux0* (red), *fluxPD* (blue), and *ctrl* (black) ensembles at **a**. 116 ka, and **b**. 112 ka.

peak has a sub kyr phase delay compared to *ctrl*, again mirroring the peak volume and phasing relationship for EA. I speculate that the enhanced NA warming of *fluxPD* is due to atmospheric compensation for the reduced oceanic heat transport to the higher latitudes not being masked by the regional downstream cooling over EA.

4.4.3.1 Sea ice

The regional shutdown of runoff in the *flux0* ensemble results, as expected, in significantly smaller NH sea ice area (about one third less) compared to the other two experiments, largely due to enhanced northward heat transport by a stronger AMOC (figure 4.12).

Comparison of *fluxPD* and *ctrl* mean sea ice area elucidates the interplay of hemispheric cooling from orbital forcing and changes in AMOC. Under the much smaller

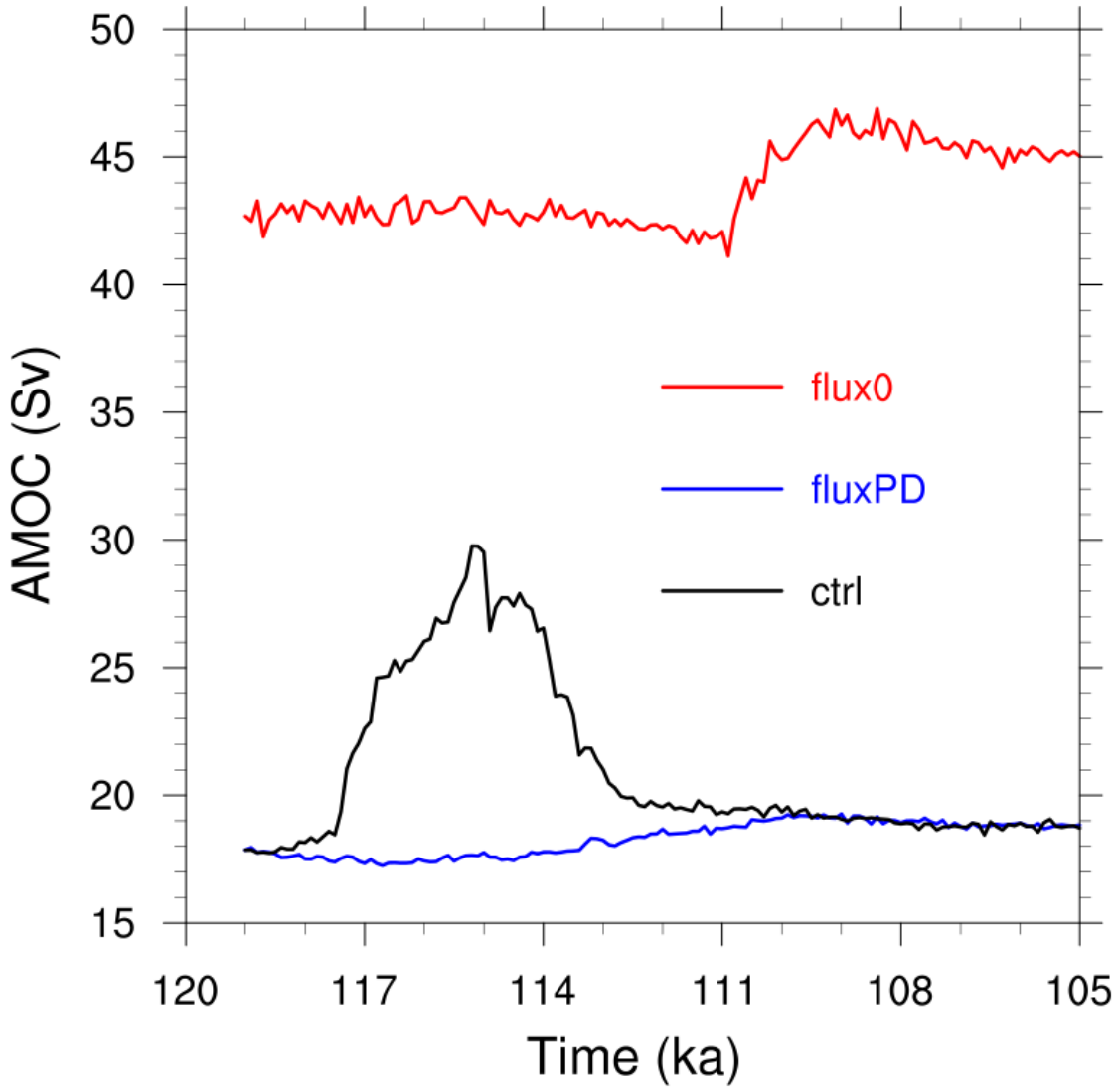

Figure 4.10: Maximum of the meridional overturning in the North Atlantic for *flux0* (red), *fluxPD* (blue), and *ctrl* (black) ensembles.

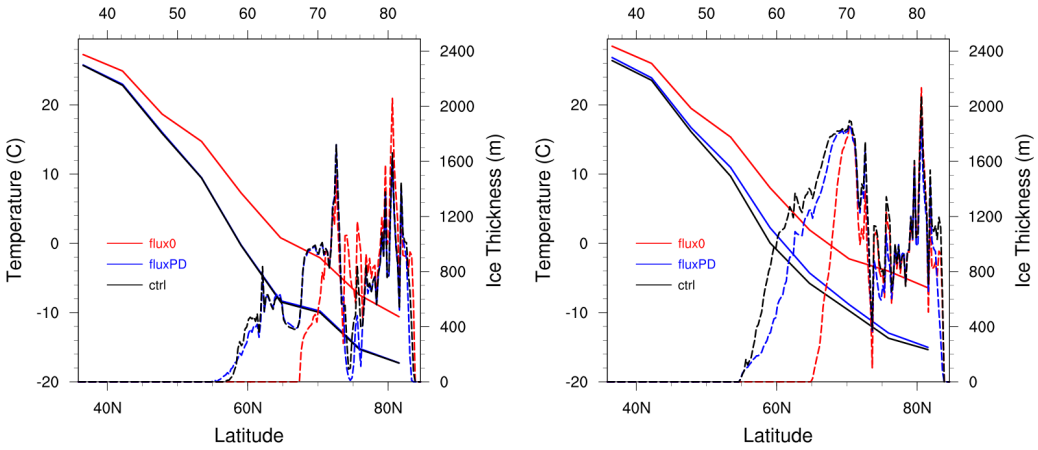

Figure 4.11: NA ice thickness (dashed lines) and temperature (solid lines) profiles at 20°E for *flux0* (red), *fluxPD* (blue), and *ctrl* (black) ensembles at **a**. 115 ka, and **b**. 112 ka.

changes in AMOC in *fluxPD*, NH sea ice area grows until approximately 113 ka or about 1.5 kyr after the time of the orbital 60°N JJA insolation minimum, and then undergoes a nearly constant rate of decrease to at least 105 ka. Given that *fluxPD* AMOC is decreasing (albeit slowly) after 110 ka, most of this post peak decrease must be largely in response to orbital forcing. *ctrl* undergoes a relative reduction of NH sea ice area (compared to *fluxPD*) during its interval of increasing AMOC from approximately 118 ka to 115.5 ka. The ensuing reduction in AMOC brings increasing sea ice area converging to that of *fluxPD* when corresponding AMOC strengths converge.

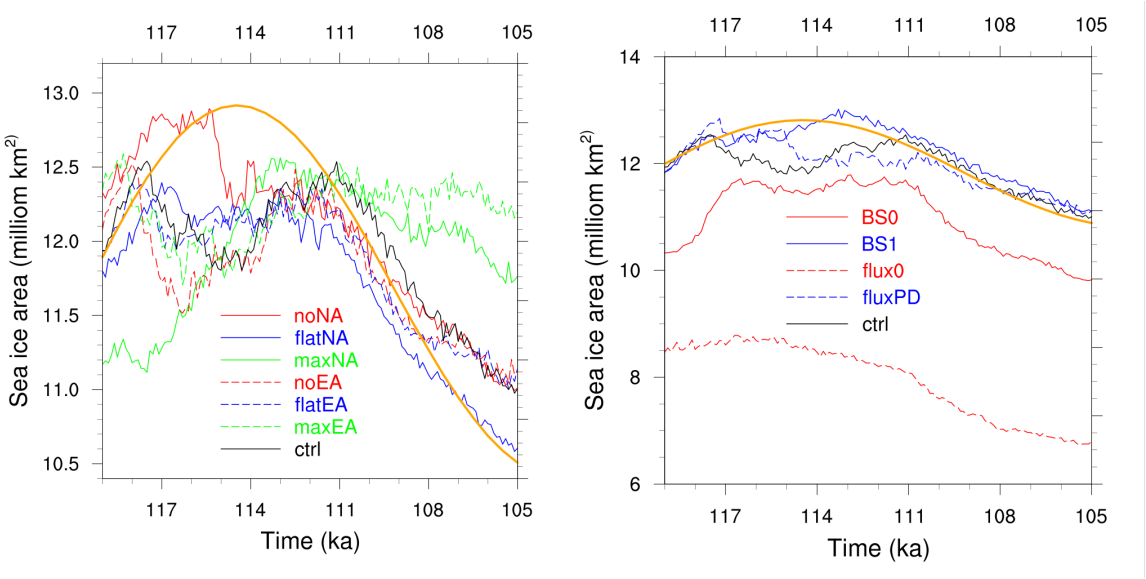

Figure 4.12: The ensemble mean annual NH sea ice area for all ensembles. **Left**: fixed-NA and fixed-EA ensembles. **Right**: fixed-BS and fixed-runoff ensembles. The orange line in both plots represents scaled 60°N mean JJA insolation.

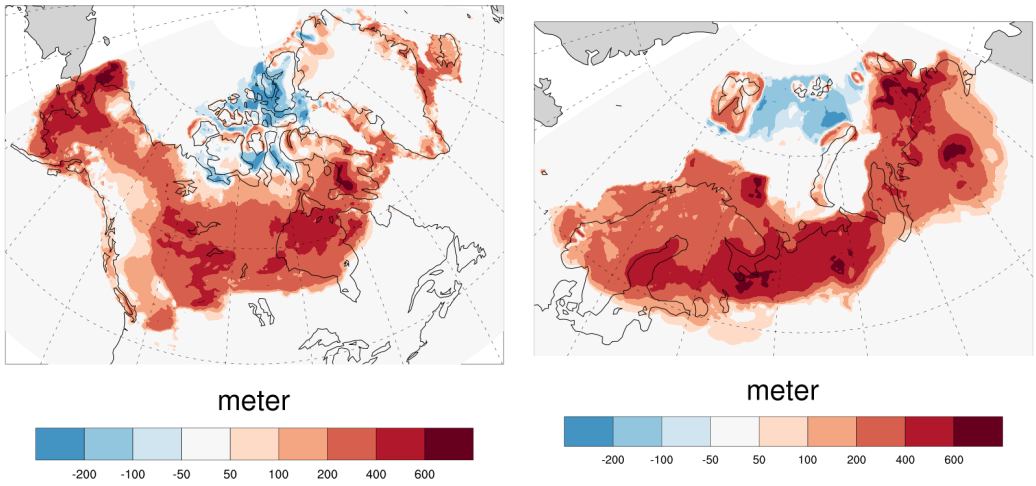

Figure 4.13: The NA and EA ice thickness difference between *BS1* and *BS0* at 112 ka.

4.4.4 Bering Strait

Three ensembles of simulations isolate the impact of the Bering Strait throughflow on the climate system and growth and retreat of each ice sheet during the LGI: with the Bering Strait i) open (*BS1*) and ii) closed (*BS0*) through the whole LGI, and iii) the *ctrl* run, in which the Bering Strait flow is determined by the relative sea level with accounting for floating and grounded ice cover.

The EA ice volume is the largest in the *BS1* ensemble, and the smallest in the *BS0* ensemble, with the *ctrl* ensemble being between the two (dashed lines in figure 4.1.right). At around inception peak (112-111 ka), The EA ice volume in the *BS1* experiment is almost double the *BS0* volume. Consistent with the ice volume, *BS1* EA ice is thicker than that of *BS0* in almost all latitudes except for the northern marine based sector (northern BK Seas) which has less ice in *BS1* (figure 4.13).

EA ice sheet response to the *BS* experiments appears to be driven by regional

temperature changes and opposed by precipitation changes at all but high latitudes. *BS1* has colder JJA temperatures (up to 8°C) and also less mean annual precipitation compared to *BS0* at all transects and at both 119 ka and 112 ka (figure C.1 and C.2). The thinner northern marine ice of *BS1* occurs where *BS0* mean summertime temperatures are below -7°C, and thus a range where summertime melt would be minimal. Therefore the higher precipitation of *BS0* becomes the controlling factor.

NA ice sheet volume response to the *BS* experiments is much weaker but otherwise a similar pattern to that of EA, ie, *BS1* is the largest, then *ctrl*, and at last *BS0* (dashed lines in figure 4.1.left). The NA ice sheet volume in *BS1* is only about 20% larger than the *BS0* at the peak time. Similar to EA, the NA ice is thicker in the *BS1* ensemble at 112 ka compared to the *BS0* ensemble at lower latitudes, and slightly thinner for higher latitudes in the northern Canadian Archipelagoes (figure 4.13). However, unlike EA ice sheet, the thicker *BS1* ice in lower latitudes of NA at 112 ka correlates with higher precipitations, while the transect temperatures of the two ensembles show relatively similar temperature profiles (figure C.3).

4.4.4.1 Atlantic meridional overturning circulation

The North Atlantic meridional overturning of the *BS0* experiment is stronger than the *BS1* during almost the whole growth phase of the inception, as per discussion above. As the NA and EA ice sheets grow, the meridional overturning strengthens in both ensembles (4.14), as less freshwater drains into the Atlantic Ocean due to the build up of ice sheets. However, the meridional overturning strengthening by the inception peak in the *BS0* ensemble is ∼50% more than *BS1* (*BS0* from ∼19 Sv to ∼28 Sv, *BS1* from ∼18 Sv to ∼24 Sv). Also the meridional overturning site in the

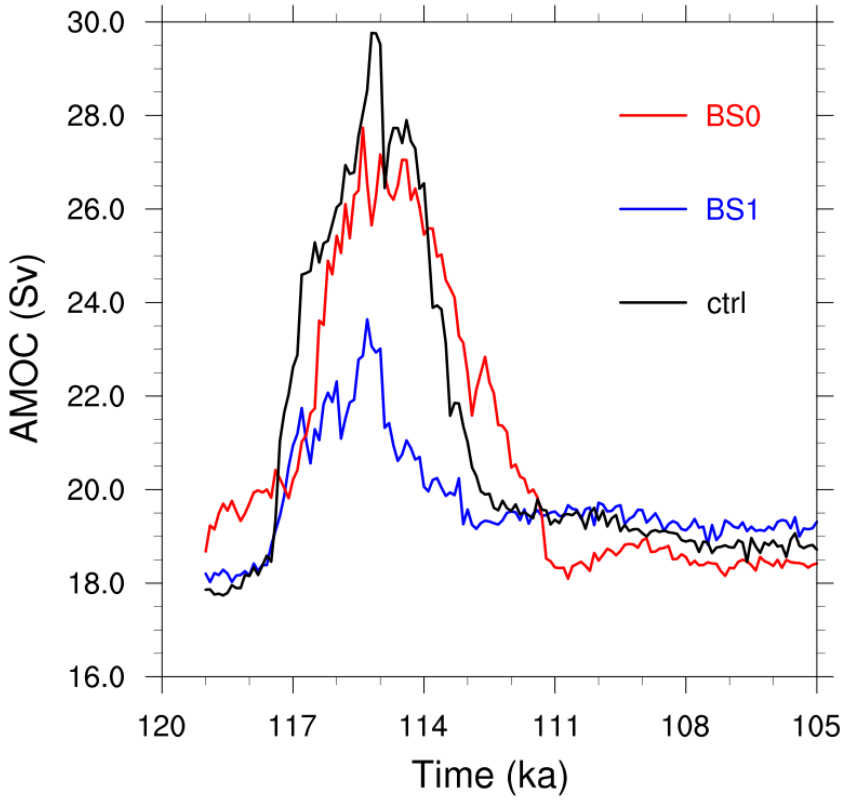

Figure 4.14: Maximum of the meridional overturning in the North Atlantic for *BS0* (red), *BS1* (blue), and the *ctrl* ensemble (black).

BS0 shifts northward in the North Atlantic. These differences are all driven by the large reduction of lower salinity Arctic outflow into the North Atlantic in the *BS0* ensemble due to the shutdown of water export from the Pacific Ocean to the Arctic.

4.4.4.2 Sea surface temperature

Comparing the sea surface temperature (SST) of the two ensembles at early inception shows that both the North Pacific and the North Atlantic oceans are colder almost everywhere in the *BS1* experiment compared to the *BS0*. However, the magnitude

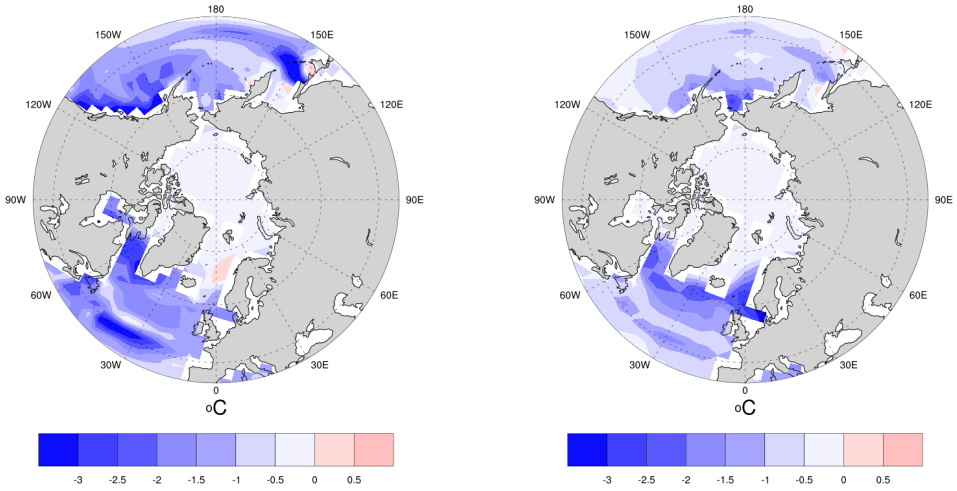

Figure 4.15: Summer mean SST difference between BS1 and BS0 in at early inception (119 ka, left plot) and inception peak (112 ka, right plot).

and distribution of the cooling is not consistent through the whole inception (figure 4.15). At the LGI peak, the *BS1* Pacific Ocean relative cooling weakens and is limited to the Bering Sea, while the cooling in the North Atlantic is more concentrated on the north of the North Atlantic and the Greenland-Iceland-Norwegian seas. The enhanced cooling of the higher latitudes of the North Atlantic would tend to reduce sub-shelf and surface melt for the western EA ice sheet. The consistent colder SSTs of the *BS1* Labrador Sea and the Bering Sea from 119 ka to 112 ka also contributes to thickening of the NA ice sheet in eastern NA and Alaska. The Arctic Ocean SST is relatively similar in the two experiments, and hence ice sheets sub-shelf melt in Barent-Kara Seas and the Canadian Archipelagoes does not decrease in the BS1 compared to the BS0.

4.4.4.3 Sea ice

As expected, the enhanced AMOC of the *BS0* experiment results in smaller sea ice area compared to the other two ensembles (4.12.right). The fully open Bering Strait of *BS1* correspondingly results in the largest sea ice area between the three ensembles. Similar to the runoff experiments, the *ctrl* and *BS0* ensembles show a double peak in sea ice area, due to the same mechanism. However, despite having the dynamic runoff scheme enabled in the *BS1* experiment, the sea ice area has only one LGI peak, between 113 ka and 112 ka. This is likely the result of a weaker AMOC and southward shift of the NADW formation location in the *BS1* ensemble, though the details behind this reduced response would require further analysis.

4.5 Conclusions

I have examined the impact of the NA and EA ice sheets on the evolution of the climate and thereby on the ice sheets themselves via a series of sensitivity experiments. This included: the impact of ice sheet orography, the impact of changing sea level and NA ice sheet expansion towards Bering Strait, and the impact of runoff adjustment. In all my experiments, the evolution of the EA ice sheet (both in terms of total volume and regional extent) is more sensitive to changes in the feedbacks exerted on the climate by ice sheets, compared to the NA ice sheet. This is in good part due to the westerlies in the mid-latitudes, which carry the effects of changes in the heat and moisture budget of the Atlantic to EA. However, the magnitude of the response varies across the EA ice sheet.

On regional scales, the eastern EA is less sensitive to variations in the NA ice sheet

configurations (topography and albedo) compared to the northern and western EA. The northern and western EA are mostly affected by the position and strength of the Atlantic low pressure, which is highly influenced by the NA ice sheet. The size of ice in northern latitudes of the EA is strongly controlled by the extent and thickness of ice in lower latitudes of the western EA, and to some extent the regional sea ice cover. Thicker ice in the western EA blocks moisture transport from mid-Atlantic to higher latitudes during the growth phase. This underlines the importance of accounting for wind direction and the higher resolution ice sheet model surface slopes in downscaling the precipitation.

The EA ice sheet is also highly sensitive to AMOC. In both the runoff and Bering Strait sensitivity ensembles, a strong AMOC results in smaller EA ice sheet. Although the NA ice sheet is less affected by variations in AMOC, my *flux0* experiment showed the impact of a strong AMOC can reach as far west as the Rockies, and prevent ice build up in this area.

In both the runoff and Bering Strait experiments, a strong and northerly located AMOC results in smaller NH sea ice, and any weakening of AMOC can increase the sea ice area. Therefore in the experiments with dynamic runoff and strong AMOC, I see a second sea ice advance during the retreat of ice sheets due to the meltwater forcing into the Atlantic and Arctic Oceans, therefore restricting the heat transport to higher latitudes. The background climate warming eventually forces the sea ice to retreat again. I do not see any similar pattern in the runs with already weak AMOCs. Further experiments are required to quantify the impact of AMOC on the sea ice evolution, and identify any possible thresholds in causing the second peak.

A major topic I have not touched is inter-hemispheric interactions. The next

version of LCice includes a dynamic Antarctic ice sheet enabling analysis of the bipolar seesaw and the associated changes in ocean circulation, sea ice extent, and the global ice sheets.

Chapter 5

Conclusions

5.1 Summary

The main objectives of this thesis are to: 1) develop a fully coupled ice/climate model incorporating to the extent possible (within a PhD research frame) all the key relevant feedbacks between ice and climate, 2) take an initial model-based step towards elucidation of the potential phase space of the ice and climate system during the last glacial inception (LGI), and 3) quantify the ice-climate feedbacks during the LGI. This entailed the following:

1. Develop a fully coupled ice-climate model (LCice) (Chapter 2) which has been publicly archived for community use

2. Define parameters and processes with uncertainties to be used for the ensemble simulations (Chapter 2)

3. Evaluate the performance of an ensemble of 2000 simulations with respect to

present-day conditions, and thereby select 500 simulations for the inception interval (Chapter 2)

4. Evaluate the performance of the selected 500 simulations with respect to the LGI, and thereby select 55 simulations for analysis (Chapter 3)

5. Examine the phase-space of ice and climate evolution during the inception in the ensemble (Chapter 3)

6. Analyze the ice/climate/ice feedbacks controlling the evolution of individual ice sheets using multiple sensitivity experiments (Chapter 4)

The LCice 1.0 model is described in detail in Chapter 2. It is the only coupled ice sheet - climate model to date that includes almost all the main feedbacks between the cryosphere, atmosphere, and ocean, while being capable of doing glacial-scale simulations on order of a month. It includes a novel precipitation downscaling scheme that accounts for orographic forcing on the much higher resolution ice sheet model grid. Temperature downscaling uses the dynamic vertical surface temperature gradient. Incorporation of these downscaling schemes increased ice growth during the inception interval. Incorporation of dynamic (topographically self-consistent) surface drainage improved capture of the retreat phase of inception (after $\sim$110 ka), which has been a challenge for many previous LGI simulations. LCice 1.0 has been shown herein to be capable of capturing both growth and retreat phases of the LGI, which prior to this work, was not possible without including ad-hoc parameterizations and bias corrections.

The parameters included in the ensemble, their ranges, and sensitivity of the cli-

mate to each of them are presented in Chapter 2. From an initial set of 2000 parameter vectors, a sub-set of 55 parameter vectors was chosen based on the performance of the model in simulating the present-day and the LGI climate and sea level variations.

5.1.1 Key results

Analysis of the above described 55 member subset of transient simulations of the LGI was presented in Chapter 3. Ensemble results indicate that cross-ensemble variance in ice evolution increases from high to low latitudes, and from the NA to EA during the growth phase. Glacial inception over NA initially follows the high latitude and high elevation nucleation paradigm. Initial nucleation occurs over the Arctic archipelago (especially Ellesmere Island) with subsequent nucleation over northeastern Baffin Island and the northwestern Cordillera. Subsequently, wide snow-field expansion across Keewatin (Northern Canada) occurs in many of the ensemble members. Around the inception ice volume peak (114 ka to 110 ka), NA ice extent is robust among simulations, with a single ice sheet covering whole Canada and central Alaska. Up to this point, 2 meter summer mean -2°C to 0°C isotherms best represent the southern margins of ice.

The main cross-ensemble variations in NA are: ice cover extent over Hudson Bay, existence of an ice bridge between Greenland and Labrador, and the position of the ice margins north of Alaska and Bering Strait. By the start of the retreat phase, these regions and the region east of the Rockies are the first areas of divergence among ensemble simulations. The northward shift of the southern margin of ice lags the temperature increase, and 2 meter summer mean 0°C to 4°C isotherms mostly bound

these margins.

EA ice volume and extent, except in Svalbard, varies across the ensemble from the beginning of the LGI to the end of the simulation interval (105 ka), ranging from a single ice sheet covering the whole northern EA, to few separate ice caps in high elevations and Svalbard. In line with the smaller size of the EA ice sheet compared to the NA ice sheet, and therefore a faster response to temperature changes, its southern margin mostly follows the 2 meter summer mean 0°C temperature.

Despite large variance in the timing of EA ice sheet peak volume across the ensemble, it always leads the NA volume peak time (between 200 years and 6 kyr). The pattern of simulated sea ice, temperature, and precipitation changes through the inception suggests that the timing of the NA stadial peak ice volume is further delayed relative to orbital forcing changes by an early increase in precipitation. The precipitation and temperature changes of EA however strongly correlate with summer sea ice, which is stable at its maximum extent for ∼3 kyr.

Sensitivity experiments examining ice sheet-climate-ice sheet feedbacks (Chapter 4) confirm higher sensitivity of the EA ice sheet to changes in the climate, compared to the NA ice sheet. Transect snapshots indicate that western EA ice extent and thickness is the main control on moisture transport to Barents-Kara and eastern EA sectors. Western EA ice has high sensitivity to the strength and location of the Atlantic low pressure, which in turn correlates with the size of the NA ice sheet. The NA ice sheet, on the other hand, is much less sensitive to the presence or absence of a dynamic EA ice sheet. The imposition of a flat EA ice sheet has a slight impact (relative to the dynamical control). However, imposition of a constant LGI stadial maximum ice volume EA ice sheet (over the simulated 119 to 105 ka interval) both

reduces NA ice growth during the early stadial and inhibits any post stadial NA ice volume reduction.

In both the runoff and the Bering Strait experiments, a double peak behaviour in Northern Hemisphere sea ice area evolution occurs under strong AMOC and dynamic runoff flux. Closure of Bering Strait, or the more blunt complete shut down of terrestrial runoff flux from the GSM grid regions, results in strengthening AMOC, and prevents ice expansion and thickening in EA, and to a lesser extent, in NA. The effect is stronger in lower latitudes compared to higher latitudes.

In summary, based on the results herein, the evolution of the EA ice sheet is very sensitive (up to factor two differences in ice volume) to parametric uncertainties, the opening/closure of Bering Strait and the presence of the NA ice sheet. Corresponding NA sensitivities are weaker but not all negligible (volume differences less than 20%).

5.2 Improving analysis

Downscaled temperature and precipitation Although the temperature and precipitation transects of the atmospheric model in Chapter 4 provides valuable information about the large-scale dependence of these two fields to different latitudes and longitudes, consideration of the downscaled fields to the GSM grid may resolve certain questions that arose with respect to the ice response to changes in temperature and precipitation.

Revised transect choices In retrospect, taking into account the main geographic differences in experimental results, the 40°E and 100°E EA transects in Chapter 4,

will be replaced by 50°E and 90°E transects. I will also include 115°W and 130°W transects for NA.

Extended sub-region analysis in Chapter 3 Based on the cross ensemble divergence of the NA ice sheet retreat pattern in Chapter 3, the addition of more analytical sector masks to cover Hudson Bay, the eastern Rockies, and northern Alaska will better quantify the ice sheet variability of the NA ice sheet.

More sensitivity runs To better isolate the orographic impact of NA and EA ice sheets, two modified control ensembles, one with Bering Strait throughflow responding only to the changes in the EA ice sheet volume, and one for the NA ice sheet volume are required.

5.3 Future work

This thesis has introduced a fully coupled ice sheet - climate model, documented the phase-space of the last glacial inception, and analyzed the associated ice/climate feedbacks. This has been a major project that required clear limits to be relegated to future work. Next steps include:

Dust parameterization As discussed, Ganopolski et al. (2010) was the only modelling study to capture the inception prior to the LCice. Their success was contingent on an ad-hoc dust parameterization and applied dust chronology. The increase in atmospheric dust and associated increased dust deposition on ice sheets during glacial periods decreases the snow/ice albedo and therefore enhances melting. The simplicity

of the Ganopolski et al. (2010) model and associated parameterizations leaves unclear the relative role of dust feedbacks in the climate system. Work is therefore ongoing towards inclusion of a dust production/transport/deposition scheme in LCice. It will account for exposed continental shelves from lower sea level, increased aridity, and higher wind speeds during glacial periods.

More ensemble parameters The next version of LCice includes more parameters to be used for ensemble studies. This new set of parameters cover a wider range of physical mechanisms involving long-wave radiative fluxes, ocean diffusivity, turbulent exchange of momentum and sensible/latent heat fluxes, albedo of vegetation.

5.3.1 Improved GSM ice dynamics

The GSM ice dynamical core has recently been upgraded to hybrid shallow ice and shallow shelf approximations to much better represent ice shelves, ice streams, and grounding line migration.

5.3.2 Inclusion of other ice sheets

Every ice sheet and possibly every major ice cap likely had significant impact on the climate system. The inclusion of the Antarctic ice sheet has been completed and is currently undergoing final testing. Future versions of the LCice will include the two currently missing ice caps that were present during the last glacial cycle: Patagonian and Himalayan (the ensembles herein included the Icelandic ice cap).

5.3.3 Phase-space of other intervals

In this study LCice 1.0 is only used to simulate the LGI. This relatively short time interval was of particular advantage during this major model development phase. The next version of LCice (with Antarctic ice sheet, more ensemble parameters, and dust parameterization) will be used to investigate the phase-space of the last two complete glacial cycles.

Dynamic land-ocean mask The sensitivity experiments in Chapter 4 indicated that LGI changes in Bering Strait through-flow can have a large impact on climate and both northern hemispheric ice sheets. The impact of global land mask and bathymetric changes over glacial intervals has yet to be quantified. The challenge is, like almost all coupled atmosphere and general circulation ocean models, LOVECLIM is not configured for a dynamical land mask (likely due to the common challenge of model instability under imposed dynamical changes).

Bibliography

Abe-Ouchi, A., Saito, F., Kawamura, K., Raymo, M. E., Okuno, J., Takahashi, K., and Blatter, H. (2013). Insolation-driven 100,000-year glacial cycles and hysteresis of ice-sheet volume. *Nature*, 500(7461):190.

Andres, H. J. and Tarasov, L. (2019). Towards understanding potential atmospheric contributions to abrupt climate changes: characterizing changes to the north atlantic eddy-driven jet over the last deglaciation. *Climate of the Past*, 15(4):1621–1646.

Andrews, J. and Barry, R. (1978). Glacial inception and disintegration during the last glaciation. *Annual Review of Earth and Planetary Sciences*, 6(1):205–228.

Arnold, N. S., Rees, W. G., Hodson, A. J., and Kohler, J. (2006). Topographic controls on the surface energy balance of a high arctic valley glacier. *Journal of Geophysical Research: Earth Surface*, 111(F2).

Bahadory, T. and Tarasov, L. (2018). Lcice 1.0 – a generalized ice sheet system model coupler for loveclim version 1.3: description, sensitivities, and validation with the glacial systems model (gsm version d2017.aug17). *Geoscientific Model Development*, 11(9):3883–3902.

Balmaseda, M. A., Vidard, A., and Anderson, D. L. T. (2008). The ecmwf ocean analysis system: Ora-s3. *Monthly Weather Review*, 136(8):3018–3034.

Bard, E., Hamelin, B., Fairbanks, R. G., and Zindler, A. (1990). Calibration of the 14C timescale over the past 30,000 years using mass spectrometric U/Th ages from Barbados corals. *Nature*, 345:405–409.

Bassford, R., Siegert, M., and Dowdeswell, J. (2006a). Quantifying the mass balance of ice caps on severnaya zemlya, russian high arctic. ii: Modeling the flow of the vavilov ice cap under the present climate. *Arctic, Antarctic, and Alpine Research*, 38(1):13–20.

Bassford, R., Siegert, M., Dowdeswell, J., Oerlemans, J., Glazovsky, A., and Macheret, Y. (2006b). Quantifying the mass balance of ice caps on severnaya zemlya, russian high arctic. i: Climate and mass balance of the vavilov ice cap. *Arctic, Antarctic, and Alpine Research*, 38(1):1–12.

Beghin, P., Charbit, S., Dumas, C., Kageyama, M., Roche, D., and Ritz, C. (2013). Interdependence of the northern hemisphere ice-sheets build-up during the last glaciation: the role of atmospheric circulation. *Climate of the Past Discussions*, 9(2).

Beghin, P., Charbit, S., Kageyama, M., Dumas, C., and Ritz, C. (2015). How might the north american ice sheet influence the northwestern eurasian climate? *Climate of the Past Discussions*, 11:27–61.

Benson, L., Kashgarian, M., and Rubin, M. (1995). Carbonate deposition, pyramid lake subbasin, nevada: 2. lake levels and polar jet stream positions reconstructed

from radiocarbon ages and elevations of carbonates (tufas) deposited in the lahontan basin. *Palaeogeography, Palaeoclimatology, Palaeoecology*, 117(1-2):1–30.

Berger, A. (2014). Milankovitch and astronomical theories of paleoclimates. In *Milankovitch Anniversary UNESCO Symposium-Water Management in Transition Countries as Impacted by Climate Change and Other Global Changes, Lessons from Paleoclimate, and Regional Issues*. Jaroslav Černi Institute for the Development of Water Resources, Belgrade (Serbia).

Berger, A. L. (1978). Long-term variations of caloric insolation resulting from the earth's orbital elements 1. *Quaternary research*, 9(2):139–167.

Birch, L., Cronin, T., and Tziperman, E. (2017). Glacial inception on Baffin Island: The role of insolation, meteorology, and topography. *Journal of Climate*, 30(11):4047–4064.

Birch, L., Tziperman, E., and Cronin, T. (2016). Glacial inception in north-east canada: The role of topography and clouds. In *EGU General Assembly Conference Abstracts*, volume 18 of *EGU General Assembly Conference Abstracts*, pages EPSC2016–948.

Braconnot, P., Otto-Bliesner, B., Harrison, S., Joussaume, S., Peterchmitt, J.-Y., Abe-Ouchi, A., Crucifix, M., Driesschaert, E., Fichefet, T., Hewitt, C., et al. (2007a). Results of PMIP2 coupled simulations of the mid-holocene and last glacial maximum–part 1: experiments and large-scale features. *Climate of the Past*, 3(2):261–277.

Braconnot, P., Otto-Bliesner, B., Harrison, S., Joussaume, S., Peterschmitt, J.-Y., Abe-Ouchi, A., Crucifix, M., Driesschaert, E., Fichefet, T., Hewitt, C. D., Kageyama, M., Kitoh, A., Laîné, A., Loutre, M.-F., Marti, O., Merkel, U., Ramstein, G., Valdes, P., L.Weber, S., Yu, Y., , and Zhao, Y. (2007b). Results of PMIP2 coupled simulations of the Mid-Holocene and Last Glacial Maximum - Part 1: Experiments and large-scale features. *Climate of the Past*, 3(2):261–277.

Bromwich, D. H., Toracinta, E. R., Oglesby, R. J., Fastook, J. L., and Hughes, T. J. (2005). LGM summer climate on the southern margin of the Laurentide ice sheet: wet or dry? *Journal of Climate*, 18(16):3317–3338.

Bromwich, D. H., Toracinta, E. R., Wei, H., Oglesby, R. J., Fastook, J. L., and Hughes, T. J. (2004). Polar MM5 simulations of the winter climate of the Laurentide ice sheet at the LGM. *Journal of Climate*, 17(17):3415–3433.

Brovkin, V., Bendtsen, J., Claussen, M., Ganopolski, A., Kubatzki, C., Petoukhov, V., and Andreev, A. (2002). Carbon cycle, vegetation, and climate dynamics in the Holocene: Experiments with the CLIMBER-2 model. *Global Biogeochemical Cycles*, 16(4).

Brovkin, V., Ganopolski, A., and Svirezhev, Y. (1997). A continuous climate-vegetation classification for use in climate-biosphere studies. *Ecological Modelling*, 101(2):251 – 261.

Calov, R., Ganopolski, A., Claussen, M., Petoukhov, V., and Greve, R. (2005). Transient simulation of the last glacial inception. part i: glacial inception as a bifurcation in the climate system. *Climate Dynamics*, 24(6):545–561.

Calov, R., Ganopolski, A., Kubatzki, C., and Claussen, M. (2009). Mechanisms and time scales of glacial inception simulated with an earth system model of intermediate complexity. *Climate of the Past*, 5(2):245–258.

Campin, J.-M. and Goosse, H. (1999). Parameterization of density-driven downsloping flow for a coarse-resolution ocean model in z-coordinate. *Tellus A: Dynamic Meteorology and Oceanography*, 51(3):412–430.

Cane, M. A., Braconnot, P., Clement, A., Gildor, H., Joussaume, S., Kageyama, M., Khodri, M., Paillard, D., Tett, S., and Zorita, E. (2006). Progress in paleoclimate modeling. *J. Clim.*, 19(20):5031–5057.

Chappell, J., Omura, A., Esat, T., McCulloch, M., Pandolfi, J., Ota, Y., and Pillans, B. (1996). Reconciliaion of late quaternary sea levels derived from coral terraces at huon peninsula with deep sea oxygen isotope records. *Earth and planetary science letters*, 141(1-4):227–236.

Charbit, S., Ritz, C., Philippon, G., Peyaud, V., and Kageyama, M. (2007). Numerical reconstructions of the Northern Hemisphere ice sheets through the last glacial-interglacial cycle. *Clim. of the Past*, 3(1):15–37.

Clark, P., Clague, J., Curry, B., Dreimanis, A., Hicock, S., Miller, G., Berger, G., Eyles, N., Lamothe, M., Miller, B., Mott, R., Oldale, R., Stea, R., Szabo, J., Thorleifson, L., and Vincent, J. (1993a). Initiation and development of the Laurentide and Cordilleran ice sheets following the last interglaciation. *Quat. Sci. Rev.*, 12(2):79–114.

Clark, P., Clague, J., Curry, B. B., Dreimanis, A., Hicock, S., Miller, G., Berger, G., Eyles, N., Lamothe, M., Miller, B., et al. (1993b). Initiation and development of the Laurentide and Cordilleran ice sheets following the last interglaciation. *Quaternary Science Reviews*, 12(2):79–114.

Clark, P. U. and Mix, A. C. (2002). Ice sheets and sea level of the last glacial maximum. *Quaternary Science Reviews*, 21(1-3):1–7.

Cleator, S., Harrison, S. P., Nichols, N., Prentice, I. C., and Roulstone, I. (2019). A new multi-variable benchmark for last glacial maximum climate simulations. *University of Reading. Dataset. DOI*, 10(1947.206).

Cohen, J., Jones, J., Furtado, J. C., and Tziperman, E. (2013). Warm arctic, cold continents: A common pattern related to arctic sea ice melt, snow advance, and extreme winter weather. *Oceanography*, 26(4):150–160.

Colleoni, F., Wekerle, C., Näslund, J.-O., Brandefelt, J., and Masina, S. (2016). Constraint on the penultimate glacial maximum northern hemisphere ice topography ($\approx$ 140 kyrs bp). *Quaternary Science Reviews*, 137:97–112.

Condron, A. and Winsor, P. (2012). Meltwater routing and the Younger Dryas. *Proc. of Nat. Acad. Sci.*, 109(49):19928–19933.

Cramer, W., Bondeau, A., Woodward, F. I., Prentice, I. C., Betts, R. A., Brovkin, V., Cox, P. M., Fisher, V., Foley, J. A., Friend, A. D., et al. (2001). Global response of terrestrial ecosystem structure and function to CO_2 and climate change: results from six dynamic global vegetation models. *Global change biology*, 7(4):357–373.

Dansgaard, W., Johnsen, S. J., Clausen, H. B., Dahl-Jensen, D., Gundestrup, N. S., Hammer, C. U., Hvidberg, C. S., Steffensen, J. P., Sveinbjornsdottir, A. E., Jouzel, J., , and Bond, G. C. (1993). Evidence for general instability of past climate from a 250 kyr ice-core record. *Nature*, 264:218–220.

De Boer, A. M. and Nof, D. (2004). The exhaust valve of the north atlantic. *Journal of climate*, 17(3):417–422.

De Noblet, N. I., Prentice, I. C., Joussaume, S., Texier, D., Botta, A., and Haxeltine, A. (1996). Possible role of atmosphere-biosphere interactions in triggering the last glaciation. *Geophysical Research Letters*, 23(22):3191–3194.

De Woul, M., Hock, R., Braun, M., Thorsteinsson, T., Jóhannesson, T., and Halldórsdóttir, S. (2006). Firn layer impact on glacial runoff: a case study at hofsjökull, iceland. *Hydrological Processes*, 20(10):2171–2185.

DeConto, R. M. and Pollard, D. (2016). Contribution of Antarctica to past and future sea-level rise. *Nature*, 531(7596):591–597.

Denton, G. H., Anderson, R. F., Toggweiler, J., Edwards, R., Schaefer, J., and Putnam, A. (2010). The last glacial termination. *science*, 328(5986):1652–1656.

Depoorter, M. A., Bamber, J., Griggs, J., Lenaerts, J. T., Ligtenberg, S. R., van den Broeke, M. R., and Moholdt, G. (2013). Calving fluxes and basal melt rates of Antarctic ice shelves. *Nature*, 502(7469):89.

Dong, B. and Valdes, P. J. (1995). Sensitivity studies of northern hemisphere

glaciation using an atmospheric general circulation model. *Journal of Climate*, 8(10):2471–2496.

Elison Timm, O., Friedrich, T., Timmermann, A., and Ganopolski, A. (2015). Separating the effects of northern hemisphere ice-sheets, co_2 concentrations and orbital parameters on global precipitation during the late pleistocene glacial cycles. *AGU Fall Meeting Abstracts*.

Erokhina, O., Rogozhina, I., Prange, M., Bakker, P., Bernales, J., Paul, A., and Schulz, M. (2017). Dependence of slope lapse rate over the greenland ice sheet on background climate. *Journal of Glaciology*, 63(239):568–572.

Etheridge, D., Barnola, J., and Morgan, V. (1998). Historical CO_2 records from the law dome de08, de08-2, and dss ice cores. Technical report, ESS-DIVE (Environmental System Science Data Infrastructure for a Virtual Ecosystem); Oak Ridge National Lab.(ORNL), Oak Ridge, TN (United States).

Fichefet, T. and Maqueda, M. A. M. (1997). Sensitivity of a global sea ice model to the treatment of ice thermodynamics and dynamics. *Journal of Geophysical Research: Oceans*, 102(C6):12609–12646.

Flowers, G. E. and Clarke, G. K. (2002). A multicomponent coupled model of glacier hydrology 1. theory and synthetic examples. *Journal of Geophysical Research: Solid Earth*, 107(B11).

Gallimore, R. and Kutzbach, J. (1996). Role of orbitally induced changes in tundra area in the onset of glaciation. *Nature*, 381(6582):503.

Gallup, C. D., Cheng, H., Taylor, F. W., and Edwards, R. L. (2002). Direct determination of the timing of sea level change during termination ii. *Science*, 295(5553):310–313.

Gallée, H., Van Yperselb, J. P., Fichefet, T., Marsiat, I., Tricot, C., and Berger, A. (1992). Simulation of the last glacial cycle by a coupled, sectorially averaged climate-ice sheet model: 2. response to insolation and CO_2 variations. *Journal of Geophysical Research: Atmospheres*, 97(D14):15713–15740.

Ganopolski, A., Calov, R., and Claussen, M. (2010). Simulation of the last glacial cycle with a coupled climate ice-sheet model of intermediate complexity. *Climate of the Past*, 6(2):229–244.

Ganopolski, A., Winkelmann, R., and Schellnhuber, H. J. (2016). Critical insolation–CO_2 relation for diagnosing past and future glacial inception. *Nature*, 529(7585):200–203.

Gardner, A. S., Sharp, M. J., Koerner, R. M., Labine, C., Boon, S., Marshall, S. J., Burgess, D. O., and Lewis, D. (2009). Near-surface temperature lapse rates over arctic glaciers and their implications for temperature downscaling. *Journal of Climate*, 22(16):4281–4298.

Gent, P. R. and Mcwilliams, J. C. (1990). Isopycnal mixing in ocean circulation models. *Journal of Physical Oceanography*, 20(1):150–155.

Gildor, H. and Tziperman, E. (2003). Sea-ice switches and abrupt climate change. *Philos. Trans. of the Roy. Soc. of London Series A*, 361:1935–1942.

Glover, R. W. (1999). Influence of spatial resolution and treatment of orography on gcm estimates of the surface mass balance of the greenland ice sheet. *Journal of Climate*, 12(2):551–563.

Goosse, H., Brovkin, V., Fichefet, T., Haarsma, R., Huybrechts, P., Jongma, J., Mouchet, A., Selten, F., Barriat, P.-Y., Campin, J.-M., Deleersnijder, E., Driesschaert, E., Goelzer, H., Janssens, I., Loutre, M.-F., Morales Maqueda, M. A., Opsteegh, T., Mathieu, P.-P., Munhoven, G., Pettersson, E. J., Renssen, H., Roche, D. M., Schaeffer, M., Tartinville, B., Timmermann, A., and Weber, S. L. (2010a). Description of the earth system model of intermediate complexity loveclim version 1.2. *Geoscientific Model Development*, 3(2):603–633.

Goosse, H., Brovkin, V., Fichefet, T., Haarsma, R., Huybrechts, P., Jongma, J., Mouchet, A., Selten, F., Barriat, P.-Y., Campin, J.-M., Deleersnijder, E., Driesschaert, E., Goelzer, H., Janssens, I., Loutre, M.-F., Morales Maqueda, M. A., Opsteegh, T., Mathieu, P.-P., Munhoven, G., Pettersson, E. J., Renssen, H., Roche, D. M., Schaeffer, M., Tartinville, B., Timmermann, A., and Weber, S. L. (2010b). Description of the Earth system model of intermediate complexity LOVECLIM version 1.2. *Geoscientific Model Development*, 3(2):603–633.

Goosse, H., Campin, J., Fichefet, T., and Deleersnijder, E. (1997). Sensitivity of a global ice–ocean model to the bering strait throughflow. *Climate Dynamics*, 13(5):349–358.

Goosse, H., Campin, J.-M., Deleersnijder, E., Fichefet, T., Mathieu, P.-P., Maqueda, M. M., and Tartinville, B. (2001). Description of the clio model version 3.0. *Institut*

d'Astronomie et de Géophysique Georges Lemaitre, Catholic University of Louvain, Belgium.

Goosse, H., Campin, J.-M., Deleersnijder, E., Mathieu, P.-P., Morales Maqueda, M. A., and Tartinville, B. (2000). Description of the clio model.

Goosse, H., Driesschaert, E., Fichefet, T., and Loutre, M.-F. (2007). Information on the early Holocene climate constrains the summer sea ice projections for the 21st century. *Climate of the Past*, 3(4):683–692.

Goosse, H., Renssen, H., Timmermann, A., and Bradley, R. S. (2005). Internal and forced climate variability during the last millennium: a model-data comparison using ensemble simulations. *Quaternary Science Reviews*, 24(12):1345–1360.

Gregory, J., Browne, O., Payne, A., Ridley, J., and Rutt, I. (2012). Modelling large-scale ice-sheet–climate interactions following glacial inception. *Climate of the Past*, 8(5):1565–1580.

Groeneveld, J., Hathorne, E. C., Steinke, S., DeBey, H., Mackensen, A., and Tiedemann, R. (2014). Glacial induced closure of the panamanian gateway during marine isotope stages (mis) 95–100 (2.5 ma). *Earth and Planetary Science Letters*, 404:296–306.

Haarsma, R., Selten, F., Opsteegh, J., Lenderink, G., and Liu, Q. (1996). Ecbilt, a coupled atmosphere ocean sea-ice model for climate predictability studies. *KNMI, De Bilt, The Netherlands*, 31.

Hahn, J., Walsh, J., Widiasih, E., and McGehee, R. (2015). Periodicity in a con-

ceptual model of glacial cycles in the absence of milankovitch forcing. *AGU Fall Meeting Abstracts*.

Harrison, S. P., Kohfeld, K. E., Roelandt, C., and Claquin, T. (2001). The role of dust in climate changes today, at the last glacial maximum and in the future. *Earth-Science Reviews*, 54(1-3):43–80.

Heinemann, M., Timmermann, A., Elison Timm, O., Saito, F., and Abe-Ouchi, A. (2014). Deglacial ice sheet meltdown: orbital pacemaking and CO_2 effects. *Climate of the Past*, 10(4):1567–1579.

Helsen, M., Van De Berg, W., Van De Wal, R., Van Den Broeke, M., and Oerlemans, J. (2013). Coupled regional climate–ice-sheet simulation shows limited greenland ice loss during the eemian. *Climate of the Past*, 9(4):1773–1788.

Hewitt, C., Stouffer, R., Broccoli, A., Mitchell, J., and Valdes, P. J. (2003). The effect of ocean dynamics in a coupled gcm simulation of the last glacial maximum. *Climate Dynamics*, 20(2-3):203–218.

Hewitt, C. D. and Mitchell, J. F. B. (1997). Radiative forcing and response of a gcm to ice age boundary conditions: cloud feedback and climate sensitivity. *Climate Dynamics*, 13(11):821–834.

Hibler, W. D. (1979). A dynamic thermodynamic sea ice model. *Journal of Physical Oceanography*, 9(4):815–846.

Hidy, A. J., Gosse, J. C., Froese, D. G., Bond, J. D., and Rood, D. H. (2013).

A latest pliocene age for the earliest and most extensive Cordilleran ice sheet in northwestern Canada. *Quaternary Science Reviews*, 61:77–84.

Hu, A., Meehl, G. A., Han, W., Otto-Bliestner, B., Abe-Ouchi, A., and Rosenbloom, N. (2015). Effects of the bering strait closure on amoc and global climate under different background climates. *Progress in Oceanography*, 132:174 – 196. Oceanography of the Arctic and North Atlantic Basins.

Hu, A., Meehl, G. A., Han, W., Timmermann, A., Otto-Bliesner, B., Liu, Z., Washington, W. M., Large, W., Abe-Ouchi, A., Kimoto, M., Lambeck, K., and Wu, B. (2012). Role of the bering strait on the hysteresis of the ocean conveyor belt circulation and glacial climate stability. *Proceedings of the National Academy of Sciences*, 109(17):6417–6422.

Hu, A., Meehl, G. A., Otto-Bliesner, B. L., Waelbroeck, C., Han, W., Loutre, M.-F., Lambeck, K., Mitrovica, J. X., and Rosenbloom, N. (2010). Influence of bering strait flow and north atlantic circulation on glacial sea-level changes. *Nature Geoscience*, 3(2):118.

Hu, A., Otto-Bliesner, B. L., Meehl, G. A., Han, W., Morrill, C., Brady, E. C., and Briegleb, B. (2008). Response of thermohaline circulation to freshwater forcing under present-day and LGM conditions. *Journal of Climate*, 21(10):2239–2258.

Huybers, P. and Tziperman, E. (2008). Integrated summer insolation forcing and 40,000-year glacial cycles: The perspective from an ice-sheet/energy-balance model. *Paleoceanography*, 23(1).

Huybrechts, P. (2002). Sea-level changes at the LGM from ice-dynamic reconstructions of the Greenland and Antarctic ice sheets during the glacial cycles. *Quat. Sci. Rev.*, 21(1-3):203–231.

Ivanovic, R. F., Gregoire, L. J., Kageyama, M., Roche, D. M., Valdes, P. J., Burke, A., Drummond, R., Peltier, W. R., and Tarasov, L. (2016). Transient climate simulations of the deglaciation 21–9 thousand years before present (version 1) – PMIP4 core experiment design and boundary conditions. *Geoscientific Model Development*, 9(7):2563–2587.

Jacobs, S., Hellmer, H., Doake, C., Jenkins, A., and Frolich, R. (1992). Melting of ice shelves and the mass balance of Antarctica. *J. Glaciol*, 38(130):375–387.

Johns, T. C., Carnell, R. E., Crossley, J. F., Gregory, J. M., Mitchell, J. F. B., Senior, C. A., Tett, S. F. B., and Wood, R. A. (1997). The second hadley centre coupled ocean-atmosphere gcm: model description, spinup and validation. *Climate Dynamics*, 13(2):103–134.

Jouzel, J., Masson-Delmotte, V., Cattani, O., Dreyfus, G., Falourd, S., Hoffmann, G., Minster, B., Nouet, J., Barnola, J., Chappellaz, J., et al. (2007). Epica dome c ice core 800kyr deuterium data and temperature estimates. *IGBP PAGES/World Data Center for Paleoclimatology data contribution series*, 91:2007.

Kageyama, M., Charbit, S., Ritz, C., Khodri, M., and Ramstein, G. (2004). Quantifying ice-sheet feedbacks during the last glacial inception. *Geophysical Research Letters*, 31(24).

Kageyama, M., Merkel, U., Otto-Bliesner, B., Prange, M., Abe-Ouchi, A., Lohmann, G., Ohgaito, R., Roche, D., Singarayer, J., Swingedouw, D., et al. (2013a). Climatic impacts of fresh water hosing under last glacial maximum conditions: a multi-model study. *Climate of the Past*, 9(2):935–953.

Kageyama, M., Merkel, U., Otto-Bliesner, B., Prange, M., Abe-Ouchi, A., Lohmann, G., Ohgaito, R., Roche, D. M., Singarayer, J., Swingedouw, D., and Zhang, X. (2013b). Climatic impacts of fresh water hosing under Last Glacial Maximum conditions: a multi-model study. *Clim. of the Past*, 9(2):935–953.

Kageyama, M. and Valdes, P. J. (2000). Impact of the north american ice-sheet orography on the last glacial maximum eddies and snowfall. *Geophysical Research Letters*, 27(10):1515–1518.

Khazendar, A., Rignot, E., Schroeder, D. M., Seroussi, H., Schodlok, M. P., Scheuchl, B., Mouginot, J., Sutterley, T. C., and Velicogna, I. (2016). Rapid submarine ice melting in the grounding zones of ice shelves in West Antarctica. *Nature communications*, 7:13243.

Kleman, J., Fastook, J., Ebert, K., Nilsson, J., and Caballero, R. (2013). Pre-LGM northern hemisphere ice sheet topography. *Climate of the Past*, 9(5).

Krebs, U. and Timmermann, A. (2007). Tropical air–sea interactions accelerate the recovery of the atlantic meridional overturning circulation after a major shutdown. *Journal of Climate*, 20(19):4940–4956.

Kutzbach, J. E. and Guetter, P. J. (1986). The influence of changing orbital param-

eters and surface boundary conditions on climate simulations for the past 18000 years. 43(16):1726–1759.

Lambeck, K. and Chappell, J. (2001). Sea level change through the last glacial cycle. *Science*, 292(5517):679–686.

Lambeck, K., Rouby, H., Purcell, A., Sun, Y., and Sambridge, M. (2014). Sea level and global ice volumes from the last glacial maximum to the holocene. *Proceedings of the National Academy of Sciences*, 111(43):15296–15303.

Le Morzadec, K., Tarasov, L., Morlighem, M., and Seroussi, H. (2015). A new subgrid surface mass balance and flux model for continental-scale ice sheet modelling: testing and last glacial cycle. *Geoscientific Model Development*, 8(10):3199–3213.

Liakka, J. (2011). *The mutual interaction between the time-mean atmospheric circulation and continental-scale ice sheets*. PhD thesis, Department of Meteorology, Stockholm University.

Liakka, J., Löfverström, M., and Colleoni, F. (2016). The impact of the North American glacial topography on the evolution of the eurasian ice sheet over the last glacial cycle.

Lisiecki, L. E. and Raymo, M. E. (2005). A pliocene-pleistocene stack of 57 globally distributed benthic δ^{18}o records. *Paleoceanography*, 20(1).

Liu, S., Jiang, D., and Lang, X. (2018). A multi-model analysis of moisture changes during the last glacial maximum. *Quaternary Science Reviews*, 191:363–377.

Liu, Z., Otto-Bliesner, B. L., He, F., Brady, E. C., Tomas, R., Clark, P. U., Carlson, A. E., Lynch-Stieglitz, J., Curry, W., Brook, E., Erickson, D., Jacob, R., Kutzbach, J., and Cheng, J. (2009). Transient simulation of last deglaciation with a new mechanism for bølling-allerød warming. *Science*, 325(5938):310–314.

Mairesse, A., Goosse, H., Mathiot, P., Wanner, H., and Dubinkina, S. (2013). Investigating the consistency between proxy-based reconstructions and climate models using data assimilation: a mid-holocene case study. *Climate of the Past*, 9(6):2741–2757.

Manabe, S. and Broccoli, A. J. (1985). The influence of continental ice sheets on the climate of an ice age. *Journal of Geophysical Research: Atmospheres*, 90(D1):2167–2190.

Manabe, S., Stouffer, R., Spelman, M., and Bryan, K. (1991). Transient responses of a coupled ocean–atmosphere model to gradual changes of atmospheric CO_2. part i. annual mean response. *Journal of Climate*, 4(8):785–818.

Marshall, S. J., Sharp, M. J., Burgess, D. O., and Anslow, F. S. (2007). Near-surface-temperature lapse rates on the prince of wales icefield, ellesmere island, canada: implications for regional downscaling of temperature. *International Journal of Climatology*, 27(3):385–398.

Maslin, M. A. and Ridgwell, A. J. (2005). Mid-pleistocene revolution and the 'eccentricity myth'. *Geological Society, London, Special Publications*, 247(1):19–34.

McManus, J. F., Francois, R., Gherardi, J.-M., Keigwin, L. D., and Brown-Leger, S.

(2004). Collapse and rapid resumption of atlantic meridional circulation linked to deglacial climate changes. *Nature*, 428(6985):834–837.

Meissner, K., Weaver, A., Matthews, H., and Cox, P. (2003). The role of land surface dynamics in glacial inception: a study with the uvic earth system model. *Climate Dynamics*, 21(7-8):515–537.

Monnin, E., Indermühle, A., Dällenbach, A., Flückiger, J., Stauffer, B., Stocker, T. F., Raynaud, D., and Barnola, J.-M. (2001). Atmospheric CO_2 concentrations over the last glacial termination. *Science*, 291(5501):112–114.

Morzadec, K. L. and Tarasov, L. (2017). The impact of fjords on ice sheets and their subgrid representation in models. *The Cryosphere Discuss.*

Nikolova, I., Yin, Q., Berger, A., Singh, U. K., and Karami, M. P. (2013). The last interglacial (eemian) climate simulated by loveclim and ccsm3. *Climate of the Past*, 9(4):1789. Copyright - Copyright Copernicus GmbH 2013; Last updated - 2013-09-13.

Opsteegh, J. D., Haarsma, R. J., Selten, F. M., and Kattenberg, A. (1998). Ecbilt: a dynamic alternative to mixed boundary conditions in ocean models. *Tellus A*, 50(3):348–367.

Otto-Bliesner, B. L. and Brady, E. C. (2010). The sensitivity of the climate response to the magnitude and location of freshwater forcing: last glacial maximum experiments. *Quaternary Science Reviews*, 29(1):56 – 73. Climate of the Last Million Years: New Insights from EPICA and Other Records.

Otto-Bliesner, B. L., Brady, E. C., Clauzet, G., Tomas, R., Levis, S., and Kothavala, Z. (2006). Last glacial maximum and holocene climate in ccsm3. *Journal of Climate*, 19(11):2526–2544.

Peltier, W. and Fairbanks, R. G. (2006). Global glacial ice volume and last glacial maximum duration from an extended barbados sea level record. *Quaternary Science Reviews*, 25(23-24):3322–3337.

Pollard, D. (2010). A retrospective look at coupled ice sheet-climate modeling. *Climatic Change*, 100(1):173–194.

Pollard, D. and PMIP-participating groups (2000). Comparisons of ice-sheet surface mass budgets from paleoclimate modeling intercomparison project (pmip) simulations. *Glob. and Planet. Change.*, 24:79–106.

Pollard, D. and Thompson, S. L. (1997). Climate and ice-sheet mass balance at the last glacial maximum from the genesis version 2 global climate model. *Quaternary Science Reviews*, 16(8):841–863.

Rahmstorf, S. (1995). Bifurcations of the atlantic thermohaline circulation in response to changes in the hydrological cycle. *Nature*, 378(6553):145.

Rahmstorf, S., Crucifix, M., Ganopolski, A., Goosse, H., Kamenkovich, I., Knutti, R., Lohmann, G., Marsh, R., Mysak, L. A., Wang, Z., et al. (2005). Thermohaline circulation hysteresis: A model intercomparison. *Geophysical Research Letters*, 32(23).

Raper, S. C. and Braithwaite, R. J. (2006). Low sea level rise projections from mountain glaciers and icecaps under global warming. *Nature*, 439(7074):311.

Renssen, H., Seppä, H., Heiri, O., Roche, D., Goosse, H., and Fichefet, T. (2009). The spatial and temporal complexity of the holocene thermal maximum. *Nature Geoscience*, 2(6):411–414.

Ridley, J. K., Huybrechts, P., Gregory, J. M., and Lowe, J. A. (2005). Elimination of the greenland ice sheet in a high CO_2 climate. *Journal of Climate*, 18(17):3409–3427.

Rignot, E., Jacobs, S., Mouginot, J., and Scheuchl, B. (2013). Ice-shelf melting around Antarctica. *Science*, 341(6143):266–270.

Rind, D., Peteet, D., and Kukla, G. (1989). Can milankovitch orbital variations initiate the growth of ice sheets in a general circulation model? *Journal of Geophysical Research: Atmospheres*, 94(D10):12851–12871.

Roberts, W. H. G., Valdes, P. J., and Payne, A. J. (2014). Topography's crucial role in heinrich events. *Proceedings of the National Academy of Sciences*.

Roche, D., Crosta, X., and Renssen, H. (2012). Evaluating southern ocean sea-ice for the last glacial maximum and pre-industrial climates: PMIP-2 models and data evidence. *Quaternary Science Reviews*, 56:99–106.

Roche, D. M., Dokken, T. M., Goosse, H., Renssen, H., and Weber, S. L. (2007). Climate of the Last Glacial Maximum: sensitivity studies and model-data comparison with the LOVECLIM coupled model. *Climate of the Past*, 3(2):205–224.

Roche, D. M., Dumas, C., Bügelmayer, M., Charbit, S., and Ritz, C. (2014). Adding a dynamical cryosphere to iloveclim (version 1.0): coupling with the grisli ice-sheet model. *Geoscientific Model Development*, 7(4):1377–1394.

Roche, D. M., Wiersma, A. P., and Renssen, H. (2010). A systematic study of the impact of freshwater pulses with respect to different geographical locations. *Climate Dynamics*, 34(7-8):997–1013.

Roe, G. H. and Lindzen, R. S. (2001). The mutual interaction between continental-scale ice sheets and atmospheric stationary waves. *Journal of Climate*, 14(7):1450–1465.

Rossow, W. B. (1996). *International Satellite Cloud Climatology Project (ISCCP): New radiance calibrations*. World Meteorological Organization.

Ruddiman, W. F. (2003). Orbital insolation, ice volume, and greenhouse gases. *Quaternary Science Reviews*, 22(15-17):1597–1629.

Shackleton, N. (1987). Oxygen isotopes, ice volume and sea level. *Quaternary Science Reviews*, 6(3-4):183–190.

Shaffer, G. and Bendtsen, J. (1994). Role of the bering strait in controlling north atlantic ocean circulation and climate. *Nature*, 367(6461):354–357.

Shin, S.-I., Liu, Z., Otto-Bliesner, B. L., Kutzbach, J. E., and Vavrus, S. J. (2003). Southern ocean sea-ice control of the glacial north atlantic thermohaline circulation. *Geophysical Research Letters*, 30(2).

Shine, K. and Henderson-Sellers, A. (1985). The sensitivity of a thermodynamic sea ice model to changes in surface albedo parameterization. *Journal of Geophysical Research: Atmospheres*, 90(D1):2243–2250.

Siddall, M., Rohling, E., Almogi-Labin, A., Hemleben, C., Meischner, D., Schmelzer, I., and Smeed, D. (2006). Red sea sea level reconstruction. *IGBP PAGES/World Data Center for Paleoclimatology Data Contribution Series*, 63.

Siddall, M., Rohling, E. J., Almogi-Labin, A., Hemleben, C., Meischner, D., Schmelzer, I., and Smeed, D. (2003). Sea-level fluctuations during the last glacial cycle. *Nature*, 423(6942):853–858.

Stephens, B. B. and Keeling, R. F. (2000). The influence of Antarctic sea ice on glacial–interglacial CO_2 variations. *Nature*, 404(6774):171.

Stokes, C. R., Tarasov, L., and Dyke, A. S. (2012). Dynamics of the north american ice sheet complex during its inception and build-up to the last glacial maximum. *Quaternary Science Reviews*, 50:86–104.

Stouffer, R. J., Yin, J., Gregory, J. M., Dixon, K. W., Spelman, M. J., Hurlin, W., Weaver, A. J., Eby, M., Flato, G. M., Hasumi, H., Hu, A., Jungclaus, J. H., Kamenkovich, I. V., Levermann, A., Montoya, M., Murakami, S., Nawrath, S., Oka, A., Peltier, W. R., Robitaille, D. Y., Sokolov, A., Vettoretti, G., and Weber, S. L. (2006). Investigating the causes of the response of the thermohaline circulation to past and future climate changes. *Journal of Climate*, 19(8):1365–1387.

Svendsen, J. I., Alexanderson, H., Astakhov, V. I., Demidov, I., Dowdeswell, J. A., Funder, S., Gataullin, V., Henriksen, M., Hjort, C., Houmark-Nielsen, M., et al.

(2004). Late quaternary ice sheet history of northern eurasia. *Quaternary Science Reviews*, 23(11):1229–1271.

Takahashi, K. (1998). The bering and okhotsk seas: modern and past paleoceanographic changes and gateway impact. *Journal of Asian Earth Sciences*, 16(1):49–58.

Tarasov, L., Dyke, A. S., Neal, R. M., and Peltier, W. R. (2012). A data-calibrated distribution of deglacial chronologies for the North American ice complex from glaciological modeling. *epsl*, 315-316:30–40.

Tarasov, L. and Peltier, W. R. (1997a). A high-resolution model of the 100 kyr ice age cycle. *Ann. Glaciol.*, 25:58–65.

Tarasov, L. and Peltier, W. R. (1997b). Terminating the 100 kyr ice age cycle. *jgr*, 102(D18):21665–21693.

Tarasov, L. and Peltier, W. R. (2002). Greenland glacial history and local geodynamic consequences. *Geophys. J. Int.*, 150:198–229.

Tarasov, L. and Peltier, W. R. (2003). Greenland glacial history, borehole constraints and Eemian extent. *J. Geophys. Res.*, 108(B3):2124–2143.

Tarasov, L. and Peltier, W. R. (2004). A geophysically constrained large ensemble analysis of the deglacial history of the North American ice sheet complex. *Quat. Sci. Rev.*, 23:359–388.

Tarasov, L. and Peltier, W. R. (2006). A calibrated deglacial drainage chronology for the North American continent: Evidence of an Arctic trigger for the Younger Dryas. *qsr*, 25(7-8):659–688.

Tarasov, L. and Peltier, W. R. (2007). The co-evolution of continental ice cover and permafrost extent over the last glacial-interglacial cycle in North America. *JGR-Earth Surface*, 112(F02S08):doi:10.1029/2006JF000661.

Thomas, R. H., Abdalati, W., Frederick, E., Krabill, W. B., Manizade, S., and Steffen, K. (2003). Investigation of surface melting and dynamic thinning on jakobshavn isbræ, greenland. *Journal of Glaciology*, 49(165):231–239.

Timmermann, A., Gildor, H., Schulz, M., and Tziperman, E. (2003). Coherent resonant millennial-scale climate oscillations triggered by massive meltwater pulses. *Journal of Climate*, 16(15):2569–2585.

Ullman, D., LeGrande, A., Carlson, A. E., Anslow, F., and Licciardi, J. (2014). Assessing the impact of Laurentide ice-sheet topography on glacial climate.

Uppala, S. M., Kållberg, P., Simmons, A., Andrae, U., Bechtold, V. D. C., Fiorino, M., Gibson, J., Haseler, J., Hernandez, A., Kelly, G., et al. (2005). The era-40 re-analysis. *Quarterly Journal of the Royal Meteorological Society: A journal of the atmospheric sciences, applied meteorology and physical oceanography*, 131(612):2961–3012.

van den Broeke, M., Smeets, P., Ettema, J., and Munneke, P. K. (2008). Surface radiation balance in the ablation zone of the west greenland ice sheet. *Journal of Geophysical Research: Atmospheres*, 113(D13).

van Lent, J. (2013). Coupling an ice sheet model to ec-earth. Master's thesis.

van Meerbeeck, C. J., Renssen, H., and Roche, D. M. (2009). How did marine isotope

stage 3 and last glacial maximum climates differ? - perspectives from equilibrium simulations. *Climate of the Past*, 5:33–51.

Vettoretti, G. and Peltier, W. (2004). Sensitivity of glacial inception to orbital and greenhouse gas climate forcing. *Quaternary Science Reviews*, 23(3-4):499–519.

Vettoretti, G. and Peltier, W. R. (2003). Post-eemian glacial inception. part i: The impact of summer seasonal temperature bias. *Journal of Climate*, 16(6):889–911.

Vettoretti, G., Peltier, W. R., and McFarlane, N. A. (2000). Global balance and atmospheric water vapour transport at Last Glacial Maximum: Climate simulations with the CCCma atmospheric general circulation model. *Can. J. Earth Sci.*, 7:695–723.

Waelbroeck, C., Labeyrie, L., Michel, E., Duplessy, J. C., McManus, J., Lambeck, K., Balbon, E., and Labracherie, M. (2002). Sea-level and deep water temperature changes derived from benthic foraminifera isotopic records. *Quaternary Science Reviews*, 21(1):295–305.

Walsh, J., Chapman, W., and Fetterer, F. (2015). Gridded monthly sea ice extent and concentration, 1850 onward, version 1. Technical report, NSIDC: National Snow and Ice Data Center, Boulder, Colorado USA.

Wang, Z. and Mysak, L. A. (2002). Simulation of the last glacial inception and rapid ice sheet growth in the mcgill paleoclimate model. *Geophysical Research Letters*, 29(23).

Weertman, J. (1964). Rate of growth or shrinkage of nonequilibrium ice sheets. *Journal of Glaciology*, 5(38):145–158.

Widmann, M., Goosse, H., van der Schrier, G., Schnur, R., and Barkmeijer, J. (2010). Using data assimilation to study extratropical northern hemisphere climate over the last millennium. *Climate of the Past*, 6(5):627–644.

Xu, Y., Rignot, E., Fenty, I., Menemenlis, D., and Flexas, M. M. (2013). Subaqueous melting of store glacier, west greenland from three-dimensional, high-resolution numerical modeling and ocean observations. *Geophysical Research Letters*, 40(17):4648–4653.

Xun, G., Gregor, K., Gerrit, L., and Xu, Z. (2013). Dependence of abrupt atlantic meridional ocean circulation changes on climate background states. *Geophysical Research Letters*, 40(14):3698–3704.

Yin, Q., Berger, A., Ganopolski, A., Goelzer, H., Guo, Z., and Huybrechts, P. (2014). Ice sheets, insolation and CO_2 during the interglacial mis-13. In *EGU General Assembly Conference Abstracts*, volume 16 of *EGU General Assembly Conference Abstracts*, page 2910.

Appendix A

Supplementary material for: LCice 1.0: A generalized Ice Sheet Systems Model coupler for LOVECLIM version 1.3: description, sensitivities, and validation with the Glacial Systems Model (GSM version D2017.aug17)

A.1 Runoff routing

LOVECLIM has 26 predefined water discharge zones globally (colored cells in figure 1 (only the NH)) abutting continental margins within which the runoff flux calculated by the land model is uniformly distributed. The coupler then receives the GSM discharge at either continental margins or the terrestrial GSM grid boundaries (black lines in figure A.1).

In the case of the continental margin, all the GSM drainage in regions bounded by same-color brackets are directed into LOVECLIM drainage cells with the similar color as the brackets. For instance, the GSM drainage south of Alaska between the two purple brackets is dumped into the four LOVECLIM purple cells in the same region. The LOVECLIM drainage module uniformly redistributes this discharge across the drainage cells within a given region.

Over the terrestrial GSM grid boundaries, the GSM runoff between same-color brackets are redirected to LOVECLIM drainage cells based on PD drainage maps. The GSM drainage in these regions is added to the runoff calculated by LOVECLIM from regions not covered by GSM grids. For instance, southern Europe runoff between the olive-green brackets are redirected into the Mediterranean, in addition to the runoff calculated by LOVECLIM from southern Europe and northern Africa.

For the south-eastern Eurasian margin of the GSM grid, the GSM runoff is directed to the Pacific ocean for the following reason. Most of the drainage in this largely dry region is northward except for that of the Caspian Sea watershed. As this sea is absent in LOVECLIM and all its mass-loss is evaporative, prevailing westerly winds would dictate predominantly eastward transport of moisture.

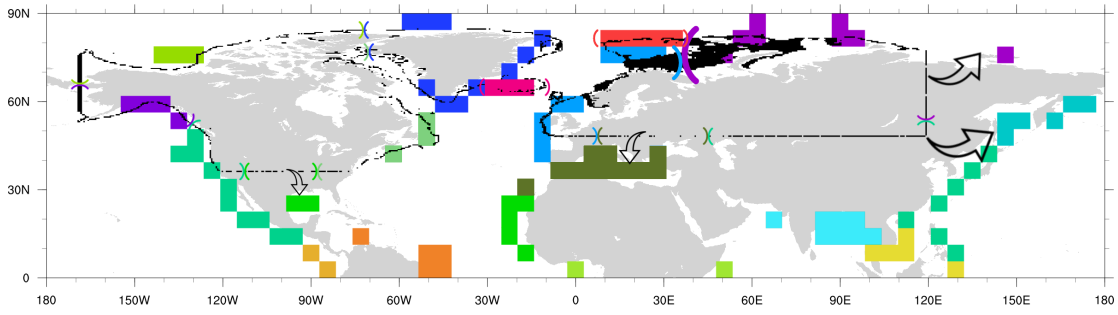

Figure A.1: GSM (black lines) and LOVECLIM (colored cells) drainage sites. The colored brackets show the regions for which the GSM drainage is captured by the coupler and dumped into LOVECLIM drainage sites with the same color. The arrows show the GSM runoff at the GSM grid boundaries redirected to the appropriate ocean basin.

A.2 LOVECLIM 2-meter and surface temperature comparison

PDD ablation models are based on nominal 2 meter air temperatures and as such I use the 2 meter temperature from LOVECLIM. The use of surface temperatures in PDD models will give erroneous results as surface temperatures on ice and snow can not be above 0°C even when air temperature is. I note that the LOVECLIM based modelling of Roche et al. (2014) uses surface temperatures for PDD ablation calculation but without justification. To examine the implications of this choice, I compare LOVECLIM present-day bias and root mean square error (RMSE) to ERA reanalysis results Uppala et al. (2005) in Table A.1. Given the simplified boundary layer physics of LOVECLIM, I also compare an average of LOVECLIM 2 meter and

surface temperatures ($\bar{T}$). For surface mass balance contexts, summertime temperatures are most relevant. LOVECLIM July surface temperature (TS) has the worst RMSE relative to ERA40 globally and over both EA and NA. LOVECLIM 2 meter temperature ($T2m$) has the worst July RMSE over Antarctica and Greenland though the latter is only 0.5°C larger than that of TS and $\bar{T}$. Furthermore, LOVECLIM $T2m$ has the smallest July bias and RMSE for terrestrial NA and EA. LOVECLIM $T2m$ also has the lowest global bias and RMSE for both July and February, over both land and ocean (except for being with 0.1°C of the lowest RSME for July global ocean). These results are for the default LOVECLIM tuning and retuning may provide better fits with $\bar{T}$.

Table A.1: The difference between the LOVECLIM two meter air temperature (T2m), LOVECLIM surface temperature (TS), T2m and TS average ($\bar{T}$), and the ERA40 two meter air temperature Uppala et al. (2005), in Feburary and July at year 2000 A.D. The ERA40 temperature is corrected using the lapse-rate extracted from LOVECLIM to the same elevation as LOVECLIM topography. The means and root mean square errors (RMSE) are calculated by averaging the temperature differences over the each region (Global, North America (NA), Eurasia (EA), Greenland (Gr), and Antarctic), considering only the land mask (land), the ocean mask (ocean), and the boundaries shown in the map plots of the paper (all). Boldface values indicate the smallest mean differences (in magnitude) and RMSEs in each row.

			$T2m$		TS		$\bar{T}$	
			Mean	RMSE	Mean	RMSE	Mean	RMSE
Global	FEB	land	**1.003**	**4.531**	1.579	5.881	1.290	4.635
		all	**0.644**	**3.660**	1.951	4.467	1.297	3.727
		ocean	**0.504**	**3.261**	2.094	3.781	1.299	3.309
	JUL	land	**1.122**	**5.142**	4.359	6.984	2.74	5.162
		all	**0.522**	4.049	2.471	4.867	1.496	**3.972**
		ocean	**0.290**	3.537	1.740	3.738	1.015	**3.402**
NA	FEB	land	3.494	6.081	**0.549**	**3.353**	2.022	4.434
		all	4.069	6.399	**2.290**	**5.521**	3.179	5.607
		ocean	**5.008**	**6.889**	5.138	7.872	5.073	7.122
	JUL	land	**2.948**	**5.066**	5.952	7.190	4.450	5.833
		all	**2.587**	**4.964**	3.958	6.062	3.273	5.157
		ocean	1.997	4.793	**0.6951**	**3.507**	1.346	3.798
EA	FEB	land	1.542	**4.650**	-3.060	6.574	**-0.759**	5.018
		all	**-0.201**	5.477	-2.764	6.626	-1.482	**5.449**
		ocean	-4.542	7.131	**-2.026**	6.753	-3.284	**6.398**
	JUL	land	**3.209**	**4.113**	8.284	9.323	5.746	6.597
		all	**2.181**	**3.821**	5.830	8.139	4.005	5.835
		ocean	-0.3784	**2.974**	**-0.278**	3.842	-0.328	3.232
GR	FEB	land	3.107	7.846	**-0.281**	8.140	1.413	**7.394**
		all	**2.979**	**7.471**	3.753	9.349	3.366	7.952
		ocean	**2.895**	**7.215**	6.400	10.060	4.648	8.299
	JUL	land	3.012	3.945	**1.192**	3.477	2.102	**3.455**
		all	3.027	4.042	**1.545**	**3.452**	2.286	3.489
		ocean	3.036	4.104	**1.777**	**3.435**	2.406	3.510
AA	FEB	land	3.499	7.151	**-0.771**	**5.361**	1.364	5.726
		all	1.630	5.139	**0.668**	**4.521**	1.149	4.546
		ocean	**0.722**	**3.796**	1.366	4.051	1.044	3.845
	JUL	land	6.983	13.250	-5.872	10.310	**0.556**	**9.760**
		all	**-0.198**	10.170	-4.292	9.333	-2.245	**8.797**
		ocean	-3.683	**8.276**	**-3.525**	8.818	-3.604	8.290

Appendix B

Supplementary material for: The phase space of last glacial inception

B.1 Sea ice

The Atlantic sea ice area variation pattern also follows the total NH sea ice area. While the maximum sea ice extent is less variable through time, the minimum sea ice extent reaches its largest extent around 114 ka, and its smallest extent between 107 and 105 ka. Regardless of the the glacial stage I are in (growth or shrink phase), the southward extent of the sea ice in the North Atlantic can never move below the 44°N (the same latitude as the jet-stream over the North Atlantic), which is reached shortly after entering the glacial period. This results in flattening the sea ice area oscillation I expect to see through the first 20 kyr of the simulations. The minimum extent on the other hand, is well north of the 44°N, therefore can freely oscillate with the cooling and warming of the stadial and interstadial phases (9th month in figure

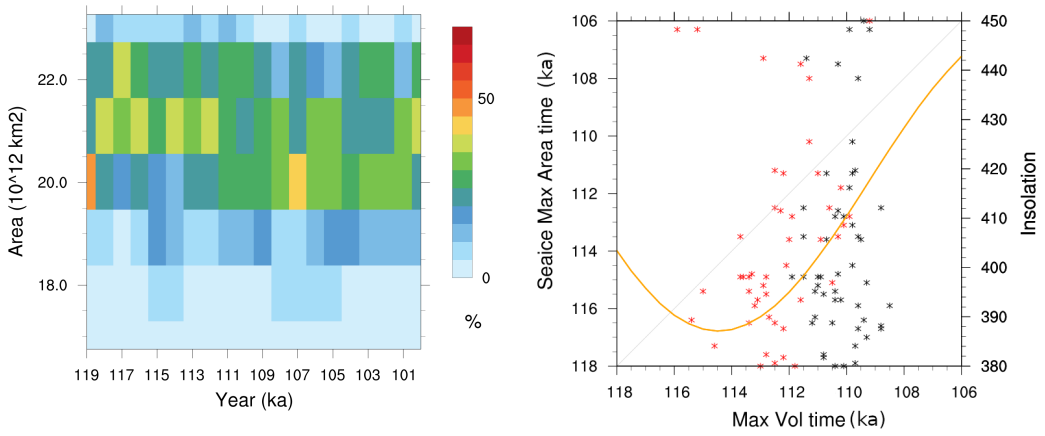

Figure B.1: Ensemble distribution of the NH maximum sea ice during the inception period. **b**. Timing of the late-winter sea ice area maximum against timing of the NA (black) and EA (red) ice sheet maximum volumes.

B.2).

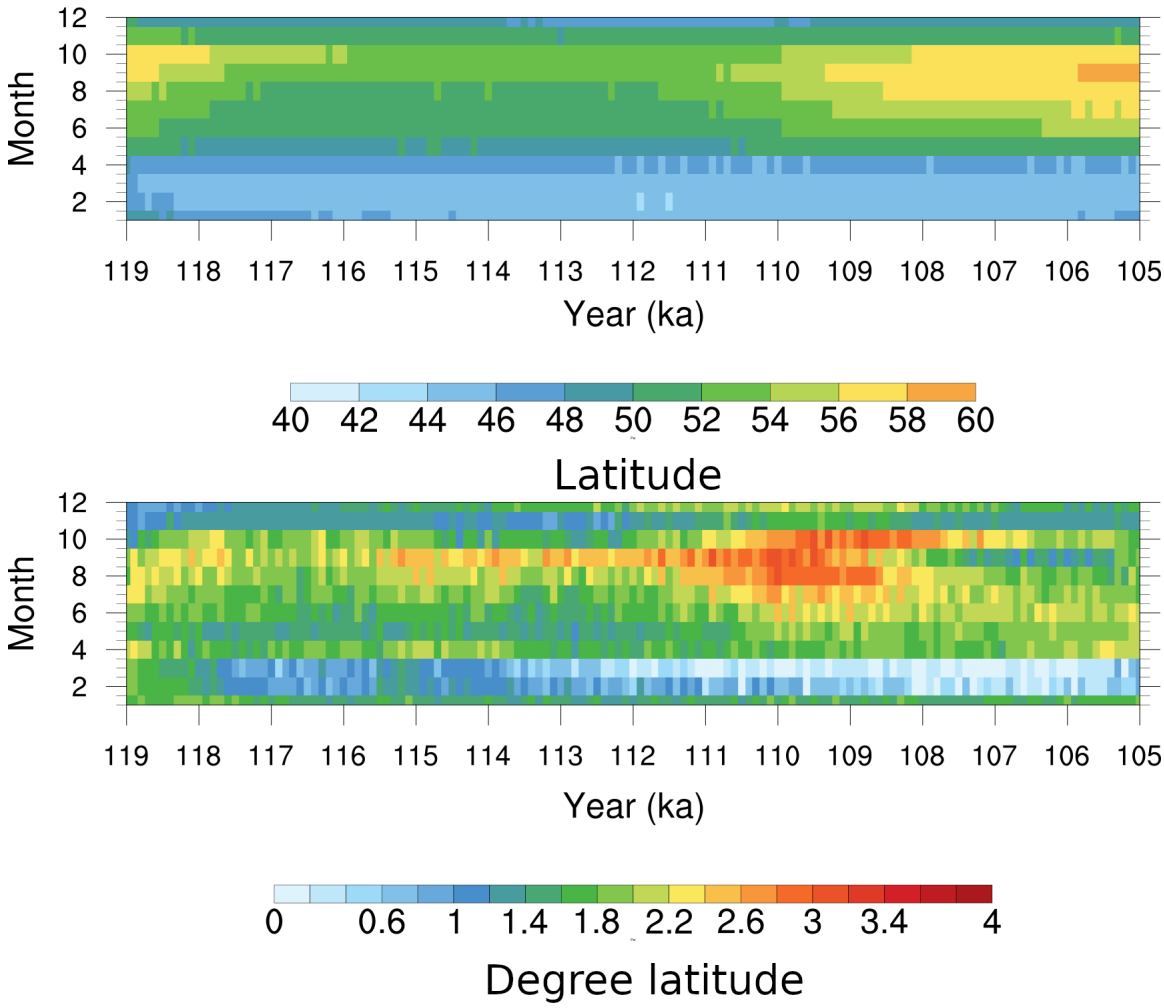

Figure B.2: Monthly lowest latitude of the sea ice in the North Atlantic from 119 ka to 105 ka. Vertical axis shows each month, and the horizontal axis is the simulation year. Colors represent the lowest latitude. **top** ensemble mean, and **bottom** ensemble standard deviation.

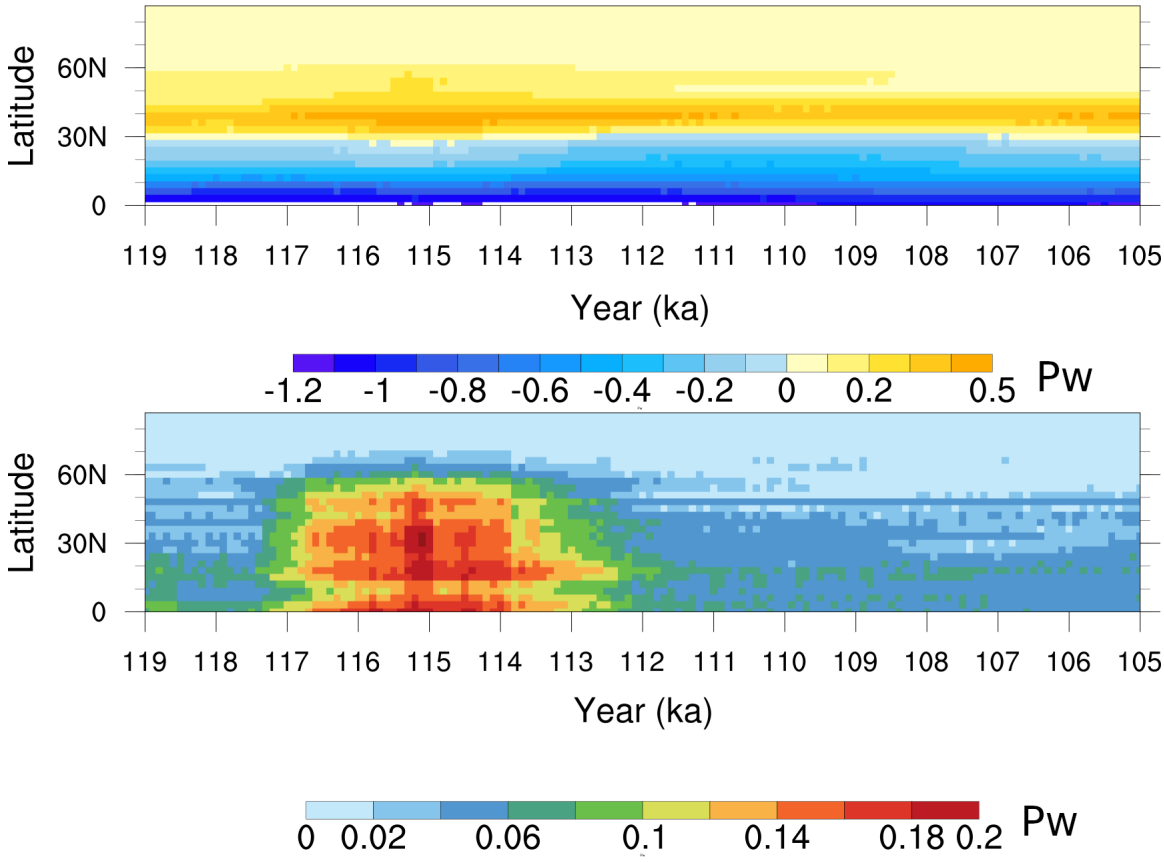

Figure B.3: Atlantic meridional northward heat transport **top**. ensemble mean and, **bottom**. standard deviation through the LGI.

B.2 Atlantic meridional heat transport

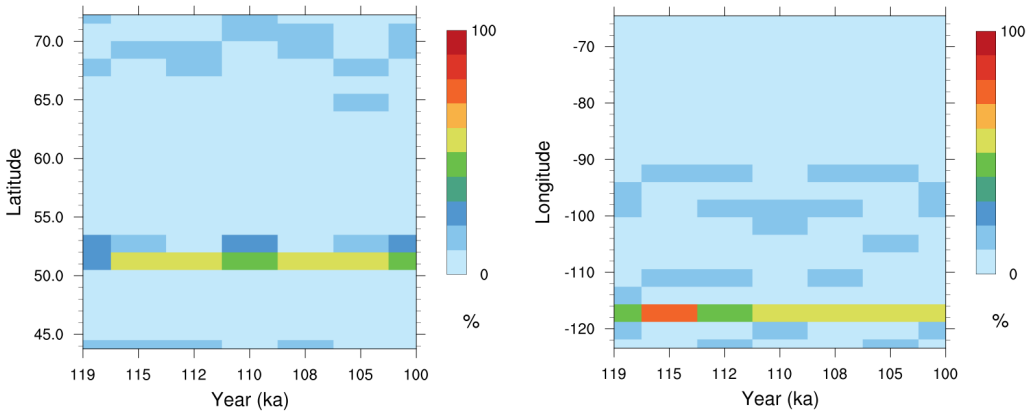

Figure B.4: The ensemble distribution of the NA ice dome **a** latitude and **b** longitude during the first 20 kyr of inception.

B.3 Ice Dome

In the NA continent, the location of the ice dome is consistent in more than 50% of the simulations through the first 20 kyr of the last glacial period (figure B.4). For most of the period, the ice dome latitude is between 50 and 55 °N, and the longitude around 118 °W. I see the two major variations in the ice dome latitude during the initial phase (prior to 118 ka) and the maximum (∼110 ka). However, no major change in the ice dome latitude is detected even during these periods (less than 2 °). The NA ice dome longitude behaves slightly different, as the ensemble longitude is more robust right after the ice initiation, and then oscillates prior to the first maximum (110 ka). This is due to the presence of thick ice sheets in the western NA, which shortly after the inception becomes the dominant ice sheet in the NA continent.

The location of the ice dome in the EA region is more variable through time

compared to NA. The EA ice dome, unlike NA, does not show a preferred latitude during the growth phase, reaches the highest variation around the peak time (110 ka). The discrepancy between runs during the shrink phase declines, and most of the runs tend to put the ice dome in the lower latitudes. Unlike the EA ice dome latitude, the EA ice dome longitude has a smaller range of variation during most of the inception phase (10 °between 120 and 100 ka). Similar to the latitude, the largest variation occurs during the peak time.

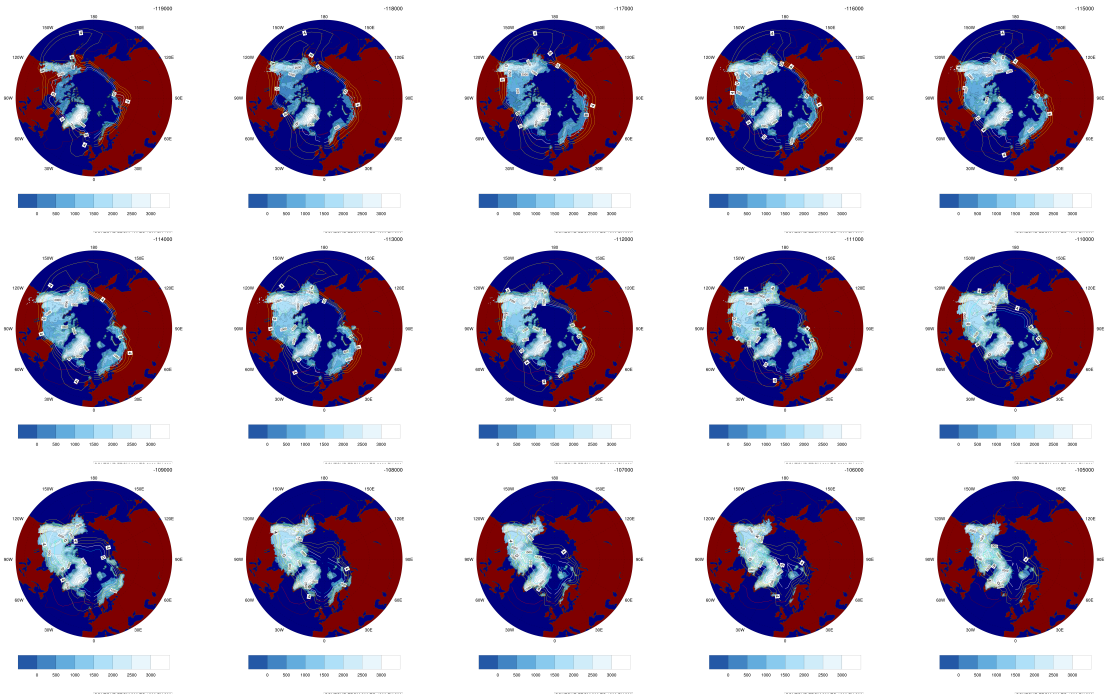

Figure B.5: The evolution of ice sheets elevation (shaded areas in light blue-white gradient), 2 meter temperature (blue, white, and yellow contour lines), and sea ice maximum and minimum extent (dark and light red) for every 1 kyr from 119 ka to 105 ka for one of the best simulations of the ensemble.

B.4 Snapshots of ice and climate during the LGI

Appendix C

Supplementary material for: The role of the Northern Hemispheric Ice Sheets in Last Glacial Inception

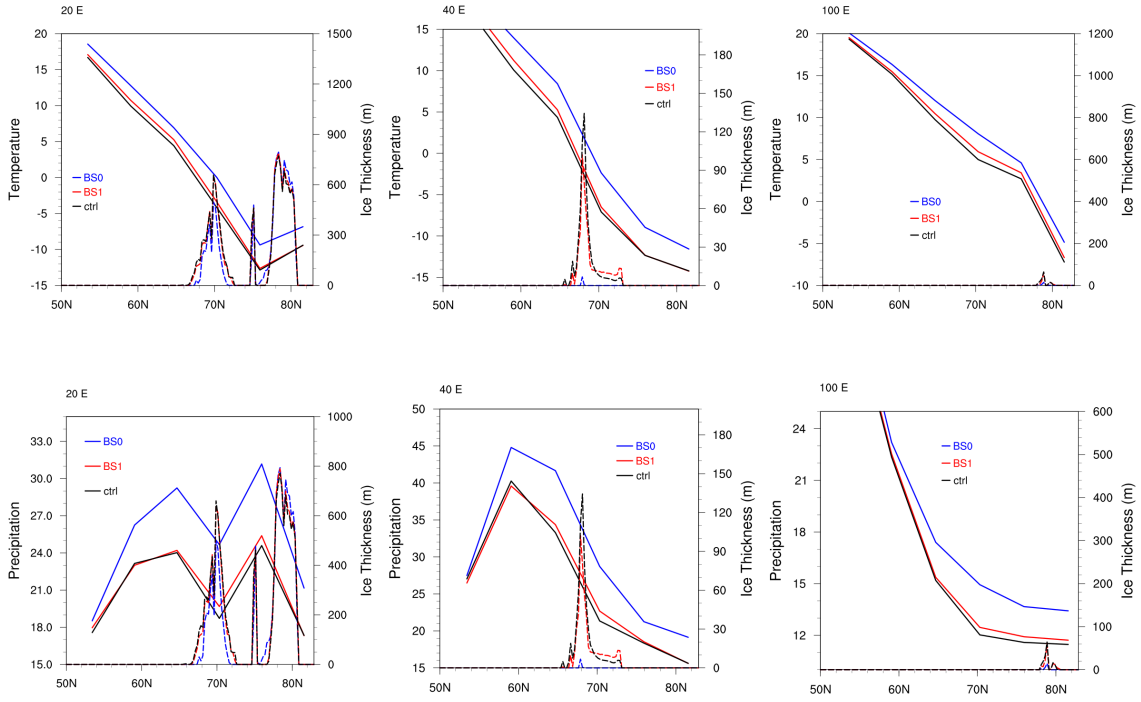

Figure C.1: Ice thickness, temperature (first row), and precipitation (second row) profiles along the 20°E (left column), 40°E (middle column), and 100°E (right column) at 119 ka for fixed BS experiments (BS0 blue, BS1 red, and ctrl black). Dashed lines show the ice thickness, and solid lines temperature or precipitation.

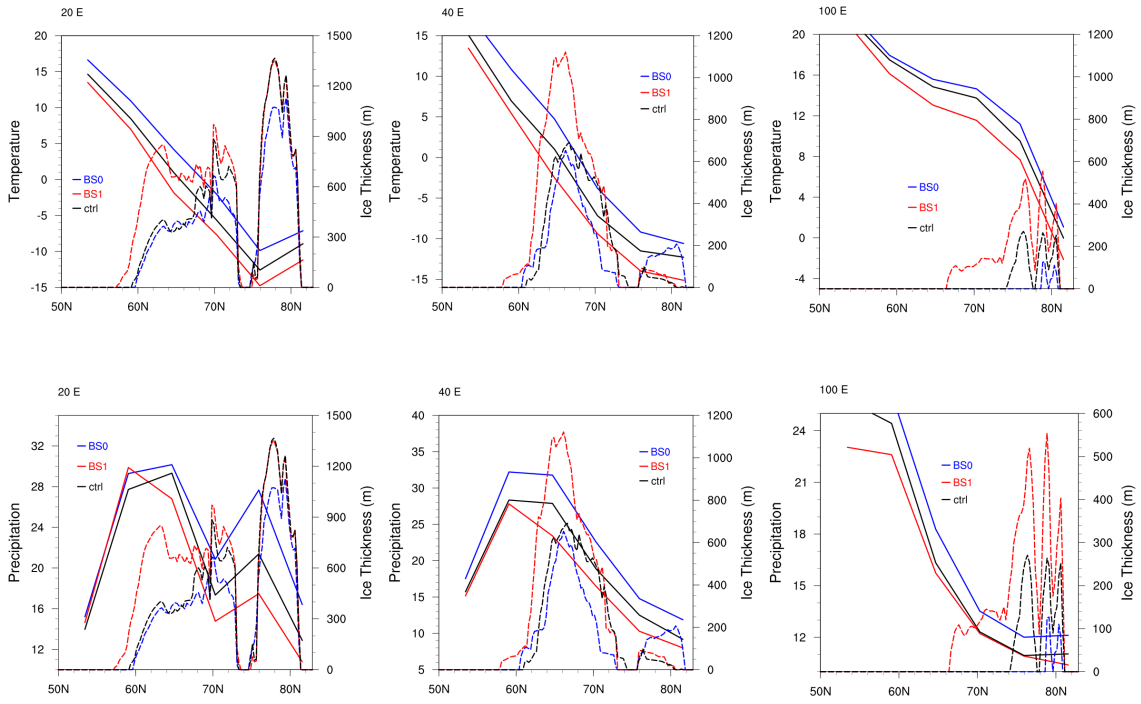

Figure C.2: Ice thickness, temperature (first row), and precipitation (second row) profiles along the 20°E (left column), 40°E (middle column), and 100°E (right column) at 112 ka for fixed BS experiments (BS0 blue, BS1 red, and ctrl black). Dashed lines show the ice thickness, and solid lines temperature or precipitation.

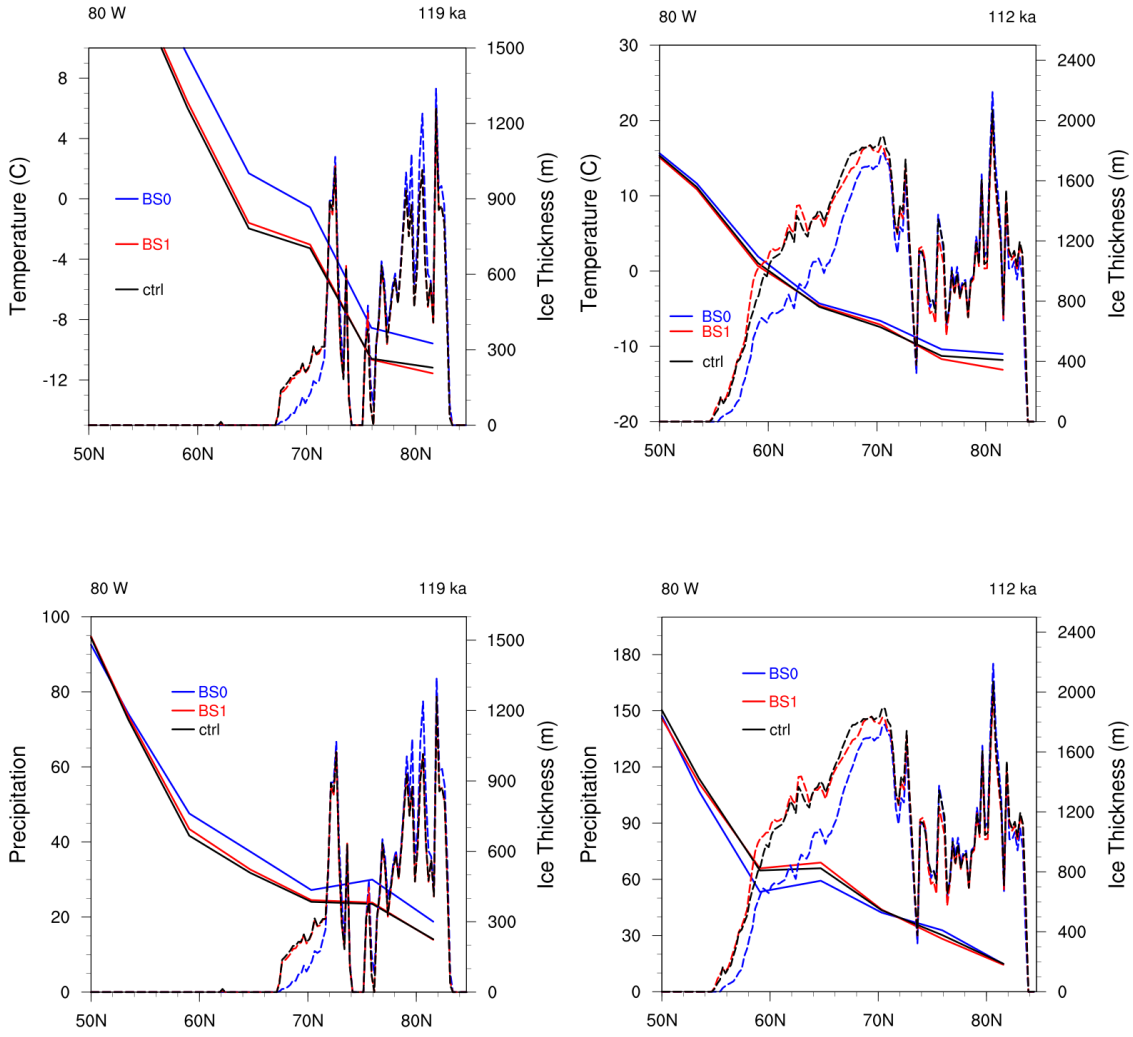

Figure C.3: Ice thickness, temperature (first row), and precipitation (second row) profiles along the 80°W in NA at 119 ka (left column), and 112 ka (right column) for fixed BS experiments (BS0 blue, BS1 red, and ctrl black). Dashed lines show the ice thickness, and solid lines temperature or precipitation.

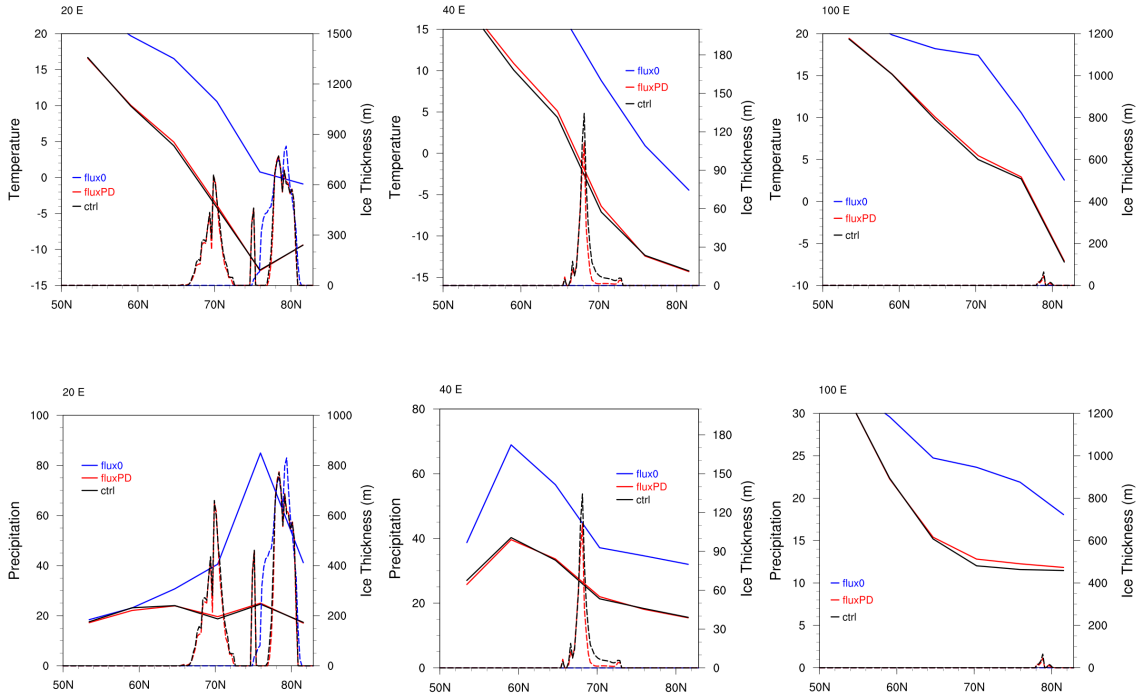

Figure C.4: Ice thickness, temperature (first row), and precipitation (second row) profiles along the 20°E (left column), 40°E (middle column), and 100°E (right column) at 119 ka for fixed runoff experiments (flux0 blue, fluxPD red, and ctrl black). Dashed lines show the ice thickness, and solid lines temperature or precipitation.

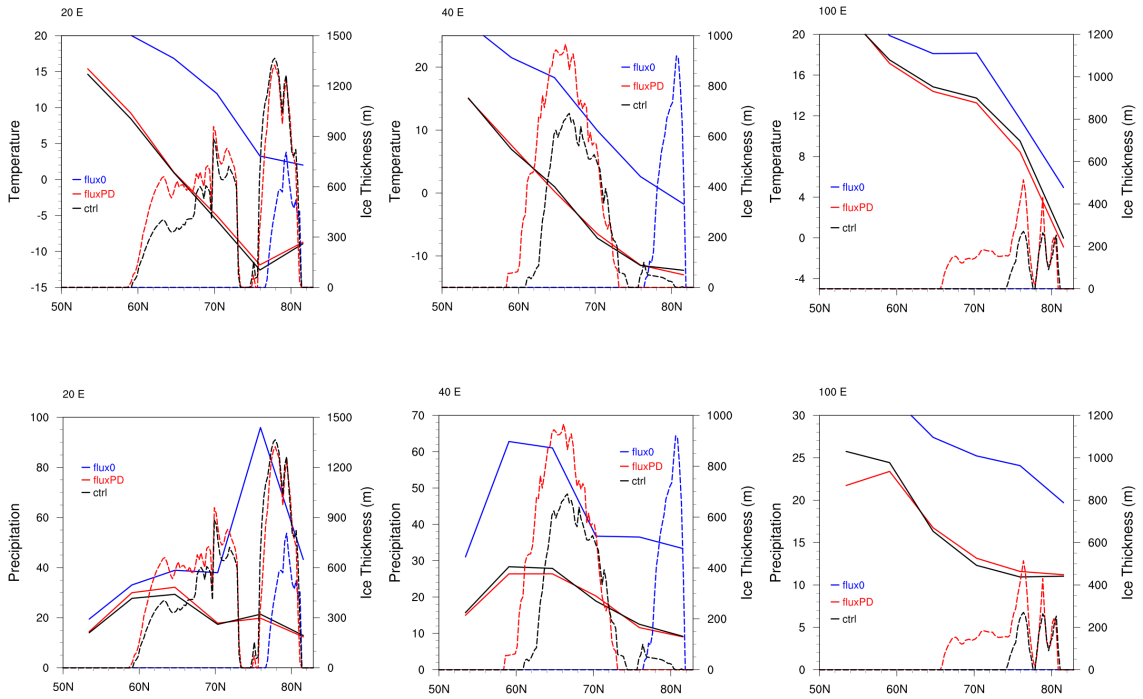

Figure C.5: Ice thickness, temperature (first row), and precipitation (second row) profiles along the 20°E (left column), 40°E (middle column), and 100°E (right column) at 112 ka for fixed runoff experiments (flux0 blue, fluxPD red, and ctrl black). Dashed lines show the ice thickness, and solid lines temperature or precipitation.

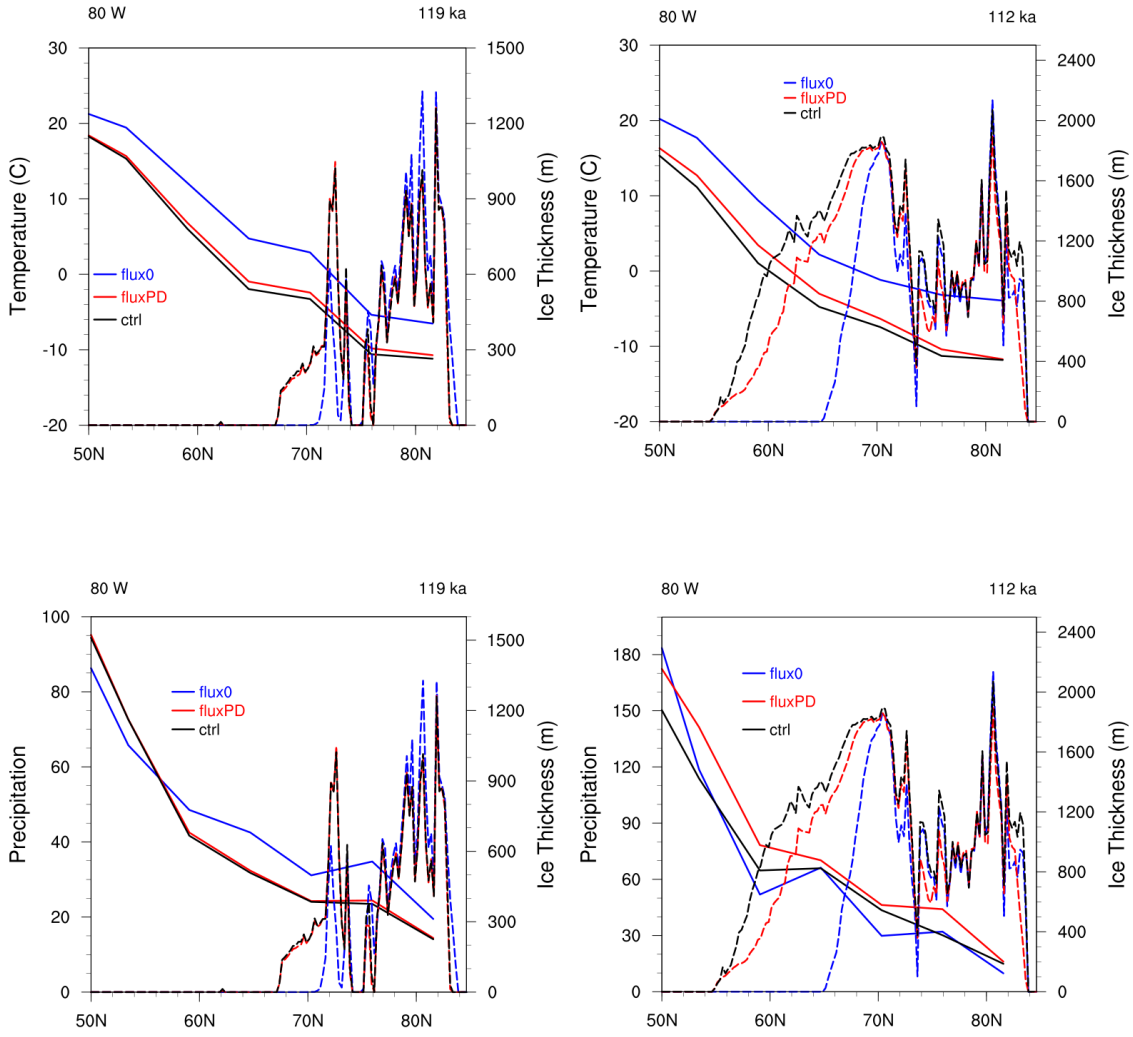

Figure C.6: Ice thickness, temperature (first row), and precipitation (second row) profiles along the 80°W in NA at 119 ka (left column), and 112 ka (right column) for fixed runoff experiments (flux0 blue, fluxPD red, and ctrl black). Dashed lines show the ice thickness, and solid lines temperature or precipitation.

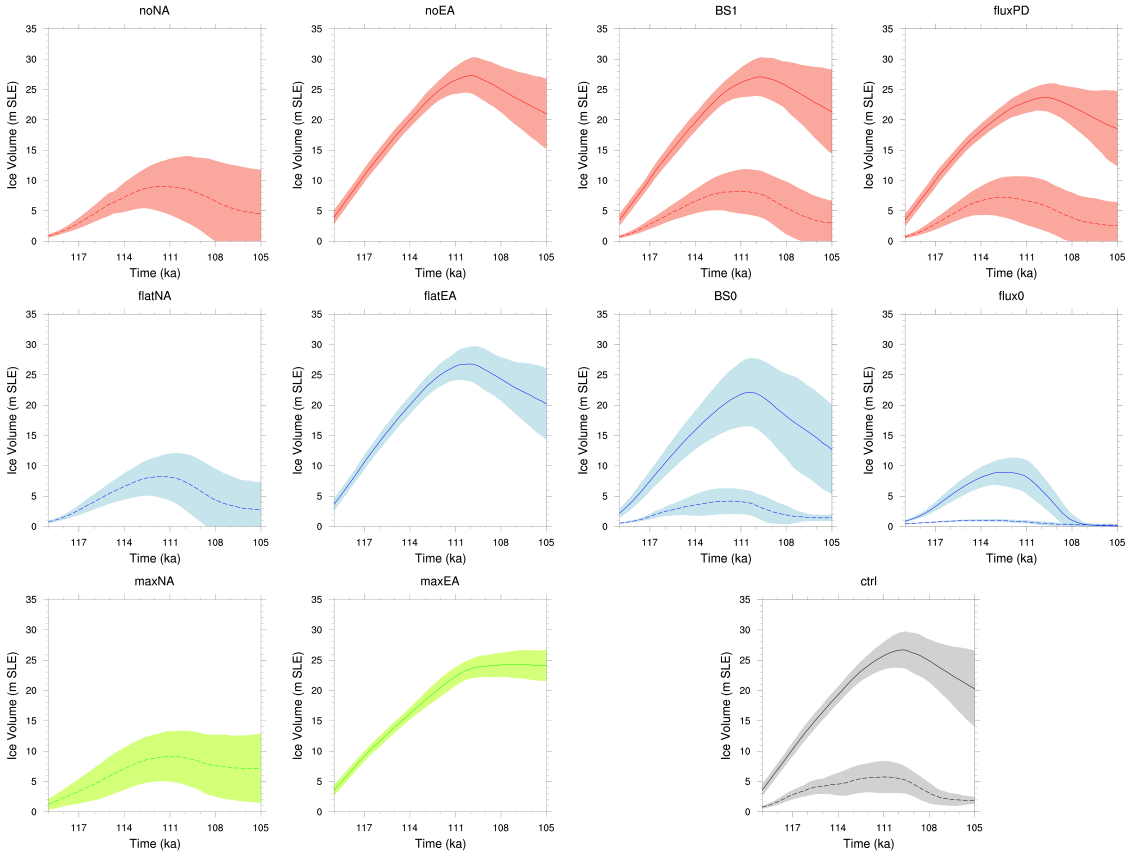

Figure C.7: Ensemble mean (lines) and one standard deviation (colored areas) of NA (solid line) and EA (dashed line) sea level equivalent ice volumes for each experiment. The colors are chosen to match the colors used in the main paper. The first and second columns on the right only include the EA and NA ice volumes, respectively.

Table C.1: List of ensemble members and their parameter values.

run ID	spinup interval (yr)	upscl	snow albedo	ice albedo	melt ice albedo	precipitation threshold	cloud parameterization	dynamic lapse-rate	start year (ka)
run0256	4800	simple	0.854	0.442	0.435	0.813	1	1	125.3
run0351	4200	simple	0.863	0.574	0.584	0.808	0	1	124.1
run0359	3800	envelope	0.856	0.521	0.528	0.875	0	1	124.7
run0525	3100	simple	0.795	0.600	0.507	0.801	1	1	125.3
run0661	3000	envelope	0.807	0.533	0.577	0.807	0	1	125.1
run0664	3900	envelope	0.901	0.671	0.674	0.865	0	1	124.6
run0693	4500	simple	0.803	0.493	0.538	0.790	0	1	125.7
run1058	3200	envelope	0.897	0.676	0.605	0.832	0	1	125.4
run1352	3400	envelope	0.718	0.633	0.563	0.761	0	1	124.6
run1666	3000	envelope	0.814	0.419	0.442	0.847	1	1	124.7
run1928	4000	Silhouette	0.862	0.623	0.479	0.905	0	0	125.9